Report No. FAA/PS-88/10



Project Report
ATC-159

# Low-Altitude Wind Shear Detection with Airport Surveillance Radars: Evaluation of 1987 Field Measurements

M.E. Weber
T.A. Noyes



31 August 1988

**Lincoln Laboratory**

MASSACHUSETTS INSTITUTE OF TECHNOLOGY

*LEXINGTON, MASSACHUSETTS*

The work reported in this document was performed at Lincoln Laboratory, a center for research operated by Massachusetts Institute of Technology under Air Force Contract F19628-85-C-0002.



Document is available to the public through the National Technical Information Service, Springfield, VA 22161.

TECHNICAL REPORT STANDARD TITLE PAGE

| 1. Report No. | 2. Government Accession No. | 3. Recipient's Catalog No. |
|---|---|---|
| DOT/FAA/PS-88-10 | | |

| 4. Title and Subtitle | 5. Report Date |
|---|---|
| Low-Altitude Wind Shear Detection with Airport Surveillance Radars: Evaluation of 1987 Field Measurements | 31 August 1988 |
| | 6. Performing Organization Code |
| 7. Author(s) | 8. Performing Organization Report No. |
| Mark E. Weber and Terri A. Noyes | ATC-159 |
| 9. Performing Organization Name and Address | 10. Work Unit No. (TRAIS) |
| Lincoln Laboratory, MIT<br>P.O. Box 73<br>Lexington, MA 02173-0073 | 11. Contract or Grant No.<br>DTFA-01-80-Y-10546 |
| | 13. Type of Report and Period Covered |
| 12. Sponsoring Agency Name and Address | Project Report |
| Department of Transportation<br>Federal Aviation Administration<br>Program Engineering Service<br>Washington, DC 20591 | 14. Sponsoring Agency Code |

15. Supplementary Notes

The work reported in this document was performed at Lincoln Laboratory, a center for research operated by Massachusetts Institute of Technology, under Air Force Contract F19628-85-C-0002.

16. Abstract

A field measurement program is being conducted to investigate the capabilities of airport surveillance radars (ASR) to detect low altitude wind shear (LAWS). This capability would require minor RF signal path modifications in existing ASRs and the addition of a signal processing channel to measure the radial velocity of precipitation wind tracers and automatically detect regions of hazardous velocity shear. A modified ASR-8 has been deployed in Huntsville, Alabama and is operated during periods of nearby thunderstorm activity. Data from approximately 30 " wet" (i.e., high radar reflectivity) microbursts during 1987 have been evaluated through comparison with simultaneous measurements from a collocated pencil beam weather radar. In this report, we describe the 1987 field experiment and utilize the resulting data to illustrate problems and potential processing approaches for LAWS detection with airport surveillance radars. Techniques are described for estimation of low altitude wind fields in the presence of interference such as ground clutter or weather aloft and for automatic detection of microburst wind shear from the resulting radial velocity fields. Evaluation of these techniques using case studies and statistical scoring of the automatic detection algorithm indicates that a suitably modified ASR could detect wet microbursts within 16 km of the radar with a detection probability in excess of 0.90 and a corresponding false alarm probability of less than 0.10. These favorable results indicate the need for careful consideration of implementation issues and the potential operational role of wind measurements from an ASR.

| 17. Key Words | | 18. Distribution Statement |
|---|---|---|
| low altitude wind shear<br>airport surveillance radar<br>microburst<br>radial velocity estimation | hazard detection algorithm<br>detection probability<br>false alarm probability | Document is available to the public through the National Technical Information Service, Springfield, VA 22161. |

| 19. Security Classif. (of this report) | 20. Security Classif. (of this page) | 21. No. of Pages | 22. Price |
|---|---|---|---|
| Unclassified | Unclassified | 120 | |

FORM DOT F 1700.7 (8-69)

**Low-Altitude Wind Shear Detection with Airport Surveillance Radars: Evaluation of 1987 Field Measurements**

*ABSTRACT*

A field measurement program is being conducted to investigate the capabilities of airport surveillance radars (ASR) to detect low altitude wind shear (LAWS). This capability would require minor RF signal path modifications in existing ASRs and the addition of a signal processing channel to measure the radial velocity of precipitation wind tracers and automatically detect regions of hazardous velocity shear. A modified ASR-8 has been deployed in Huntsville, Alabama and is operated during periods of nearby thunderstorm activity. Data from approximately 30 "wet" (i.e. high radar reflectivity) microbursts during 1987 have been evaluated through comparison with simultaneous measurements from a colocated pencil beam weather radar. In this report, we describe the 1987 field experiment and utilize the resulting data to illustrate problems and potential processing approaches for LAWS detection with airport surveillance radars. Techniques are described for estimation of low altitude wind fields in the presence of interference such as ground clutter or weather aloft and for automatic detection of microburst wind shear from the resulting radial velocity fields. Evaluation of these techniques using case studies and statistical scoring of the automatic detection algorithm indicates that a suitably modified ASR could detect wet microbursts within 16 km of the radar with a detection probability in excess of 0.90 and a corresponding false alarm probability of less than 0.10. These favorable results indicate the need for careful consideration of implementation issues and the potential operational role of wind measurements from an ASR.

## TABLE OF CONTENTS

## LIST OF ILLUSTRATIONS

## LIST OF TABLES

# Low-Altitude Wind Shear Detection with Airport Surveillance Radars: Evaluation of 1987 Field Measurements

## I. INTRODUCTION

This report addresses the potential applications and major technical problems associated with the detection of low-altitude wind shear (LAWS) using airport surveillance radars (ASR). This capability would require a signal processing upgrade to ASRs to support:

(i) measurement of microburst and gust front winds;

(ii) automatic recognition of regions of hazardous wind shear.

Analysis of this problem has been underway at Lincoln Laboratory and cooperating universities since 1984 under Federal Aviation Agency (FAA) sponsorship. Initial work used data from meteorological Doppler radars and operational ASRs to analyze the expected impact on wind measurements of severe ground clutter, a broad, cosecant-squared elevation beam pattern and short, time varying coherent processing intervals [1,2]. Candidate signal processing sequences were proposed and their expected performance assessed [2,3].

Results of these analyses led in 1985 to the design of a data collection facility that would provide a realistic assessment of the capabilities of an airport surveillance radar for wind shear detection. One transmit-receive channel of an ASR-8 was obtained on loan from the U.S. Navy. Lincoln Laboratory modified the radar transmitter to provide better stability and the capability to transmit either a constant pulse repetition frequency (PRF) waveform or the block-staggered sequence used by the ASR-9. A time-series data acquisition system allows for simultaneous recording of in-phase and quadrature signals from both high and low beam signals out to a maximum instrumented range of 60 nmi. This broad band recording capability facilitates comparative evaluation of various signal processing techniques.

The testbed radar was deployed near Huntsville, Alabama and became operational in late 1986. During the summer of 1987, approximately 50 microbursts and gust fronts occurred near this test facility and were recorded on digital tape. Initial analysis has indicated that an ASR can automatically detect wet microbursts in an area extending 12 to 16 km from the radar and that reasonably accurate velocity shear estimates are feasible provided that suitable data processing techniques are employed. These encouraging results indicate the need for:

(a) further data collection and analysis to refine our understanding of the capabilities and limitations of ASRs for wind shear detection;

(b) careful consideration as to how data from this radar should be integrated with existing or planned terminal-area LAWS sensors.

The remainder of this section will briefly describe the potential operational role of ASR wind shear measurements. These applications define the technical requirements for interference suppression, velocity shear measurement accuracy and

automatic hazard detection performance that will be addressed in the remainder of this report.

## A. Background

During the last two decades, thunderstorm generated low-altitude wind shear has been identified as the primary cause of twelve major air-carrier accidents. Seven of these accidents involved fatalities, resulting in the loss of 575 lives.

Figures I-1 illustrates the two principal causes of low-altitude wind shear. A microburst (Figure I-1(a)) is an intense, thunderstorm downdraft which encounters the earth's surface producing a brief outburst of highly divergent horizontal winds [4]. Aircraft penetrating a microburst on take-off or landing experience headwind-to-tailwind velocity shear compounded by the downdraft in the microburst core. Gust fronts [5], as depicted in Figure I-1(b), are thunderstorm outflows whose leading edges propagate well away from the generating precipitation. The wind shear encountered by an aircraft penetrating a gust front is considered less hazardous than that associated with a microburst since the change is towards greater lift. However, the winds behind the front are turbulent and the long-term change of wind direction following a gust front passage is of concern for runway usage. Tracking and prediction of gust front arrivals at an airport would yield significant benefit for airport operations.

In response to these wind-shear hazards, the FAA has initiated a two-part enhancement to its terminal area weather information system. The on-airport network of surface wind-speed and direction sensors -- Low Level Wind Shear Alert System (LLWAS) -- is being expanded from six stations to eleven and its wind shear detection algorithm reworked. In addition, a dedicated, microwave Terminal Doppler Weather Radar (TDWR) will be deployed at 50 to 100 airports to measure the radar reflectivity and radial velocity signatures associated with low-altitude wind shear. The TDWR systems will be preceded by FAA-operated "terminal" S-band NEXRAD radars (approximately 20) with a transition to all C-band TDWR's for airport weather surveillance planned for the mid 1990's.

The existing LLWAS systems suffer from two major performance deficiencies:

(i) false reports are often generated by turbulent gusts that do not reflect organized, convectively driven wind shear. These frequent false alarms have reduced pilot confidence in LLWAS reports to the point that alarms are often ignored;

(ii) small-scale hazardous wind shear events such as microbursts have been detected late or missed altogether because the wind vector gradients occurred between stations or outside the network's coverage.

Enhanced LLWAS will provide improvement in both of these areas [6]. However, coverage will continue to be confined to corridors extending at most 5 km from the runway ends and -- as a stand-alone system -- supporting information on storm location and structure will be unavailable. In particular, enhanced LLWAS will not provide forecasts of the movement of wind shear into the approach/departure corridors and cannot distinguish between a microburst and a gust front at the edge of the sensor network.

The TDWR will provide high quality, rapid update measurements of storm structure and radial winds. The scanning strategy calls for an update of the

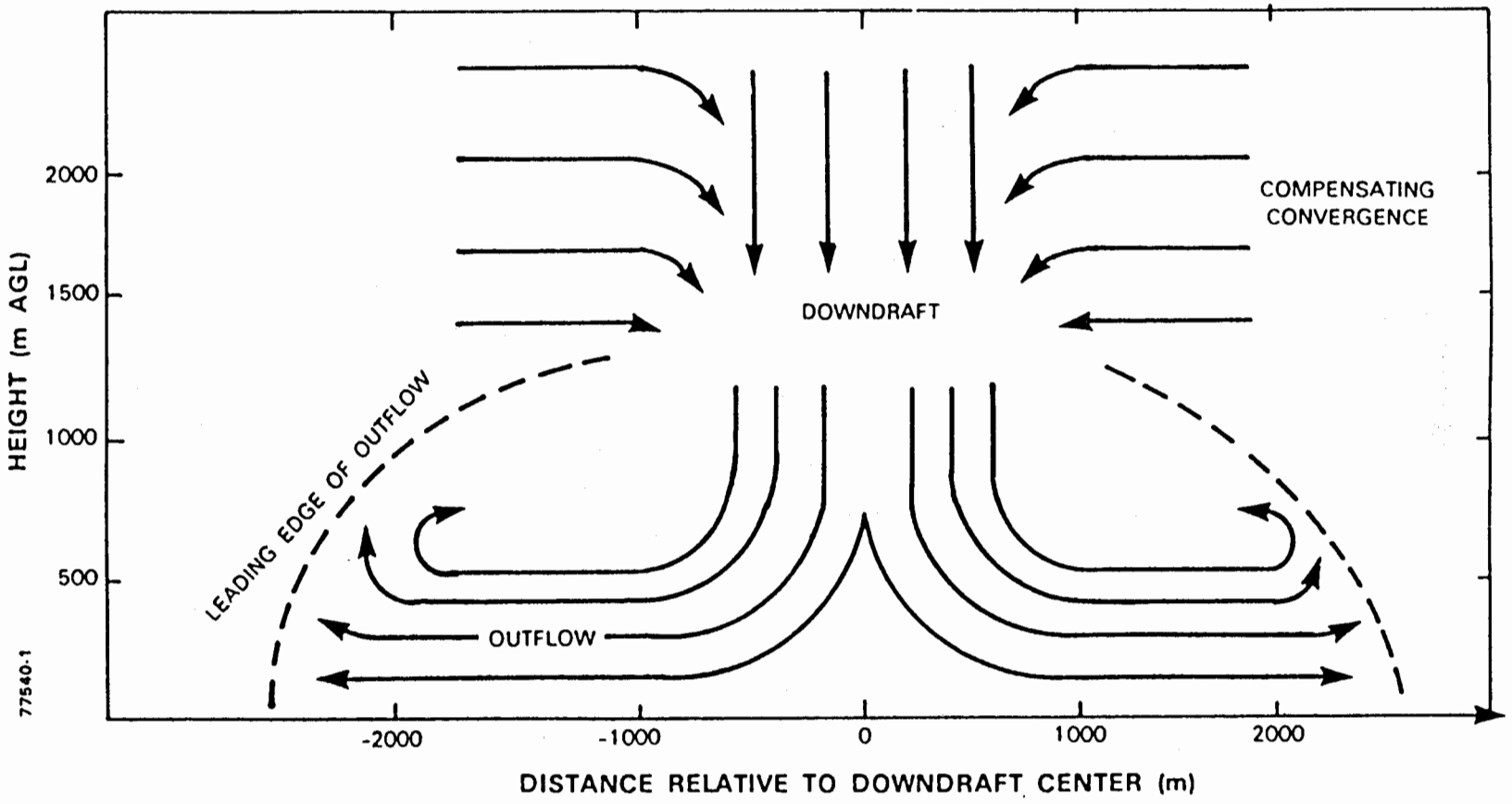


Figure I-1(a) Vertical cross section of microburst wind field.

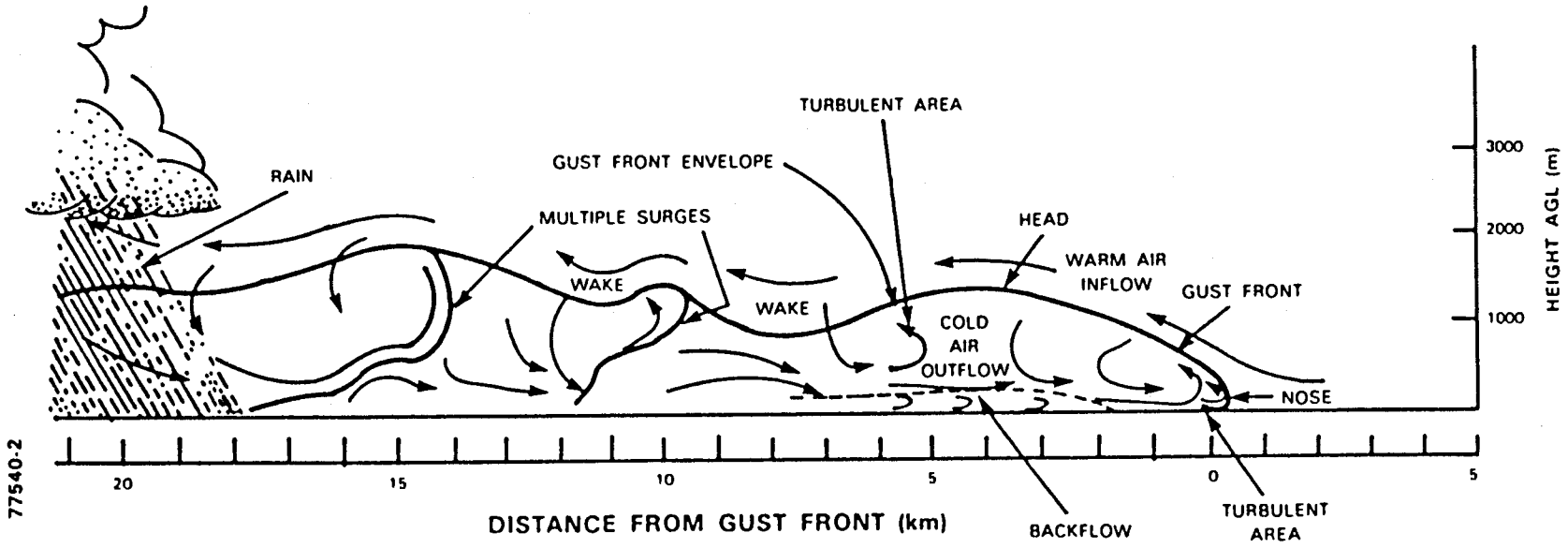


Figure I-1(b) Vertical cross section of gust front. (From Goff [5].)

surface radial velocity field once each minute with the remaining time spent executing volumetric scanning to identify storm features aloft. The FAA system requirements statement calls for the capability to automatically detect microburst wind shear with a 0.90 or better probability of detection and to measure the intensity of the shear to within 0.20 relative error. Forecasts of microburst occurrence based on recognition of precursory features aloft are viewed as highly desirable but are not a system requirement at this time.

One unresolved issue for the TDWR is achievement of the required velocity shear estimate accuracy for microbursts whose outflow winds are not radially symmetric. Multiple Doppler radar measurements of microburst winds have indicated that the velocity shear encountered by an aircraft penetrating a microburst may vary by a factor of three or more depending on the direction of penetration [7]. While it is not clear how often such large asymmetries occur or whether they persist during the entire outflow period, this result indicates that a TDWR should ideally be sited so that radials from the radar are aligned with the major runways and their approach/departure corridors. Even if such a location can be found at an airport the site may not be suitable owing, for example, to blockage by nearby buildings. In addition such a location is likely to conflict with the desired off-airport siting that will enable a TDWR to efficiently scan aloft for microburst precursors. The General Accounting Office has stated [8] that the problems associated with asymmetric microbursts may prevent TDWR from fully meeting the objectives for which it is being procured.

### B. Potential Role of Airport Surveillance Radar Wind Measurements

The FAA is deploying 103 new airport surveillance radars (ASR-9) at U.S. air terminals while relocating the existing ASR-7s and ASR-8s to secondary terminals. Thus, by 1992 almost every U.S. airport that supports commercial operations will be equipped with one of these modern airport surveillance radars. As discussed in reference [1], the critical areas for LAWS detection lie within 10 km of the airport center for most runway layouts. Given the on- or near-airport siting of ASRs, the coverage requirements for reliable wind shear measurement will thus be an approximately 10 km radius circle centered on the radar.

A stand-alone wind shear detection capability for ASRs would allow a number of airports that will not have TDWR or LLWAS to be provided with LAWS warnings, *albeit* possibly with lower confidence than would be provided by the dedicated wind shear sensors. The relatively small incremental cost associated with equipping ASRs with wind-shear processors probably justifies this stand-alone role, even if the additional airports covered have low traffic volume or are in locales where wind shear is infrequent.

As stated above, a shortcoming of even the enhanced LLWAS system will be the limited aerial coverage of the sensor network. At airports equipped with LLWAS but lacking a TDWR, data from an airport surveillance radar could be used to reinforce LLWAS wind shear reports and to detect wind shear in operationally significant areas not covered by the surface station network.

At airports slated to receive a TDWR, additional radar wind measurements from an ASR could help to reduce headwind-tailwind shear estimate inaccuracies resulting from outflow asymmetry. The siting of the ASR will often provide a

better viewing angle for headwind-tailwind shear measurements along some runways. Alternately, data from the two radars may be combined to compute the total horizontal component of the wind vector over areas where radials from the two radars intersect at approximately right angles.

To quantify the accuracy of such two-radar wind shear estimates relative to estimates from a TDWR alone, we examined the planned TDWR and current ASR locations at Denver Stapleton and Dallas-Ft. Worth International Airports relative to the principal runways. As described in Appendix A, we assumed a worst-case scenario of a severely asymmetric microburst oriented with peak shear along the runway. Estimated headwind-tailwind shear was calculated given either:

(i) single-Doppler measurements from the TDWR;

(ii) dual-Doppler measurements from the TDWR and ASR, assuming 10 percent root mean squared (RMS) relative error in the radial velocity estimates from the individual radars.

As illustrated in Appendix A, the calculation showed that the joint use of ASR wind data in conjunction with a TDWR could yield a significantly larger area near the runways with accurate (RMS relative errors $< 0.20$) headwind-tailwind shear estimates.

## C. Scope of Report

The remainder of this report describes the ASR wind measurement experimental facilities in Huntsville and presents results from the 1987 measurement program. Section II describes the ASR emulation system and supporting sensors used to confirm the nature of the weather phenomena. A summary of wind shear activity near the testbed facility during 1987 is given in section III. Section IV reviews the major issues involved in low-altitude radial velocity measurement with an ASR, using testbed data for illustration of the problems and potential processing solutions. An automatic microburst detection algorithm that used data from the ASR testbed as input is described in Section V. We then evaluate the performance of the signal processing-hazard detection sequence through case studies and presentation of overall detection and false alarm probabilities for automatic microburst declarations. Conclusions and an outline of necessary future investigations are given in Section VII.

## II. HUNTSVILLE TESTBED FACILITIES

Lincoln Laboratory's airport surveillance radar test facilities in Huntsville, Alabama were constructed to support the evaluation of the ASR-9's dedicated six-level weather reflectivity processor [9] as well as our investigations of the radar's capabilities for low-altitude wind shear detection. An ASR-9 emulation radar, a colocated Doppler weather radar and a network of 10 surface weather stations comprise the sensor suite. Figure II-1 shows a map of the testbed facility. In this section, we describe the sensors at the level of detail necessary to evaluate our results on ASR wind shear detection.

### A. ASR-9 Emulation Radar

The FL-3 (FAA/Lincoln-Laboratory) radar is a modified ASR-8 with Lincoln Laboratory built receivers, A/D converters and digital recording apparatus. Table II-1 summarizes the parameters of the radar.

**Table II-1: FL-3 Radar Parameters**

| | |
|---|---|
| *Transmitter* | |
| Frequency | 2.73 GHz |
| Polarization | Vertical |
| Peak Power | 1.1 MW |
| Pulse Width | 0.65 $\mu$s |
| PRF (typical) | 980 $s^{-1}$ |
| *Receiver* | |
| Noise Figure | 6.0 dB |
| Sensitivity | -108 dBm |
| A/D Word Size | 12 bit |
| *Antenna* | |
| Elevation Beamwidth | $4.8^o$ |
| Azimuth Beamwidth | $1.4^o$ |
| Power Gain | 33.5 dB (high beam)<br>32.5 dB (low beam) |
| Rotation Rate | 12.5 RPM |

The antenna tower utilizes the maximum number of sections that can be employed for an ASR; the phase center of the antenna is 20.4 m AGL. To increase sensitivity to low-altitude winds relative to winds aloft, the elevation angle setting for the antenna has been depressed one degree below the normal ASR-8 setting. Thus the maximum gain point on the low-beam is $1.0^o$ above the horizon. Together, the high antenna placement and depressed beam elevation angle result in ground clutter that is severe relative to measurements we have made using operational airport surveillance radars [1,3].

The transmitter firing sequence is computer controlled so that variable or constant PRF waveforms may be transmitted. The instability residue of the ASR-8 transmitter was initially measured as -45 dB when operated in constant PRF mode and -33 dB when operated using the eight/ten pulse block-staggered PRF of the ASR-9. The primary contributors to transmitter instability at constant PRF were 60 Hz harmonics caused by cathode surface current generated by the filament power supply. Installation of a PRF-synchronous Klystron power supply early in

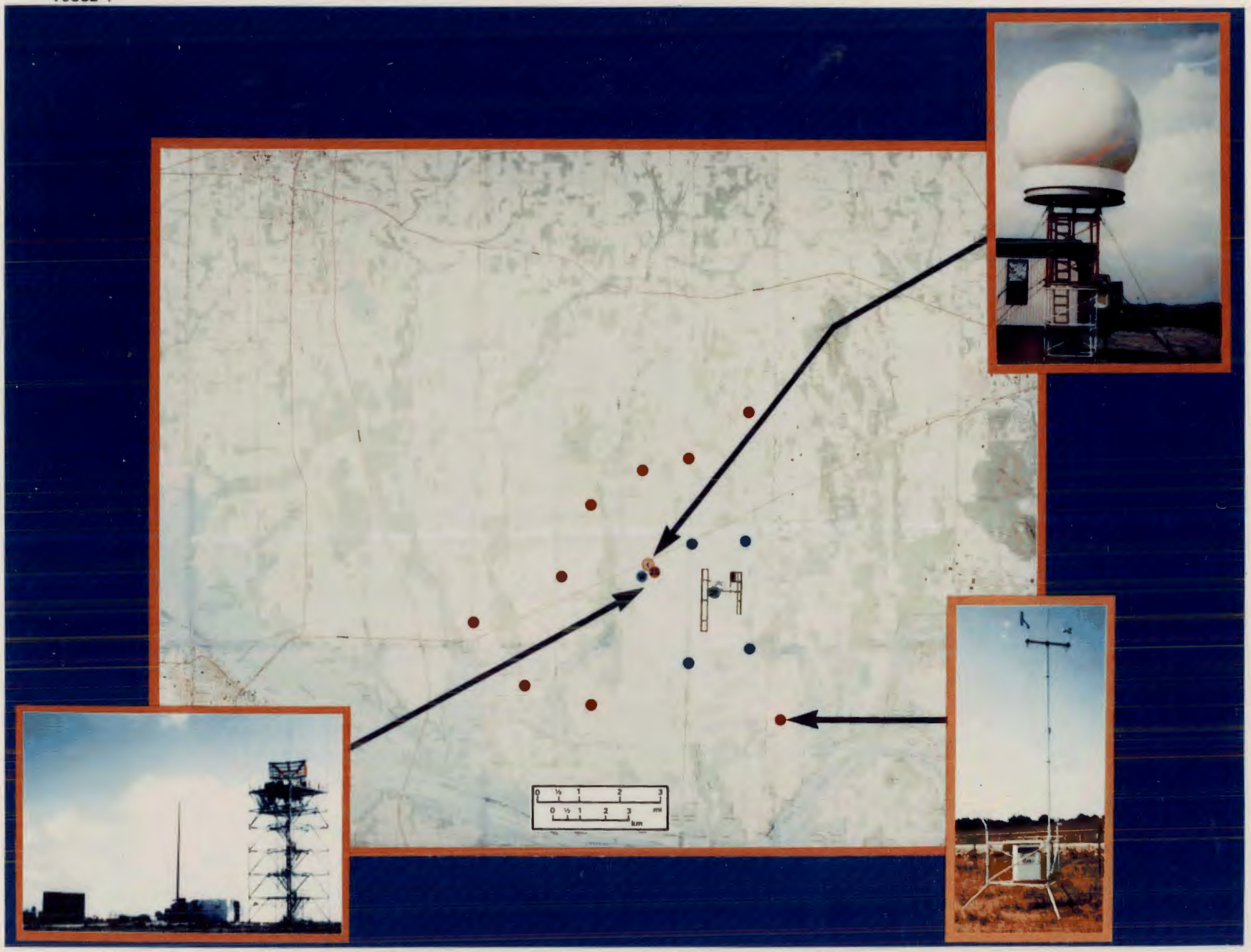


*Figure II-1. Map of Lincoln Laboratory airport surveillance radar test facilities near Huntsville, Alabama.*

July 1987 eliminated these harmonics, lowering the instability residue to -60 dB. In block staggered mode, the dominant non-zero spectral components in the transmitted waveform are at harmonics of approximately 55 Hz -- the reciprocal of the waveform period. Efforts to improve transmitter instability when using the variable-PRF ASR-9 waveform were not successful until after the 1987 summer thunderstorm season. As a result, all data analyzed in this report were collected at constant PRF. References [2] and [3] indicated that the effect of the PRF stagger on the capability of an ASR to measure winds should be minimal.

In normal aircraft surveillance operation, one of the two receiving beams of an ASR is selected as the receiver input signal although both are brought through the rotary joint. To allow for simultaneous processing of data from both high and low beams, FL-3 employs two identical receivers and analog-to-digital converters. Saturation due to ground clutter or intense weather echoes is kept to a minimum by preceding each receiver with a sensitivity-time control (STC) attenuation that varied as $(R/23km)^2$. Using this setting, the nominal system sensitivity in terms of the weather reflectivity factor is 0 dBz at ranges less than 23 km. Twelve-bit A/D converters digitize in-phase and quadrature signals from the two receiving beams every 0.8 $\mu$s (120 m in range).

In order to evaluate alternative data processing strategies, these signals and ancillary information are recorded directly on 28-track, high density digital tape. If data from both receiving beams are recorded over the full instrumented range of 115 km, a single tape will last 20 minutes. This period can be increased by selecting a smaller range interval for recording. During thunderstorm operations, we normally recorded no more than one quarter of the instrumented gates since wind shear activity at greater ranges is beyond the area of operational interest for an ASR.

Normal operating procedures were to begin recording on the high density tape as soon as thunderstorms were observed within 20 km of the radar and to continue until activity had ceased or moved beyond this range. Typically one to two high density tapes were required for an active day. Lost time during tape changes was approximately three minutes.

Both the radar and recording apparatus were highly reliable. The only major down periods occurred when system upgrades were performed or when the site backup power generator was not functioning properly.

## B. Meteorological Doppler Radar

The accuracy of wind measurements from the testbed ASR is being assessed using data from a colocated pencil-beam Doppler weather radar, operated for Lincoln Laboratory under a contract with Massachusetts Institute of Technology's Weather Radar Laboratory. The radar operates at C-band and measures weather reflectivity, radial velocity and spectrum width within an operator specified radius that can be as large as 226 km. Table II-2 lists parameters of the radar.

As stated in the table, the system processor used a 64-point coherent processing interval (CPI) for clutter rejection and radial velocity estimation. Ground clutter suppression for this coherent-on-receive radar is limited by coherent oscillator (COHO) phase jitter to about 30 dB at 4 km range, degrading to 24 dB at 17 km.

| Table II-2: MIT Weather Radar Parameters | |
|---|---|
| *Transmitter* | |
| Type | Coaxial Magnetron |
| Frequency | 5.6 GHz |
| Polarization | Vertical |
| Peak Power | 160 KW |
| Pulse Width | 1.0 $\mu$s |
| PRF (typical) | 924 $s^{-1}$ |
| *Receiver* | |
| Type | Log/Linear Coherent-on-Receive |
| Noise Figure | 6.0 dB |
| Sensitivity | Log: -108 dBm |
| | Linear: -104 dBm |
| Dynamic Range | Log: 90 dB |
| | Linear: 55 dB |
| *Antenna* | |
| Type | 2.51 m Parabolic Reflector |
| Beamwidth | 1.4° |
| Power Gain | 44.1 dB |
| Rotation Rate | 2.4 RPM (PPI Mode) |
| *Processor* | |
| A/D Word Size | Log: 8 bit (0.3 dB LSB) |
| | Linear: 10 bit |
| CPI | 64 pulses |
| Range Sampling Interval | 250 m |
| Range Coverage | 40 km |

Ground clutter breakthrough was often evident on low-elevation angle scans, particularly when weather reflectivity was low. Barring ground clutter contamination, the RMS accuracy of weather radial velocity estimates is estimated to be 0.5 m/s. The total error in the reflectivity estimates is about 2 dB.

Reflectivity estimates are obtained through a log receiving channel with total dynamic range of 90 dB. The sensitivity was set so that the minimum detectable signal at 20 km was 0 dBz. Ten-bit A/D converters limit the dynamic range of the linear (velocity estimating) channel to 55 dB. An STC function that varied with range as $R^2$ maintained this interval between 0 and 55 dBz. The velocity of weather echoes with reflectivity higher than 55 dBz can be measured accurately in spite of receiver saturation. However, the ability to extract weaker weather echoes from ground clutter is reduced when the ground clutter saturates the receiver.

The radar scanning rate was limited by:

(i) the signal processor's time requirement to filter ground clutter and estimate radial velocity for all range gates in a CPI;

(ii) wasted antenna motions built in to the radar control program.

Development of an operational scanning procedure was an iterative process requiring extensive modification of the radar control program. Through most of the summer we operated on a 3-minute update cycle where each scan sequence consisted of 360° PPI scans at 0.7° and 1.5° elevation angles, followed by RHI scans through identified wind shear events. The PPI scans provided aerial coverage and allowed for clear identification of wind shear radial velocity signatures. The RHI scans were used to measure the vertical structure of reflectivity and winds in

microburst producing storms.

In general the measurement capabilities of this "truth" radar were adequate to evaluate the accuracy of wind measurements using FL-3. Because microbursts in the Huntsville environment occur in association with heavy rain, the radar's limited sensitivity and ground clutter rejection capability were not major problems in identifying microbursts. Although the wind fields measured in gust fronts with reflectivity factors less than 5 dBz and in regions outside rain cells were often "spotty", the overall structure of the winds could be discerned by experienced observers familiar with the ground clutter distribution at this site.

The three-minute scan update period was clearly undesirable since this is long compared to both the scan rate of the ASR and to the time scale for significant changes in the intensity of microburst winds. On average there were approximately five low-elevation angle PPI scans during the course of a microburst.

### C. Surface Weather Stations

As an additional means of monitoring thunderstorm activity near the testbed radars, we deployed a network of ten surface weather stations at the locations shown in Figure II-1. These stations measure wind speed and direction at the surface. In some areas, ground clutter or blockage due to terrain relief may prevent the pencil beam weather radar from accurately measuring near-surface radial velocities. In addition, the anemometers measure both components of the horizontal wind field at the surface.

The sensor platform and anemometers are on loan to the FAA from the Bureau of Land Management. Reference [10] describes these stations in the context of a larger MESONET operated as part of Lincoln Laboratory's TDWR development program. In our system, thirty-second averages of wind speed and direction and peak wind speeds during the same 30-second interval are recorded on digital logging devices. The data loggers' first-in-first-out memory can store information from the most recent three-day period. Following periods of thunderstorm activity, data are retrieved from the devices and transferred to computer-compatible tape.

Logistical problems delayed the deployment of the wind-speed and direction sensors until September 1987. Since most of the observed low altitude wind shear activity occurred prior to this date, we have not attempted to include the surface sensor wind speed and direction observations in the microburst truth data set for this report. Based on the results of Clark [11], we believe that virtually all microbursts within 20 km were measured by the MIT weather radar.

### D. Data Transfer and Processing

Time-series data from the ASR-9 emulation radar were transferred from high-density tape to computer-compatible 6250 BPI tape for off-line processing. An engineering workstation was used to estimate the reflectivity factor and radial velocity in each range-azimuth resolution cell according to the algorithms described in Section IV. This processing was extremely slow, requiring tens of

minutes to complete a single scan (4.8 seconds) of data. As a result, we typically transferred only selected range-azimuth wedges containing the thunderstorm cells of interest, and processed only one scan every 30-60 seconds. These fields were then processed by the automatic wind shear detection algorithm described in Section V and resampled into Cartesian image files for display.

## III. SUMMARY OF WIND SHEAR ACTIVITY

### A. Short Range Microbursts

The summer of 1987 produced significantly less thunderstorm activity than normal in the Huntsville area. By mid-September, recorded rainfall accumulations were 7 inches below the climatological mean. As a result, the number of wind shear events observed within the operationally significant range interval extending 10 km from our radars was less than we had anticipated based on measurements during 1986 with Lincoln Laboratory's TDWR testbed [12]. In addition, data from several microbursts that occurred at short range were not recorded on the ASR testbed because of power failures or pre-scheduled system maintenance.

Table III-1 summarizes microburst activity on days that have been analyzed for this report. These days were chosen because microbursts occurred close to the radars and both systems were operating satisfactorily. For each day, the number of microbursts within 10 km range and within the 10-20 km range annulus are tabulated along with the maximum velocity shears measured by the C-band radar. The count of separate microburst events on some days was subjective because many of the thunderstorms we observed produced long-duration outflows with significant structural and intensity modulation over their lifetimes.

Table III-1: Summary of Analyzed 1987 Microburst Days

| | 0-10 km | | 10-20 km | |
|---|---|---|---|---|
| Date | Number of Microbursts | $\Delta$ V (m/s) | Number of Microbursts | $\Delta$ V (m/s) |
| 21 May | 2 | 18,28 | 2 | 10,10 |
| 14 June | 2 | 32,19 | 2 | 17,27 |
| 21 June | 2 | 20,27 | 2 | 22,20 |
| 1 August | 2 | 19,18 | 2 | 17,19 |
| 3 August | 0 | - | 4 | 14,23,19,13 |
| 10 August | 2 | 27,20 | 1 | 24 |
| 10 September | 3 | 31,14,27 | 0 | - |
| 11 September | 3 | 27,23,10 | 1 | 11 |

For each of these days, all recorded data from the MIT weather radar have been examined to generate a data base of microburst locations, spatial extent, radial velocity differential and outflow height. The first three parameters were obtained from the low elevation angle PPI data whereas outflow heights were measured by examining the RHI scans. The height resolution of the MIT radar's beam is 120 m at 5 km range.

### B. Reflectivity Factor in Microburst Producing Storms

Figure III-1 plots the distribution of reflectivity factors measured in the precipitation cores that generated the microbursts. These values reflect therefore the highest surface radar reflectivity factors in the microbursts. In more than 85% of the scans, the outflow winds were accompanied by precipitation reflectivity factors equal to or greater than 50 dBz. There were no scans where a microburst

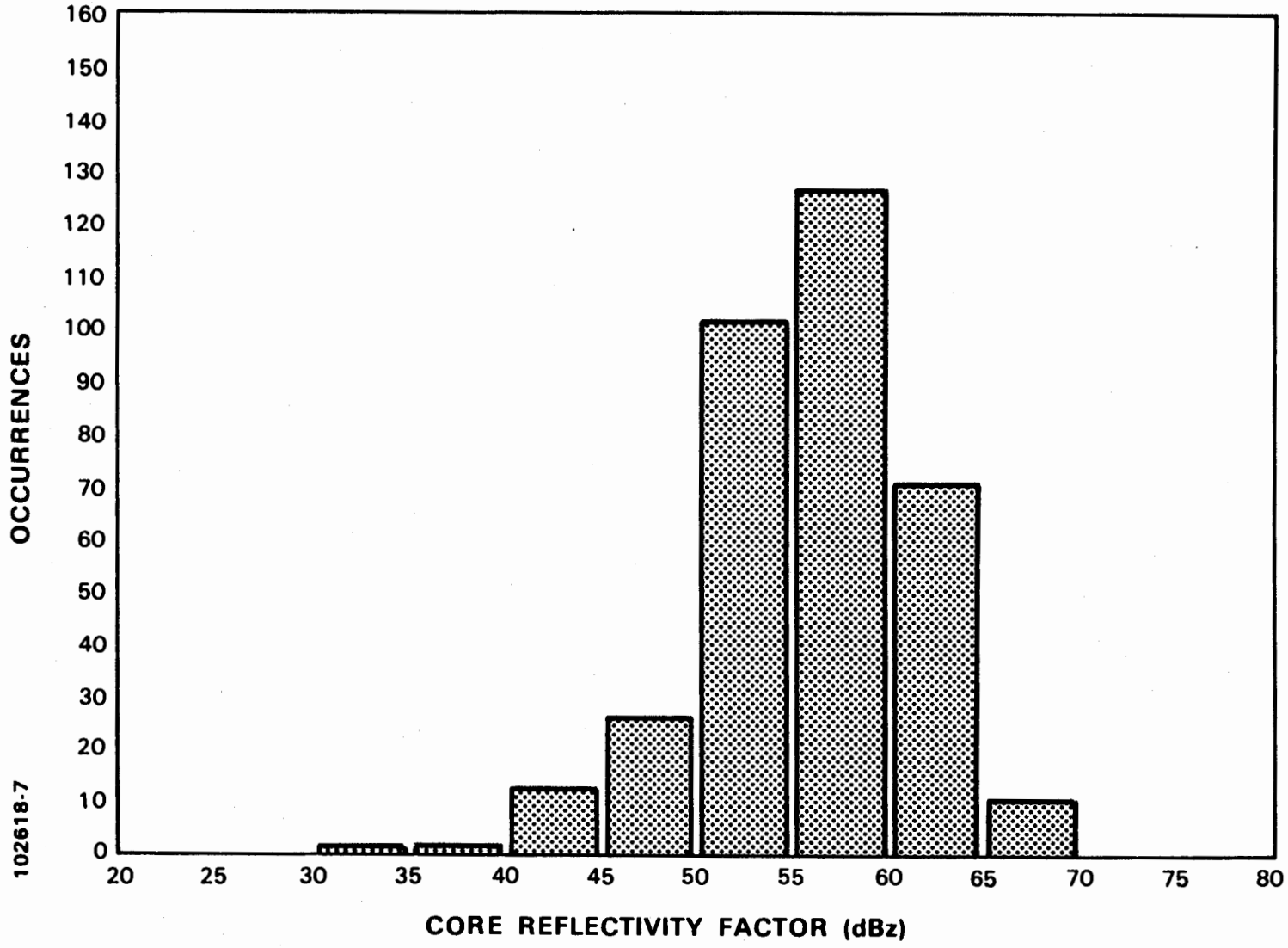


Figure III-1 Distribution of the maximum, near-surface radar reflectivity factor measured in microbursts near the ASR testbed facilities in 1987.

occurred in a cell with a maximum surface reflectivity factor less than 30 dBz. These results reinforce previous measurements [13] indicating that "wet" microbursts -- outflows accompanied by heavy rain at the surface -- are predominant in the southeastern United States.

The reflectivity factor at the leading edge of the outflow winds was often significantly lower than that in the precipitation cores that generated the microbursts. As stated in Section II, both of our radar systems have a minimum detectable signal level corresponding to reflectivity factors of 0 dBz over the range interval of operational interest. In a few cases, it was clear that microburst outflows penetrated into regions with echo strengths below this threshold so that part of the microburst wind field could not be measured. This circumstance did not, however, prevent either radar from measuring at least part of the velocity shear signature since the center of divergence remained coupled to the area of heavy precipitation.

## C. Microburst Velocity Shear

The scan-by-scan distribution of radial velocity shear in these microbursts is plotted in Figure III-2. Values less than 10 m/s are from outflows that exceeded this operational threshold over only part of their life cycle. The shear estimates are the difference between the maximum receding and approaching radial velocities in an outflow subject to the constraint that these velocity extrema occurred within a 4 km range interval.

The frequency of outflow intensities decreased approximately linearly from the microburst threshold of 10 m/s to the largest measured velocity differential of 33 m/s. These measurements are consistent with previous data [13] showing that strong microbursts ($\Delta V_R > 25$ m/s) represent the extreme end of a population of weak to moderate outflows. The relatively small number of scans showing differential radial velocities less than 10 m/s is probably an observational bias since our site operators in many cases did not begin recording data until a microburst was in progress.

## D. Microburst Outflow Height

A critical parameter affecting the capability of an airport surveillance radar to measure microburst winds is the height of the outflow layer. For each RHI scan through a microburst, we measured the altitude at which the outflow velocity dropped to half of its near-surface value. This was done separately for the point of strongest approaching and receding velocities. The distribution of these outflow heights, plotted in Figure III-3, is again consistent with earlier measurements of microbursts [1,13] in the southeastern United States. The measured heights varied from less than 100 m to about 1000 m with a median value of 350 m.

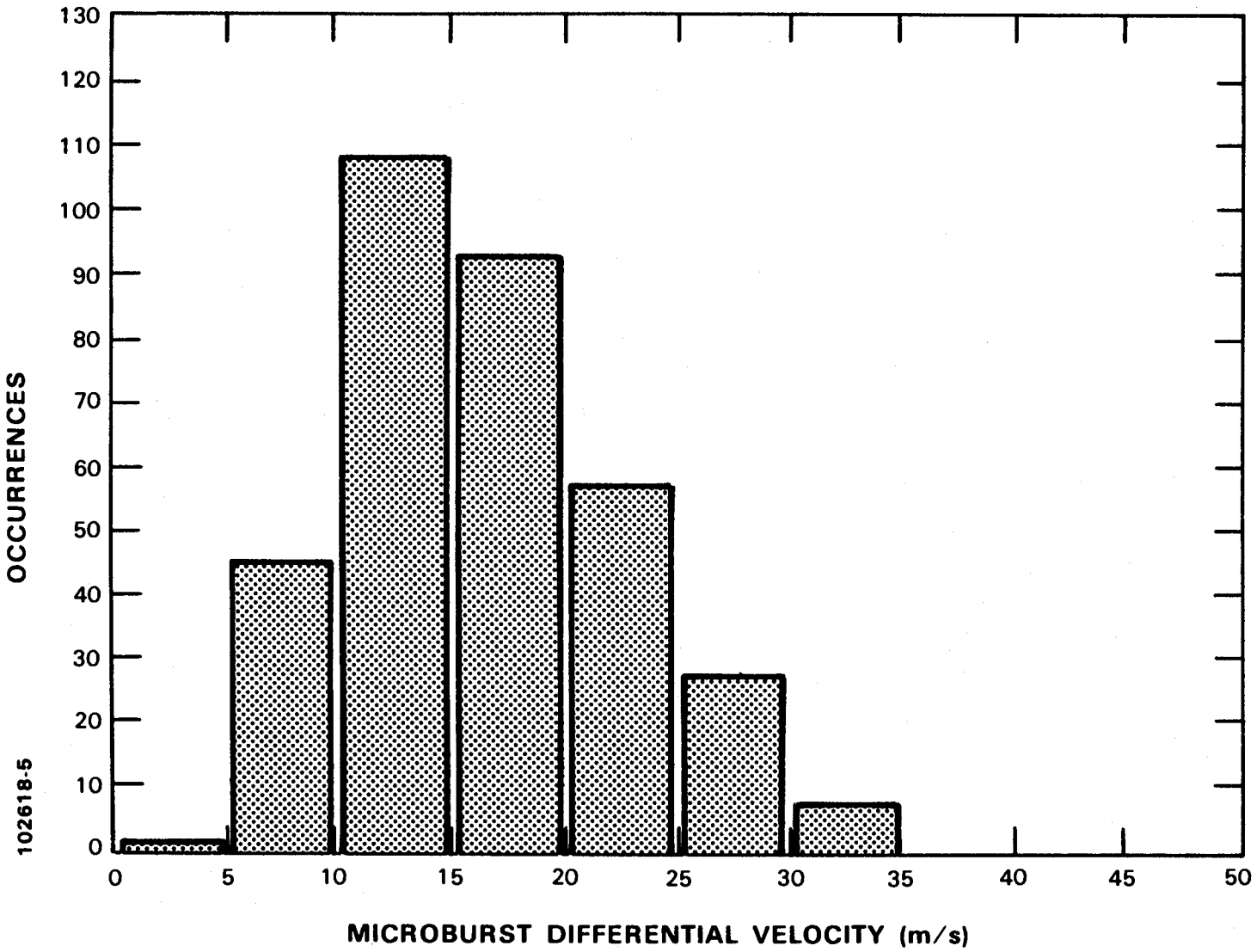


Figure III-2 Distribution of differential radial velocity measured in microbursts near the ASR testbed facilities in 1987.

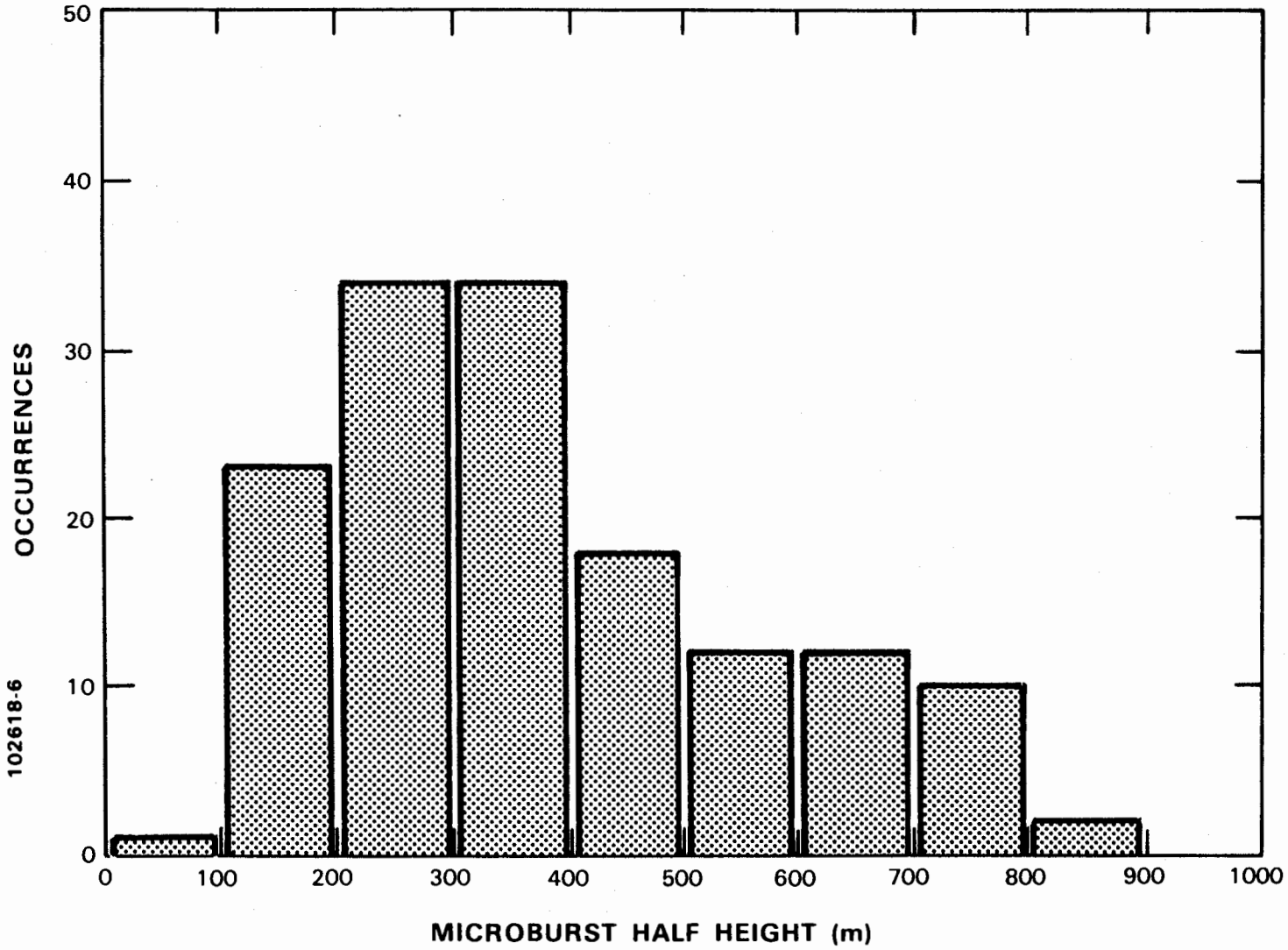


Figure III-3 Distribution of height at which outflow radial winds dropped to half of their maximum value for 1987 Huntsville microbursts.

E. Gust Fronts

Table III-2 lists parameters associated with gust fronts that passed near the testbed facility. Listed for each event are the date, time interval over which the gust front was observable in the weather radar data, range of closest approach, reflectivity factor and maximum radial velocity (approaching or receding).

Table III-2: Gust Front Parameters

| Date | Time (UT) | Closest Range (km) | Max dBz | Max $\lvert V_R \rvert$ (m/s) |
|---|---|---|---|---|
| 14 June | 18:45-19:57 | 0 | 20 | 12 |
| 24 June | 23:54-00:05 | 5 | 20 | 9 |
| 09 July | 18:19-19:10 | 0 | 20 | 15 |
| 09 July | 20:58-21:20 | 9 | 10 | 5 |
| 13 July | 21:52-22:28 | 0 | 25 | 21 |
| 17 July | 21:53-22:52 | 2 | 15 | 9 |
| 23 July | 17:08-18:33 | 0 | 15 | 10 |
| 27 July | 22:58-23:58 | 5 | 30 | 12 |
| 01 August | 21:00-21:19 | 12 | 15 | 8 |
| 03 August | 19:49-20:21 | 0 | 15 | 8 |
| 04 August | 20:05-20:40 | 0 | 15 | 10 |
| 17 August | 18:34-19:29 | 0 | 15 | 8 |
| 18 August | 00:47-01:35 | 0 | 20 | 19 |
| 18 August | 21:38-22:26 | 0 | 30 | 21 |
| 10 September | 22:27-22:43 | 7 | 20 | 15 |
| 11 September | 23:44-23:57 | 7 | 15 | 10 |
| 12 September | 00:08-00:45 | 8 | 20 | 10 |
| 12 September | 00:44-01:54 | 0 | 25 | 13 |

Many of these events were "ring" gust fronts generated by isolated thunderstorm cells. The reflectivity factors and outflow velocities in this class of gust front were low, making measurement with the radar systems challenging. Other gust fronts, for example that on 18 August (21:38-22:26), were generated by line storms and exhibited longer lifetimes, higher radar reflectivities and larger wind speeds.

# IV. SIGNAL PROCESSING FOR RADIAL VELOCITY MEASUREMENT IN THUNDERSTORM OUTFLOWS

## A. Overview of Principal Issues

Figure IV-1 illustrates the data processing steps that would be required to generate automatic wind shear hazard reports using data from an airport surveillance radar. Because of the on- or near-airport location of ASRs and the necessity of using the low receiving beam [1] for outflow wind measurements, weather-to-ground clutter power ratios in the area of operational concern will often be small [3]. References [1] to [3] examined the capabilities of airport surveillance radars to measure winds in the presence of ground clutter and concluded that ground clutter obscuration would be negligible even at short range provided that the reflectivity factor in a thunderstorm outflow is greater than about 20 dBz.

Once ground clutter has been removed from the weather echo, two additional factors affect the accuracy of low altitude radial velocity measurements made using an ASR. One is the high estimate variance associated with the short coherent processing intervals of an ASR and the large spectrum widths of weather echoes as measured with its fan elevation beam. Analysis by Zrnic' [14] implies that 10-sample mean velocity estimates formed using the pulse-pair method would have a standard deviation of 3 m/s assuming:

(i) signal to noise ratio greater than 20 dB;

(ii) velocity spectrum width of 10 m/s. As described later in this section, echo spectra measured in microbursts with an ASR exhibit large width owing to vertical shear in the wind field.

When the signal to noise ratio is small, the estimate variance could be greater still.

While this uncertainty is large relative to the velocity error in conventional slow-scanning weather radar systems, there are several approaches available for reducing the uncertainty to acceptable levels. Spatial smoothing can be employed since thunderstorm outflows extend over many ASR resolution cells at the ranges of operational concern. Reference [3] simulated ASR microburst measurements using a median filter operating on the velocity estimates in 9 adjacent range-azimuth cells and showed that the smoothed velocity field correlated well with the input microburst model. An alternate approach was considered in [2] where temporal averaging of data from six successive antenna scans reduced the standard deviation of simulated ASR velocity estimates to 1 m/s or less. The resulting update period for the wind field -- thirty seconds -- would still be adequate to track the evolution of thunderstorm outflows.

Since our current off-line processing facilities severely limited the number of ASR scans that could be handled, we chose to employ only the nine-cell, spatial median filter for the fields analyzed in this report. In rare cases, the residual "noise" prevented automatic detection of microburst signatures that were apparent to a human observer. In addition, it was clear that differential velocity measurements would have been more stable had additional smoothing been applied.

A more significant problem for velocity estimation results from the bias introduced when energy is scattered into the elevation fan beam from precipitation aloft. This overhanging precipitation normally has a radial velocity markedly different from that in the outflow layer. As a result, mean velocity estimates are

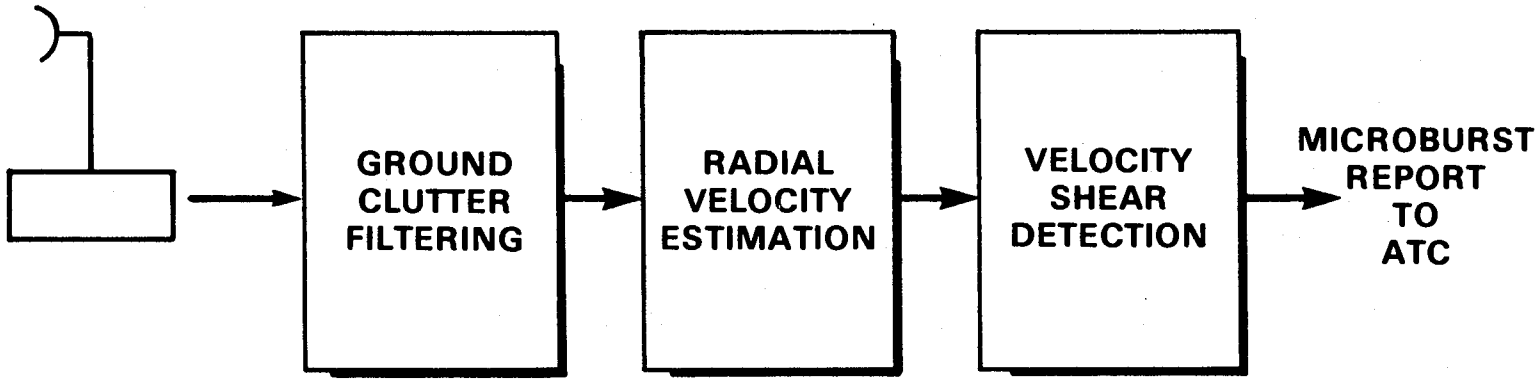


Figure IV-1 Overview of principal processing steps required for generating automatic microburst alarms for air traffic controllers from ASR data.

intermediate between the outflow velocity and winds aloft. The magnitude of the bias is a function of outflow height and range from the radar. In reference [1] we showed that for microbursts with outflow winds extending less than 500 m AGL this bias becomes significant well inside the 10 km range interval where ASR wind shear measurements would be operationally useful.

The final operation illustrated in Figure IV-1 is automatic identification of the radial velocity and reflectivity signatures of low altitude wind shear hazards. Algorithms developed for the TDWR have been described in references [15-17] and are currently undergoing design validation. While these algorithms form a basis for developing an automatic LAWS detection capability for airport surveillance radars, they have required modification to perform reliably given the characteristics of ASR wind measurements.

The remainder of this section uses data from our testbed radars to evaluate the capability of an ASR to measure microburst wind shear. As predicted from earlier analysis [1,3], the reflectivity factor in Huntsville microbursts is sufficiently high that receiver noise and ground clutter obscuration were not major issues for microburst wind measurement. Our focus, therefore, will be assessment of the impact of overhanging precipitation on the ASR measurements and evaluation of data processing approaches for ameliorating the resultant shear estimate bias.

## B. Velocity Spectra in Microburst Outflows

Figure IV-2 shows examples of velocity spectra measured with the testbed airport surveillance radar in the radial velocity cores of Huntsville microbursts. The following procedure was used to estimate the spectra:

(i) the signals were adaptively filtered [3] to remove ground clutter if necessary. In most of the cases displayed, however, the weather reflectivity factor in the microburst velocity cores was sufficiently high that no filtering was required;

(ii) 34-sample data sequences -- corresponding to the time period for the antenna to scan two azimuthal beamwidths -- were Hamming windowed, zero-filled to 64 points and transformed using the Fast Fourier Transform (FFT) algorithm;

(iii) the magnitude squared of the Fourier transforms in three adjacent range gates were averaged.

The resulting spectral estimates are therefore smoothed over 2.8° azimuth and 360 m in range. The velocity resolution is 2 m/s.

The spectra are displayed in order of increasing range of the microbursts' centers. Both high (dashed lines) and low (solid lines) beam spectra are displayed. The plots in the left column are for the approaching radial velocity cores of the microbursts and those in the right column are for the receding cores. The spectra have been normalized so that the area under the curves is unity. For reference, low altitude mean radial velocities measured at the same locations and times with the pencil beam weather radar are indicated by dashed vertical lines.

The effect of the ASR's elevation fan beam and the strong vertical shear in the wind field above microbursts is clearly evident. The spectra are significantly broader than those measured in microbursts with pencil beam Doppler weather radars and show complex structure. Spectrum widths of both high and low beam

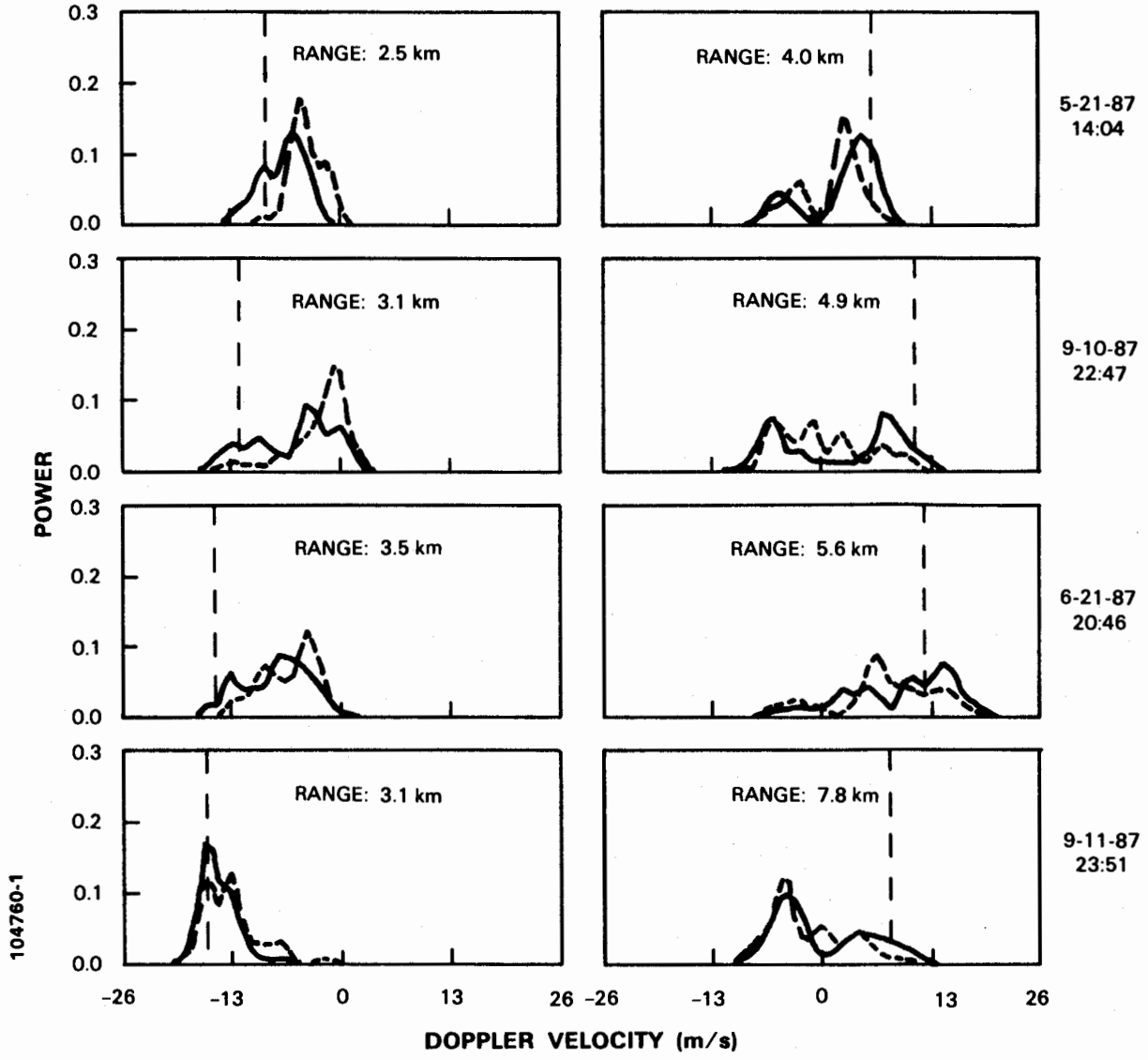


Figure IV-2 Velocity spectra measured with ASR in approaching (left) and receding (right) radial velocity cores of example microbursts. The ordinate is relative power in linear units. Spectra are plotted for both low (solid) and high (dashed) beam signals. Dashed vertical lines show mean velocities measured by pencil beam radar at 0.7 degrees elevation at same locations and times.

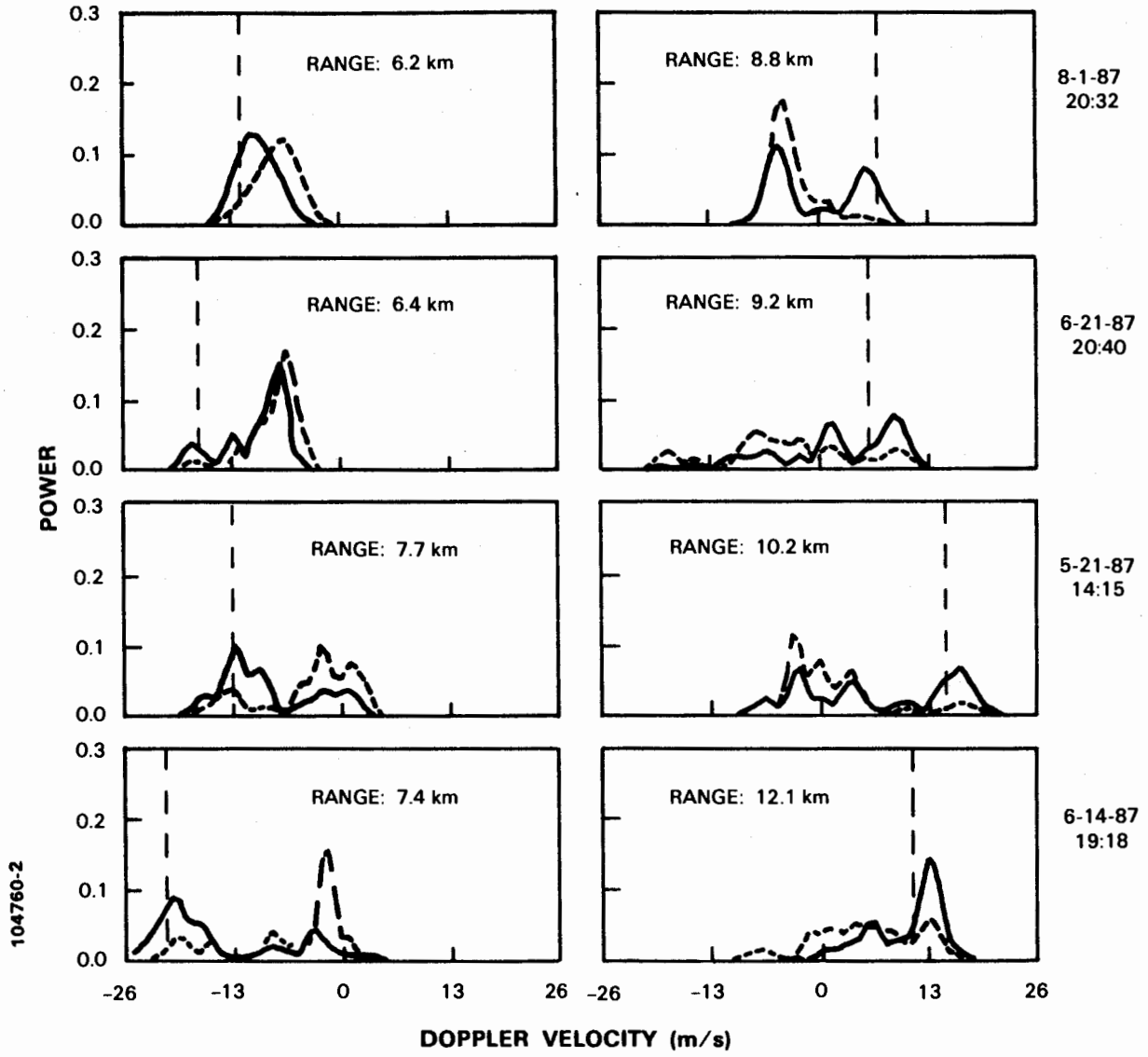


Figure IV-2 Continued

echoes are often in excess of 5 m/s (Figure IV-3) and tend to increase with range as the fan beam intercepts a larger altitude interval (i.e. more radial velocity variation).

Comparison of the spectra with the pencil beam radar low-altitude velocity measurements shows that the velocity components associated with the microburst outflow are often far down in power relative to interference from overhanging precipitation. As would be expected, the relative power at the outflow velocity is smaller in the high beam than in the low beam. Figure IV-4 plots the resulting bias in power-weighted ASR mean velocity estimates relative to simultaneous measurements with the pencil beam Doppler radar. Square symbols correspond to the low beam ASR signals and triangles to the high beam. The biases are plotted as functions of the range from the radars to the point of measurement. Overlaid lines are regressions to the data, performed separately for the low (solid) and high (dashed) beams. As predicted in reference [1], the plot indicates that:

(i) the sign of the velocity estimate error produced by overhanging precipitation echoes results in an underestimate of the surface winds (i.e. negative bias) since the precipitation aloft is normally moving at a lower radial velocity or even in the opposite direction;

(ii) this bias is greater when signals from the high beam are used rather than the low beam;

(iii) on average, the magnitude of the bias increases with range for both beams. However, the underestimate may be significant even for measurements within a few kilometers of the radar. This is consistent with the analysis in [1] and our previous observation (Figure III-3) that half of the outflows measured in Huntsville extended 350 m or less above the surface.

Thus the impact of overhanging precipitation on low altitude velocity estimates with an ASR is significant throughout the area of operational concern. The following subsection describes data processing methods that attempt to compensate for the spectral contamination produced by scatterers aloft. These methods are evaluated in Section VI through comparison of the resulting velocity estimates with simultaneous measurements from the pencil beam weather radar.

## C. Techniques for Estimating Low Altitude Radial Velocity Shear

The power spectrum, $\tilde{S}$, measured in an range-azimuth cell by a fan beam ASR can be expressed in terms of the elevation angle resolved field of velocity spectra, $S$, as:

$$\tilde{S}(\phi,R,v) = \frac{\int_0^{\frac{\pi}{2}} S(\theta,\phi,R,v) B_{TR}(\theta)\, d\theta}{\int_0^{\frac{\pi}{2}} B_{TR}(\theta)\, d\theta} \qquad (1)$$

where $B_{TR}(\theta)$ is the two-way elevation power pattern of the ASR antenna. The mean velocity seen by the ASR is therefore:

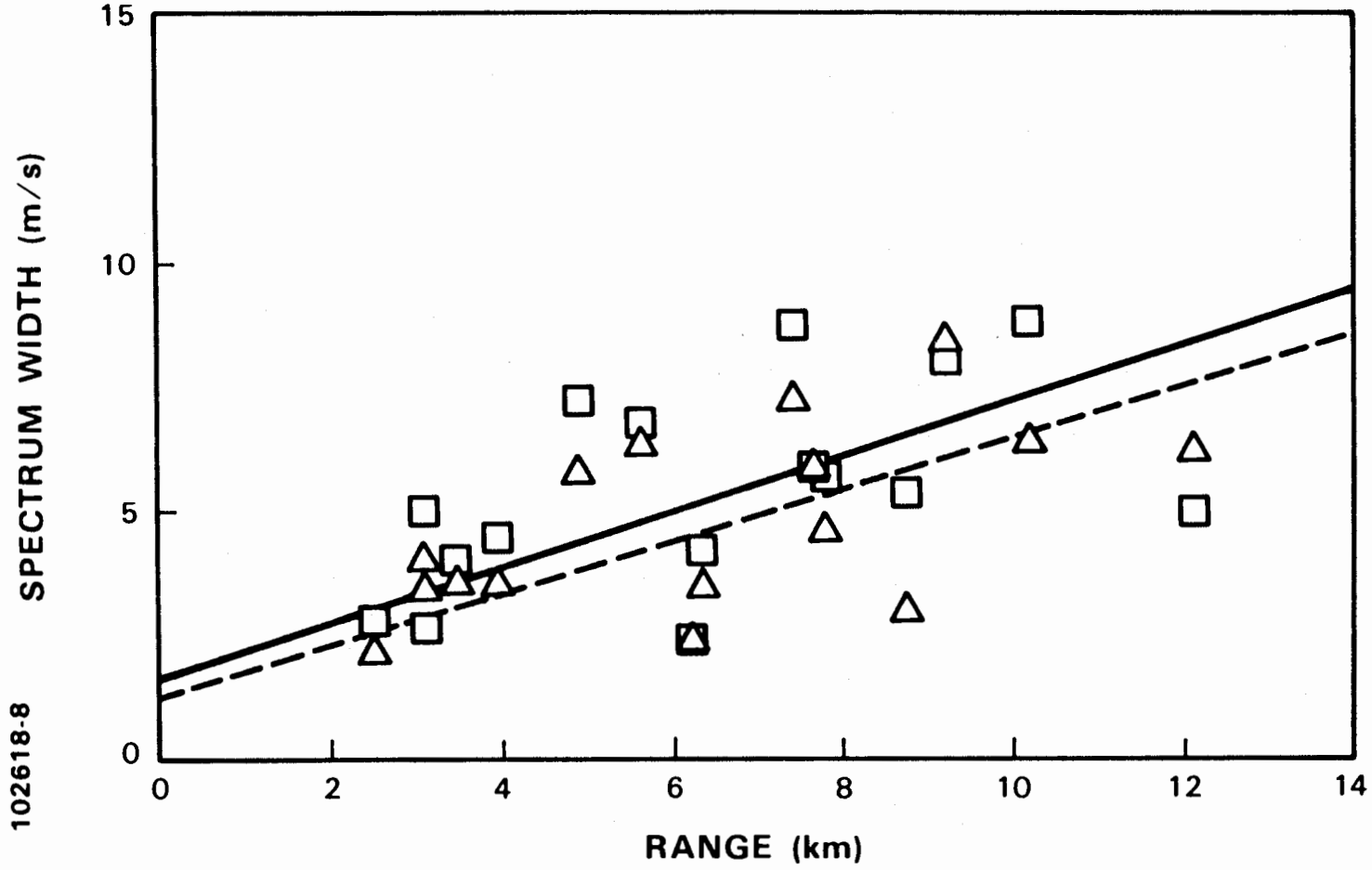


Figure IV-3 Velocity spectrum width versus range for microbursts treated in Figure IV-2. Low beam values are plotted with rectangles and high beam values with triangles. Solid (dashed) lines are linear regressions to the low (high) beam data.

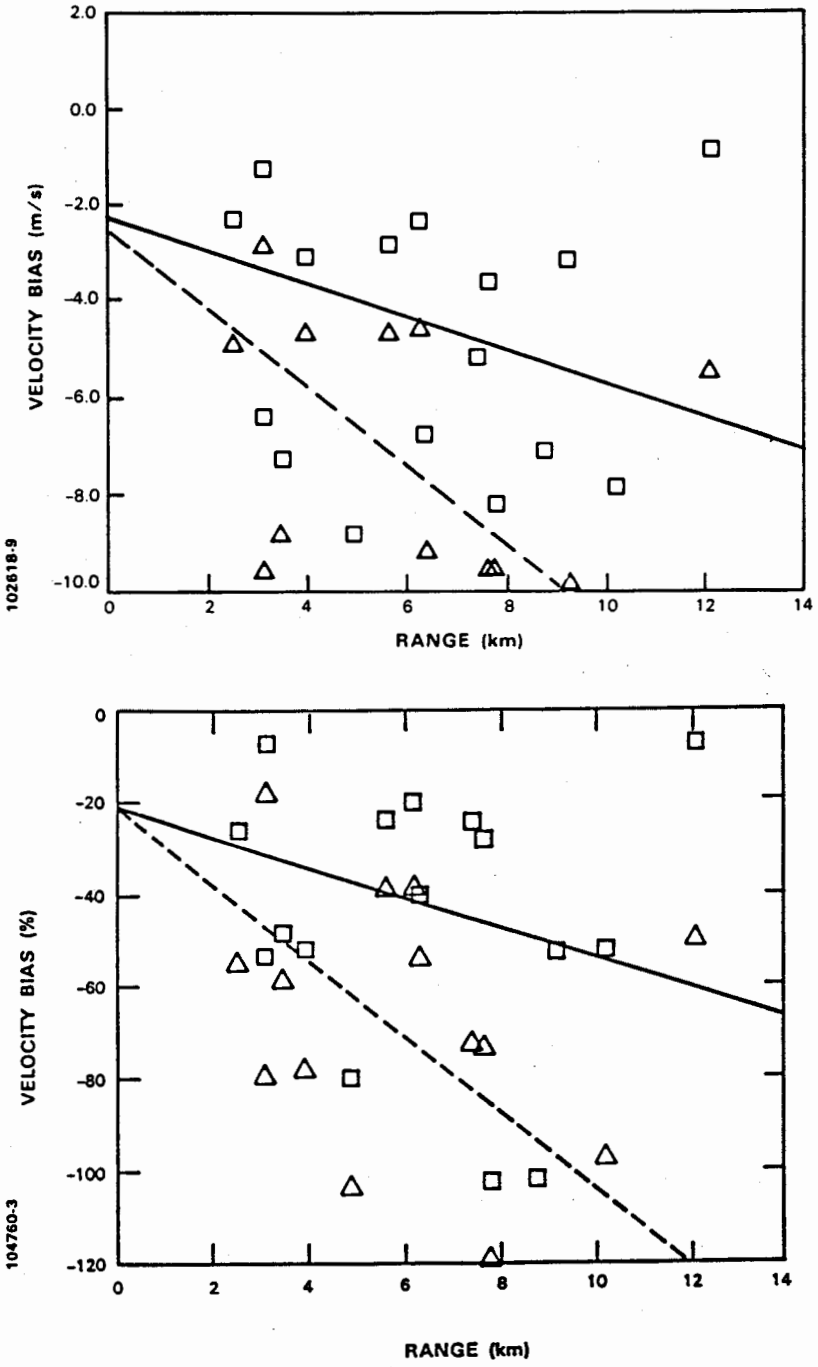


Figure IV-4 Difference versus range between mean velocity estimate from ASR and pencil beam weather radar for microbursts treated in Figure IV-2. Bias is expressed in velocity units (upper plot) and as a percentage (lower plot) of the near surface velocity measured by the weather radar. Low beam values are plotted with rectangles and high beam values with triangles. Solid (dashed) lines are linear regressions to the low (high) beam data.

$$\tilde{v}_M(\phi,R) = \frac{\int_{-\infty}^{\infty} v\ \tilde{S}(\phi,R,v)dv}{\int_{-\infty}^{\infty} \tilde{S}(\phi,R,v)dv}$$

$$= \frac{\int_0^{\frac{\pi}{2}} B_{TR}(\theta) \int_{-\infty}^{\infty} v\ S(\theta,\phi,R,v)dvd\theta}{\int_0^{\frac{\pi}{2}} B_{TR}(\theta) \int_{-\infty}^{\infty} S(\theta,\phi,R,v)dvd\theta} \qquad (2)$$

$$= \frac{\int_0^{\frac{\pi}{2}} B_{TR}(\theta) v_M(\theta,\phi,R)d\theta}{\int_0^{\frac{\pi}{2}} B_{TR}(\theta)d\theta}$$

This velocity estimate is the antenna pattern weighted integral over elevation angle of the mean velocity field. In going from the second to the third equality in (2), we assumed that the radar reflectivity factor is uniform over the altitude interval of concern and therefore cancels from the numerator and the denominator. If this is not the case, equation (2) and subsequent expressions in this section are readily modified by substituting $Z(\theta)B_{TR}(\theta)$ for $B_{TR}(\theta)$.

In estimating the low altitude radial velocity field, it would obviously be desirable to manipulate the data so that the upper limits of the elevation angle integrals above are replaced by $\theta_0$, an angle which is comparable to that subtended by the top of the microburst outflow layer and in general is much smaller than the angle at which the ASR's antenna gain becomes negligible. In attempting to effect this result, we consider two techniques that use data only from the low receiving beam and two techniques that combine information from the high and low receiving beams.

1. Correction of Low Beam Shear Estimates based on an Assumed Outflow Height

The radial velocity differential measured across a microburst by an ASR can be expressed from equation (2) as:

$$\Delta\tilde{V} = \frac{\int_0^{\theta_0} B_{TR}(\theta)(v_M(\theta,\phi,R_2)-v_M(\theta,\phi,R_1))d\theta + \int_{\theta_0}^{\frac{\pi}{2}} B_{TR}(\theta)(v_M(\theta,\phi,R_2)-v_M(\theta,\phi,R_1))d\theta}{\int_0^{\frac{\pi}{2}} B_{TR}(\theta)d\theta} \qquad (3)$$

where $R_1$ and $R_2$ are respectively the ranges of the approaching and receding cores of the microburst. We will assume that in a microburst, the strongest differential radial velocities occur near the surface so that the second integral in the numerator of equation (3) is small relative to the first. This assumption will be justified

if the radial velocity difference associated with compensating convergence aloft (Figure I-1(a)) is less than that in the surface outflow or if integration over the large elevation angle interval from $\theta_0$ to the top of the beam washes out radial velocity differences present at a single altitude.

Neglecting the second term in equation (3), the velocity difference measured across a microburst using a mean velocity estimator on the ASR signal is related to the "true" (i.e. averaged from the surface to $\theta_0$) low altitude radial velocity differential by a multiplicative correction factor:

$$C(\theta_0) = \frac{\int_0^{\frac{\pi}{2}} B_{TR}(\theta)\, d\theta}{\int_0^{\theta_0} B_{TR}(\theta)\, d\theta} \tag{4}$$

The obvious weakness of this approach is that the height of microburst outflow winds varies over a full order of magnitude (Figure III-3); thus a correction tailored to the average outflow height may give a significant over- or under-estimate of the wind shear in any particular event.

Table IV-1 compares velocity differences measured with the pencil beam weather radar to simultaneous estimates from the ASR data using this technique and additional methods described below. For this simple, low beam correction the angle $\theta_0$ is taken as that subtended by a 350 m deep outflow (i.e. the median of the distribution in Figure III-3) at a range half-way between the approaching and receding radial velocity cores of the microburst. While the shear estimates are for the same microbursts treated in Figure IV-2, the values may differ from what would be directly calculated from the plotted spectra. This is because the maximum approaching and receding radial velocities estimated from the ASR data may occur in resolution cells slightly displaced from the corresponding maximum velocity cores measured with the pencil beam radar.

Table IV-1: Comparison of ASR Velocity Estimation Techniques

| Date/Time | Outflow Height (m) | Pencil Beam Radar $\Delta V$ (m/s) | Low Beam Corrected | Low/High Beam Corrected | High Pass Filtered | Dual Beam |
|---|---|---|---|---|---|---|
| 9-11 23:51 | 250 | 27 | 26 | 23 | 23 | 27 |
| 6-21 20:46 | - | 27 | 24 | 27 | 22 | 24 |
| 9-10 22:47 | 200 | 24 | 22 | 23 | 24 | 25 |
| 5-21 14:04 | 650 | 15 | 12 | 12 | 16 | 15 |
| 6-14 19:18 | 700 | 32 | 49 | 27 | 32 | 31 |
| 5-21 14:15 | 650 | 28 | 47 | 32 | 27 | 28 |
| 6-21 20:40 | - | 23 | 21 | 18 | 20 | 21 |
| 8-1 20:32 | 400 | 19 | 27 | 19 | 20 | 18 |
| Average $\frac{\Delta V_{ASR}}{\Delta V_{TRUE}}$ | | | 1.14±.35 | 0.92±.12 | 0.95±.10 | 0.97±0.05 |

For these eight cases, the average ratio of estimated to true shear is 1.14 using the simple low beam shear correction factor in (4) but, as predicted, the error on

individual cases may be unacceptably large. There is moderate correlation between the measured heights of the outflows and the sign and magnitude of the ASR estimate error -- the correlation coefficient between ($H_{OUTFLOW}$ - 350 m) and ($\Delta V_{ASR} - \Delta V_{TRUE}$) is 0.74. The imperfect correlation indicates that our assumption of negligible radial shear in the winds aloft may not always be met.

This shear correction technique (and that considered in Section IV-C-2) are implemented as part of the hazard detection algorithm after regions of radial velocity shear have been identified from the uncorrected mean velocity field. This implementation is discussed further in Section V.

2. Correction of Shear Estimates Using High and Low Beam Data

The correction factor in equation (4) is different for the high and low beams owing to the different receive beam patterns in the integrands. An estimate for the effective elevation angle subtended by an outflow may be obtained by varying $\theta_0$ until the high and low beam corrected shear estimates are equal. As long as the measured velocity differential in the high beam is less than or equal to that in the low beam -- a circumstance always realized in microburst wind shears -- there exists a unique value of $\theta_0$ that yields the same shear estimate from the low and high beam measurements. This method removes the unrealistic assumption of constant outflow height but is still subject to errors caused by neglect of the second integral in the numerator of equation (3).

The resulting velocity shear estimates are listed in the fifth column of Table IV-1. This method does not produce the large shear overestimate that occurred when a static correction factor was applied to deep outflows such as those on 21 May (14:15) and 14 June (19:18). The estimates on average are 0.92 of the pencil beam radar measurements with a (RMS) relative error of 0.12. Errors in velocity shear estimates using this method are the result of:

(i) neglect of the second integral in equation (3);

(ii) unequal elevation angles subtended by the approaching and receding portions of a microburst outflow;

(iii) statistical uncertainty in the low and high beam shear estimates.

The last factor could be ameliorated by further smoothing of the velocity estimates -- for example, through temporal averaging over successive antenna scans.

3. High Pass Filtering Prior to Velocity Estimation

As stated previously, it would be desirable to manipulate the ASR signals so that a weighting function:

$$G(\theta) = \begin{cases} 1 & \theta \leq \theta_0 \\ 0 & \theta > \theta_0 \end{cases} \qquad (5)$$

is applied to the integrands in equation (2). If the radial velocity versus elevation angle (i.e. height) relationship in a particular resolution cell can be inverted to produce a function $\theta(v_M)$, then it would be possible to achieve this weighting by filtering the weather echoes in the velocity domain using a transfer function given by the composition of $G(\theta)$ with $\theta(v_M)$.

Microbursts in the southeastern U.S. are normally produced by air mass

thunderstorms that form in the weakly sheared environment characteristic of summer months. Anderson [18] suggested that, under these conditions, the strongest absolute radial velocities in microbursts would occur near the surface and that the magnitude of velocities would decrease rapidly above the outflow layer. As an approximation to this model, the magnitude of the radial velocity would vary with elevation angle as:

$$|v_M(\theta)| = |v_M(\theta=0)| - \Gamma(\theta) \tag{6}$$

where $\Gamma(\theta)$ is a positive, monotonically increasing function bounded by zero below and $|v_M(\theta=0)|$ above. Compositing the inverse of this profile with equation (5) gives as the desired transfer function:

$$H(v) = \begin{cases} 0 & |v| \leq |v_M(\theta=0)| - \Gamma(\theta_0) \\ 1 & |v| > |v_M(\theta=0)| - \Gamma(\theta_0) \end{cases} \tag{7}$$

which is simply a high pass filter with stop bands extending to the radial velocity associated with the top of the outflow layer. Clearly not all microbursts exhibit the same radial velocity shear (see Figure III-2); in addition, the approaching and receding velocity cores in a microburst may not exhibit equal velocity magnitudes. Thus without *a priori* knowledge of a particular microburst's radial velocity structure, the high pass filter transfer function must be chosen based on representative microburst properties. The median differential radial velocity we measured in Huntsville microbursts was 18 m/s (Figure III-2) indicating a typical maximum approaching or receding radial velocity magnitude of 9 m/s. For the examples in this report, we will set the filter stop bands at 2/3 of this value.

Figure IV-5 shows the low beam velocity spectra of the microbursts considered previously after convolving the signals with a high pass filter whose 3 dB stop bands extend to ±6.0 m/s. The spectra have been renormalized so that, as previously, their integrated power is unity. Comparison with Figure IV-2 shows that in many of the examples, the filtering has removed much of the spectral contamination associated with weather above the outflow layer. In some cases, for example the receding core spectra from 1 August (20:32 UT), 10 September (22:47 UT) and 11 September (23:51 (UT), the radial velocity of the overhanging weather echoes is large in magnitude and with sign opposite to that in the outflow layer. In this situation, the interfering signal falls into the pass bands of the filter and therefore still contributes a significant bias to mean velocity estimates.

The sixth column of Table IV-1 lists the radial velocity shears calculated using this technique. The estimated values are on average .95 of the true shear with a standard deviation of .10. Note that in several cases, the listed ASR shear estimates are substantially higher than would have been calculated from the corresponding spectra in Figure IV-5. As stated before, this occurs because the maximum velocities estimated using the ASR data may not occur at the same location as the radial velocity cores measured with the pencil beam radar. Section VI-A illustrates that in these cases, the high pass filter successfully removed overhanging precipitation interference from only part of the outflow region, thereby substantially reducing the area of either the approaching or receding radial velocity core.

4. Differential Low-High Beam Power Spectra

Figure IV-6 plots the effective one-way elevation antenna patterns for the ASR-9's high and low beams. (The high beam is passive so that these patterns are the square root of the product of the low beam transmit pattern and the high

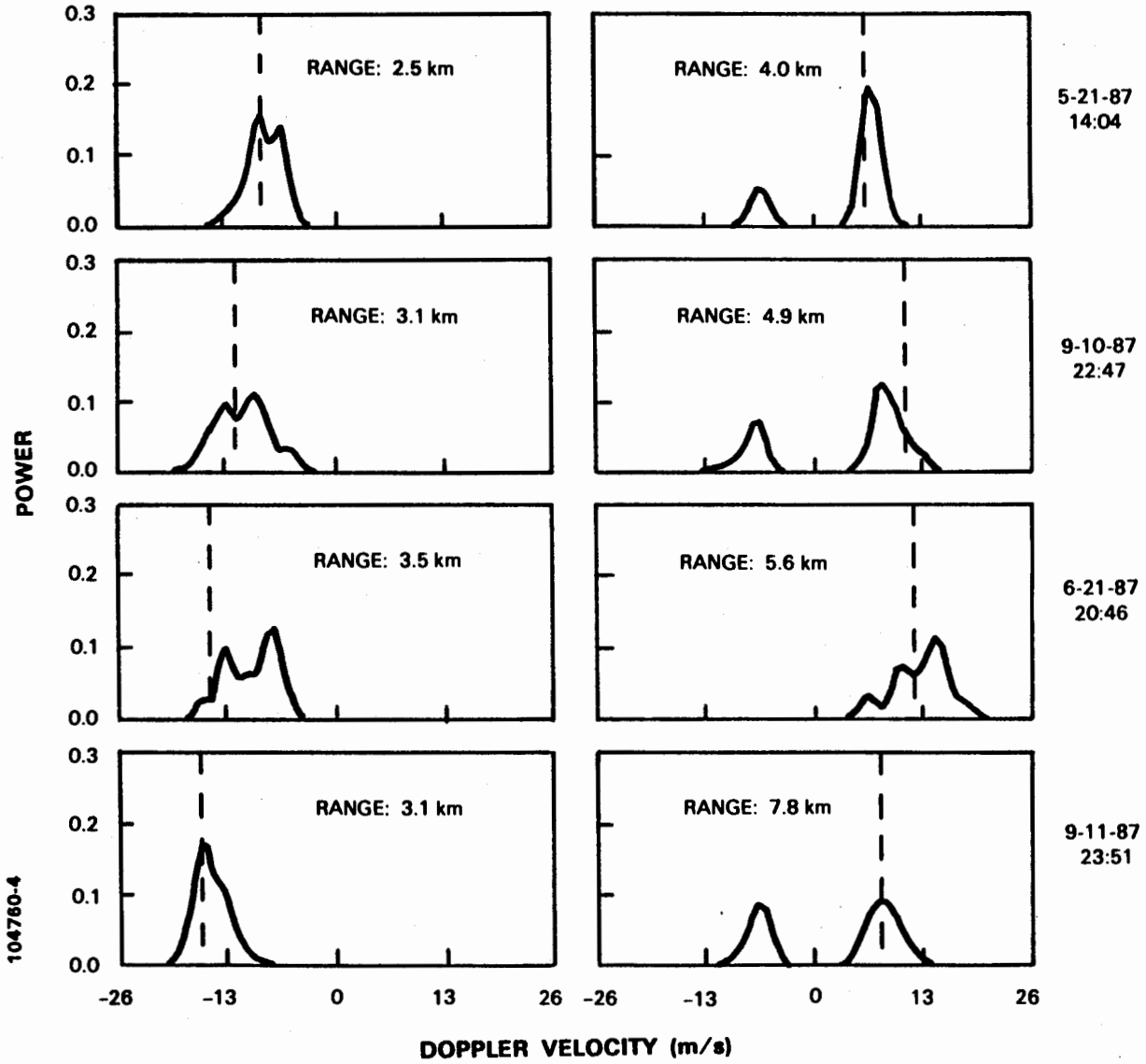


Figure IV-5 Microburst velocity spectra measured with ASR. The figure shows the low beam data previously treated in Figure IV-2 except that here, the signals have been convolved with a high-pass filter whose stop bands extend to ±6 m/s. Vertical dashed lines are simultaneous low altitude velocity estimates from pencil beam radar.

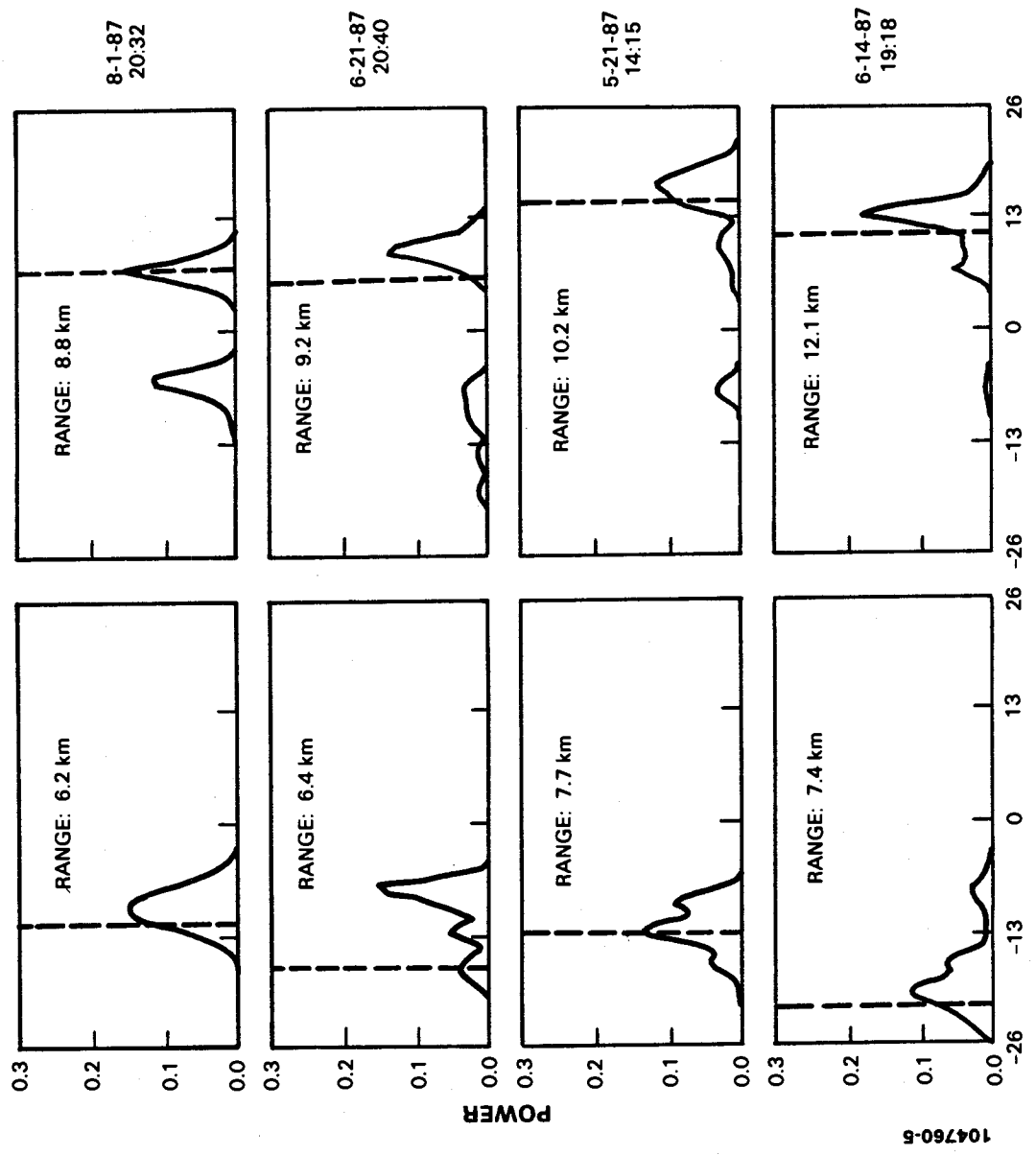


Figure IV-5 Continued.

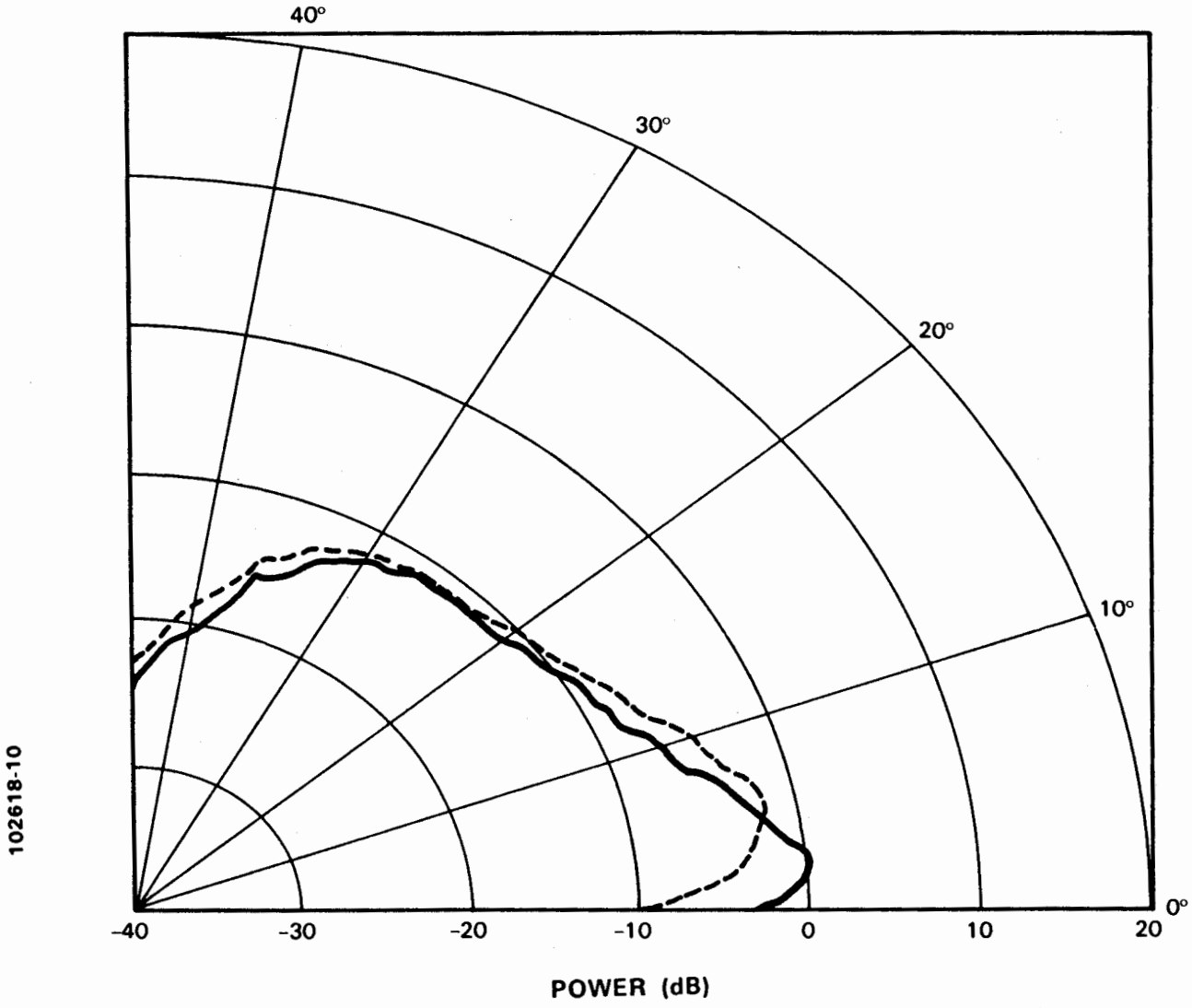


Figure IV-6 Effective one-way elevation beam patterns for an ASR-9. Solid line is low beam pattern (normalized to unity gain at peak response point). Dashed line is high beam pattern.

or low beam receive pattern.) Below about 4° elevation angle, the low beam gain exceeds that in the high beam with a maximum difference (two-way) of 14 dB on the horizon. Above 4° elevation angle, the low beam gain is everywhere less than or equal to that in the high beam. As is obvious from inspection of Figure IV-2, this elevation angle dependent gain difference provides information on the function $\theta(v_M)$ which can be used to filter the spectral components associated with overhanging precipitation. †

The algorithm we currently employ forms a mean velocity estimate from the low-high beam "difference" spectrum:

$$\tilde{S}_{Diff}(\phi,R,v) = \begin{cases} \tilde{S}_{Low}(\phi,R,v) - \tilde{S}_{High}(\phi,R,v) & v_a \leq v \leq v_b \\ 0 & otherwise \end{cases} \tag{8}$$

After adaptive ground clutter filtering, normalized low and high beam spectra are calculated as described in Section IV-B using running averages (over three successive range gates) of 64-sample FFTs. The limits $v_a$ and $v_b$ are found by determining all runs of consecutive frequency lines with $\tilde{S}_{Low}$ greater than $\tilde{S}_{High}$ and selecting that run for the velocity estimate with the greatest integrated power in $\tilde{S}_{Diff}$.

The resulting velocity estimate is related to the radial wind profile by:

$$\tilde{v}_{Diff}(\phi,R) = \frac{\int_0^{\theta_C} (B_{Low}(\theta) - B_{High}(\theta)) v_M(\theta,\phi,R)\, d\theta}{\int_0^{\theta_C} (B_{Low}(\theta) - B_{High}(\theta))\, d\theta} \tag{9}$$

where $\theta_C$, the crossing point of the normalized high and low beam elevation patterns, equals 3.2° if the antenna tilt is 1°. If the radial winds in a microburst decrease linearly with elevation angle (height) above the surface, it is readily shown from (9) that $\tilde{v}_{Diff}$ equals the velocity at an elevation angle given by the centroid of the positive lobe of the beam pattern difference function $B_{Low} - B_{High}$. This is at an angle of 1.3°, corresponding to a height of 110 m at 5 km range and 230 m at 10 km range.

Figure IV-7 plots the spectra $\tilde{S}_{Diff}$ defined by equation (10) for the microbursts considered previously. The resulting functions are considerably narrower than the input spectra and are localized in velocity space near the mean low altitude velocity measured by the pencil beam radar. As seen from table IV-1, the velocity estimates generated using this technique correspond well to the pencil beam measurements. On average, the estimated shear for these eight examples was .97 of the true value with a standard deviation of .05.

5. Coherent Combination of Signals from Low and High Beams

Reference [1] considered two techniques for estimating low altitude winds which involved combination of low and high beam signals in the time domain. In order to compute the complex weights to be applied to the signals prior to their combination, these methods required knowledge of the high-low beam phase difference

† It has come to our attention that David Atlas [19] has proposed a concept for measuring near surface winds with an airport surveillance radar, using a low-high beam spectral differencing technique.

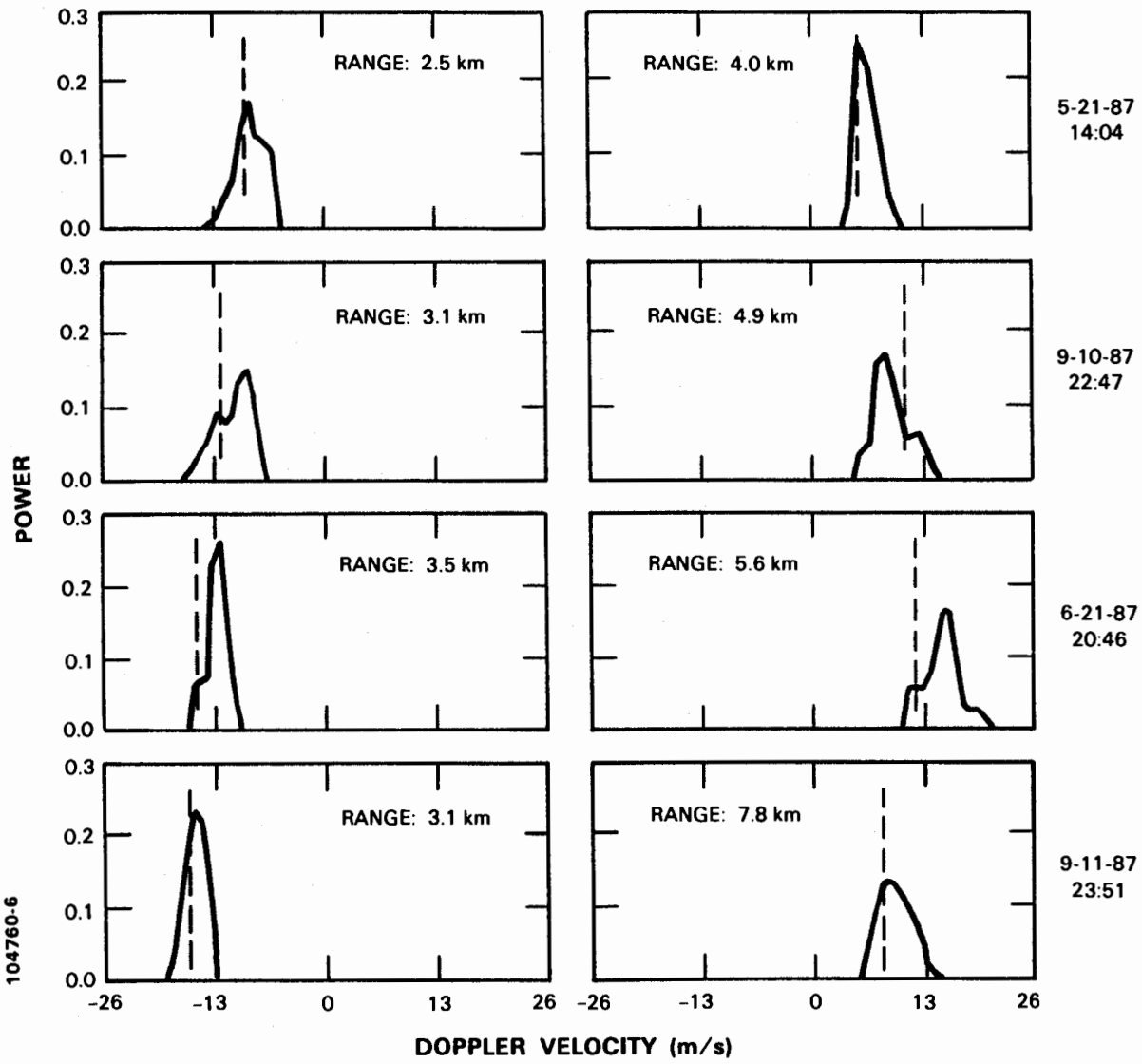


Figure IV-7 Microburst velocity spectra estimated by differencing normalized low and high beam spectra as in equation (8). Vertical dashed lines are simultaneous low altitude velocity estimates for pencil beam weather radar.

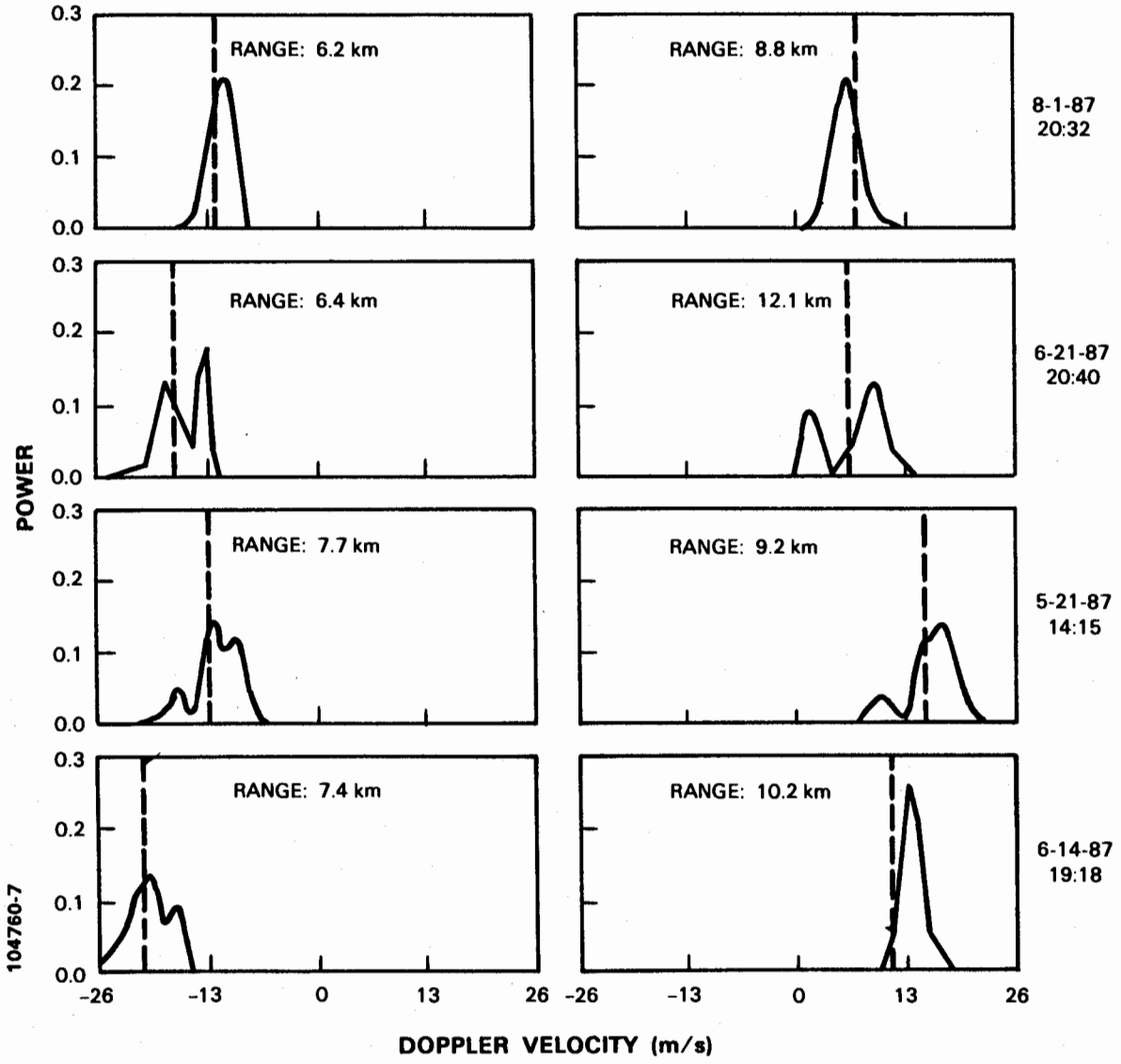


Figure IV-7 Continued.

as a function of elevation angle. These techniques were tested using simulations [1] and showed improvement relative to mean velocity estimates from the low beam for measurement of low altitude winds.

Anderson [18] is investigating the use of the phase of the cross-spectral density of low and high beam weather signals as another means of mapping ASR radial velocity spectral components to elevation angle. Given knowledge of the differential low-high beam phase pattern, this technique could provide three dimensional weather reflectivity and radial velocity fields, subject to ambiguities caused by wrap-around of the phase difference. For a proof of concept, Anderson used ground clutter sources to determine the phase difference for scatterers at low elevation angle, then selected corresponding weather echo spectral components to successfully estimate the low altitude radial velocity field in a microburst.

Since we have no measurements of the antenna phase patterns for our testbed ASR, these techniques have not been pursued extensively to date. We plan in future to accomplish the phase measurement by observing targets of opportunity (aircraft whose altitude is known from beacon reports and ground clutter) over a period of time.

## V. MICROBURST DETECTION ALGORITHM

Air traffic controllers have neither the time nor the expertise to examine complex radial velocity fields from a weather radar for the presence of hazardous wind shear. This section describes an algorithm directed at automatically detecting microbursts from the radial velocity field estimated using ASR signals. Given a scalar field of radial velocities on a range-azimuth coordinate grid, the algorithm identifies regions of large, positive radial velocity gradients that have spatial and temporal dimensions consistent with meteorological understanding of microbursts.

The difficulty in microburst identification arises from the complexity and variability in size, shape and strength of the target. The problem differs from typical visual image processing in which known characteristics of physical objects (such as surface continuity, rigidity, texture, color, shape, etc.) can be used to aid in image segmentation and subsequent image interpretation.

The constraints used here to guide image interpretation are uncertain at best. It is difficult, if not impossible to find a consistent range of values for hazard region size, shape, and strength which apply for all microbursts. Even experienced radar meteorologists may differ in their interpretation of a complex radial velocity image; different observers mark hazard locations differently and under or overestimate shear strength relative to the rules that have been adapted for algorithm scoring. Consistency has only been maintained by adhering to very specific requirements.

The challenge is made more difficult by possible data contamination. Sources include the statistical uncertainty in the $V_R$ estimate, ground clutter breakthrough, velocity biases due to overhanging precipitation, and interference from other airborne targets (airplanes, flocks of birds, emissions from other radars). Noise or biases in the data may prevent even a robust image processing algorithm from detecting real hazards.

The approach described is a modified version of the TDWR surface divergence algorithm [15]; this algorithm allows for a wide range of variability in "target" structure and intensity while at the same time maintaining high resistance to image degradation from the sources described above. Given that the microburst outflow signature is not totally obscured, the approach described has shown favorable initial results in automatically detecting and quantifying wind shear hazards.

### A. Performance Goals

Our goal has been to achieve as much as possible the requirements set by the FAA for the Terminal Doppler Weather Radar System. Those requirements which place demands on microburst detection algorithm performance include:

(1) *Hazard Definition:* Reports must include changes in wind speed which exceed 20 kts (10 m/s) and extend from .5 to 4 nmi.

(2) *Coverage:* The TDWR system must provide hazardous wind shear detection within a 6 nmi radius of the airport reference point.

(3) *Probability of Detection:* The probability of detecting an existing hazardous wind shear must be at least 90 percent.

(4) *Probability of False Alarm:* The probability of a wind shear report being false must not exceed 10 percent.

(5) *Location Accuracy:* The location and extent of reported events must be accurate to within .5 nmi.

(6) *Shear Strength Accuracy:* The magnitude of reported wind shear must be accurate to within 5 knots or 20 percent (whichever is larger) at least 95 percent of the time.

## B. The Microburst Divergent Shear Algorithm

The microburst detection algorithm described here incorporates the basic steps of Merritt's TDWR Microburst Divergent Outflow Algorithm [15], which was itself adapted from Zrnic' and Gal-Chen's algorithm for detecting divergence at storm tops [20]. A pseudo-code level description of this algorithm may be found in [21]. The algorithm's hierarchical feature extraction process consists of the three phases illustrated in Figure V.1.

### 1. Shear Segment Feature Identification

The first step of the detection process attempts to identify regions of divergent shear along individual radials of velocity measurements, tangential components of the shear not having been considered in this report.

The algorithm first searches radials of velocity measurements for runs of velocities generally increasing with range. This is accomplished by sliding a pattern search window outward along a radial. A shear segment is begun when a fixed number of contiguous velocities within the window are increasing. A shear segment continues to grow as the window slides until either the windowed signature is no longer increasing or the minimum velocity jump in the window is too large. During this shear growing process, an attempt is made to minimize the rejection of true features by allowing for spurious data values or outliers (typical of wind measurements) within these runs.

To reduce false detections, the completed segments are then pruned using additional tests. These tests impose requirements on segment smoothness, length, and the velocity difference across the segment. These test criteria were based on known microburst radial shear signature characteristics and have been validated with extensive testing. Parameters used in the initial segment identification and later segment filtering process are described in Appendix B to this report.

### 2. Shear Region Feature Identification

The second stage in the detection process attempts to group radial shear segments over azimuth into two-dimensional regions indicative of a divergent outflow.

The algorithm joins range-overlapping segments found on proximate radials to form two-dimensional shear regions. Variable factors in the joining process are the minimum overlap in range required and the maximum number of azimuths over which to associate two shear segments.

These regions are then post filtered using size and shear strength criteria. The

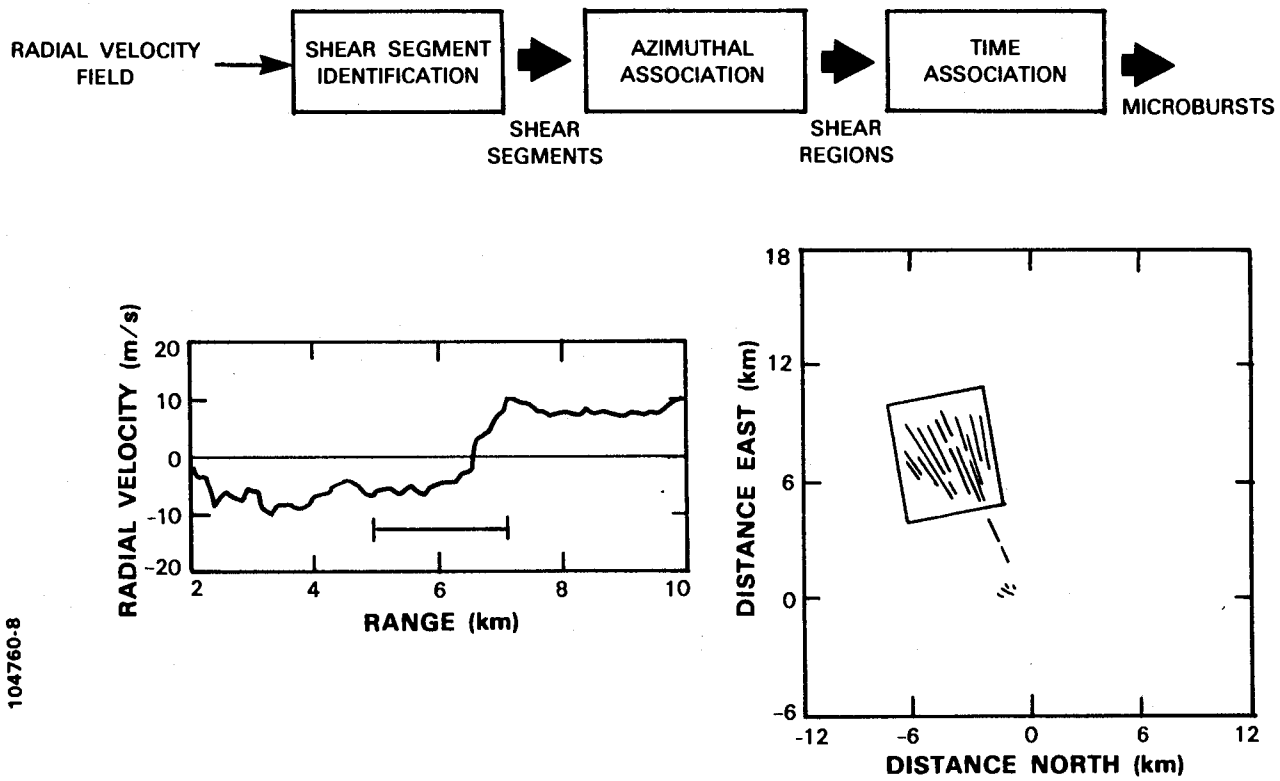


Figure V-1 Block diagram of feature extraction steps in the microburst divergent outflow algorithm.

shear intensity requirement is less than that posited in the definition of a microburst (10 m/s) to allow for detection of the outflow before it reaches an operationally significant strength.

The initial region creation and post filtering criteria are implemented using parameters described in Appendix B.

3. Microburst Feature Identification

The third phase of the detection process establishes the time continuity of regions on successive scans in order to substantiate a microburst. This relies on the assertion that microburst hazards are of significant duration. The continuity requirement would be especially valid in an operational ASR system where radial velocity field updates would be available at the radar's 4.8 second scan period.

Each region found on the latest scan is associated with those found on recent scans using a simple center-to-center Cartesian distance requirement. If the closest previous region is not already tagged as part of a microburst, and the current region is of sufficient strength, a new microburst is declared. If the closest previous region is already part of a microburst, the current region becomes part of this event. The parameters used at this stage of the algorithm are again defined in Appendix B.

The use of these hierarchical feature extraction techniques has provided a good basis to evaluate the ability to automatically detect wind shear with an ASR. Whether this type of algorithm is optimal is unknown, and other methods which operate directly on the two-dimensional wind field are being investigated. In this preliminary report, we will discuss only methods which build directly on the TDWR Microburst Divergent Outflow Algorithm [14] as they have been extensively tested and have met with reasonable success.

C. Adaptations for Use with ASR Velocity Fields

Table B-1 in Appendix B shows current algorithm parameter settings used for the ASR-generated velocity fields. Relative to the values used at Lincoln Laboratory for TDWR prototype testing, these criteria are somewhat less stringent to accommodate the ASR's tendency to see smaller and/or less intense regions of velocity shear owing to its elevation beam pattern. Examples of parameters that were relaxed are the shear segment differential velocity threshold and the shear region total area threshold. This latter parameter was reduced further when running off the high-pass filtered radial velocity field (Section IV-C-3) in an attempt to improve detection probabilities for the small shear signatures that sometimes resulted from this signal processing strategy.

As described in Section IV-C-1 and IV-C-2, two of the methods we tested detect shear regions from the mean low beam velocity field and then attempt to compensate for the beam-shape induced bias using either a static correction factor or one based on information from the corresponding shear feature in the high beam velocity field. As indicated in that section, the static correction factor often severely over- or underestimated the true shear owing to the large variability in the height of real microburst outflows.

Figure V.2 summarizes the more successful algorithm version which associates

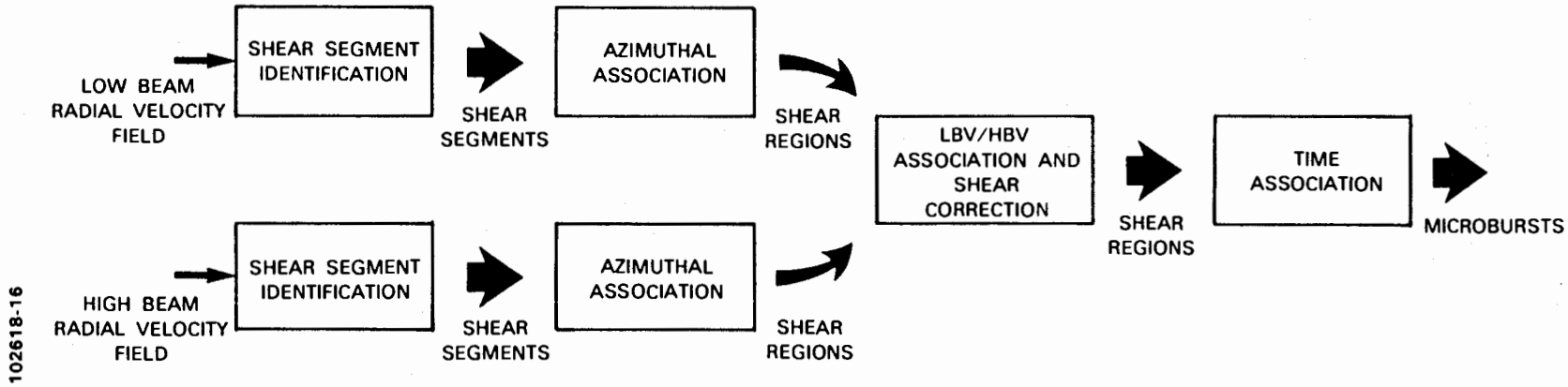


Figure V-2 Block diagram of feature extraction and shear correction steps in the ASR LBV/HBV microburst detection algorithm.

shear regions from the low and high receiving beams to estimate low altitude shear. Shear regions detected in the low beam velocity field are correlated with range-overlapping divergence regions found in the high beam velocity product. The shear for each region is taken to be its largest point-to-point velocity difference after median filtering of the single-gate radial velocity estimates. If an associated high beam shear is weaker than the low beam shear the phenomenon is considered to be a low altitude divergent outflow, and equation (4) from the previous section is used to correct the shear values associated with a region. The appropriate value for $\theta_0$, the elevation angle subtended by the outflow, is found by iteration using a bisection technique until the corrected estimates for the low and high beam converge. If there is no associated region in the high beam, an upper bound of 5 m/s (the site adaptation parameter *Threshold_Max_Diff* in Appendix B) is used for the calculation, establishing a lower bound for the corrected shear estimate.

# VI. EVALUATION OF MICROBURST MEASUREMENT AND DETECTION

This section employs data from the 1987 field experiment to illustrate the capability of an ASR to measure thunderstorm microbursts and to quantify the performance of the evaluated detection algorithm when running on the resulting velocity fields. In part A, we present case studies of microbursts occurring within 12 km of the radars. Simultaneous measurements from the pencil beam weather radar and the ASR are compared using images of the radial velocity fields and plots of velocity shear versus time during microbursts. Part B then presents global statistics on the detection and false alarm probabilities of the evaluated signal processing - hazard detection sequence.

Here, we will consider only the velocity shear estimation techniques described in IV-C-2 through IV-C-4. For brevity, the differential velocity estimates based on comparison of the shear measured in the mean low (LBV) and high beam (HBV) radial velocity fields will be denoted by "LBV/HBV". The radial velocity field estimated after filtering the signals with a $\pm 6$ m/s high pass filter will be designated by "LBHP" and that based on the differential low-high beam power spectral density difference by "DBV". We will not consider the static low beam mean velocity shear correction (IV-C-1) since the potential shear estimate errors have already been shown to be unacceptably large. In addition, we do not treat coherent high-low beam signal combination methods owing to lack of appropriate information on the antenna phase pattern.

## A. Case Studies

### 1. 21 May 1987 - 14:09 to 14:24

An intense, symmetric microburst occurred in an air-mass thunderstorm 10 km east of the radars on 21 May. Near-surface radial velocity shear of 28 m/s was measured by the pencil beam weather radar at the time of maximum intensity (14:15).

Figure VI-1 compares the radial velocity field measured by the pencil beam radar at 14:15 with simultaneous estimates based on the ASR signals. As in subsequent color images in this section, the upper left panel shows the field measured with the pencil beam radar scanning at a nominal $0.7^o$ elevation angle. The upper right panel shows the mean of the ASR's low beam power spectra (LBV); the adaptive filtering procedure described in reference [3] was used to remove ground clutter. The lower left plot is the LBHP velocity field while the image in the lower right shows the DBV field. For this scan, signals from the ASR testbed radar were processed only over the azimuth interval from $56^o$ to $260^o$. To eliminate the possibility of interfering with the ASR-7 at Huntsville's airport, the Klystron amplifier was not triggered as the antenna swept between $95^o$ and $110^o$. Later in the summer, this "blanked" sector was reduced in size and finally eliminated with permission from controllers at the airport.

The center of divergence at 9 km range/$85^o$ azimuth was clearly evident in the velocity fields estimated from the ASR data. Low velocity precipitation scatterers above the outflow account for the discrepancy between the pencil beam radar's differential velocity measurement and that seen in the LBV field from the ASR (28

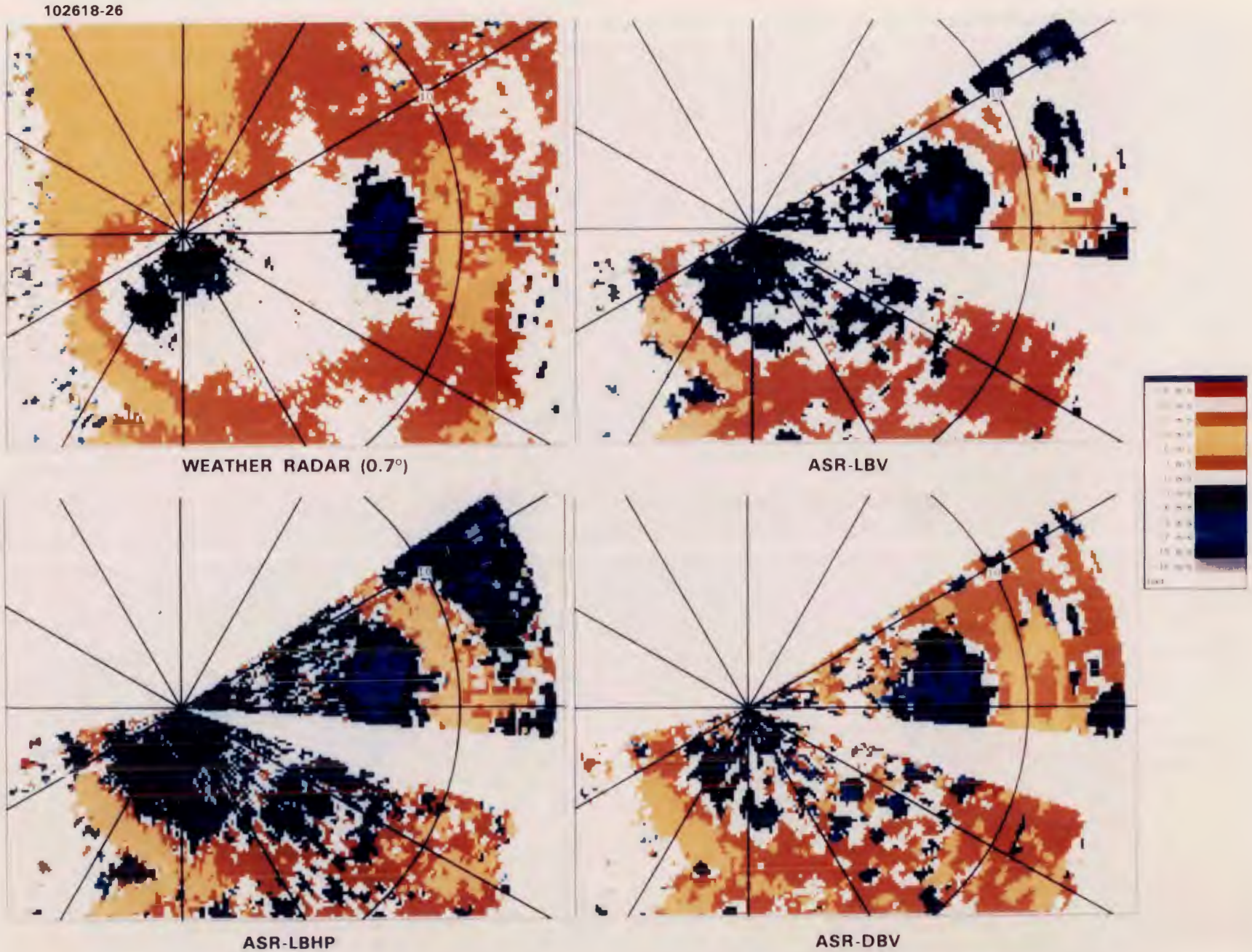


*Figure VI-1. Radial velocity fields from pencil beam weather radar and ASR during microburst at 14:15 (UT), 21 May 1987. Range ring is at 10 km.*

versus 24 m/s). The interfering spectral components were successfully filtered from the ASR signals using both the fixed high-pass transfer function (LBHP) and the comparison of the low-high beam power spectra (DBV). Thus the radial wind differential across the microburst is accurately depicted in the corresponding velocity fields at this time. The arc of weaker divergence extending from 4 km/180° to 3 km/240° was the remnant outflow from an earlier microburst.

Figure VI-2 compares the pencil-beam radar and ASR radial velocity shear measurements. Data collection on the ASR testbed radar ceased at 14:19. The values shown for the pencil beam radar were determined through manual examination of low-elevation angle PPI radial velocity fields whereas ASR estimates were from the microburst detection algorithm.

The MIT weather radar was performing volume scans during this event, resulting in only three surface PPI's over the time period shown; the microburst was first apparent in a scan at 14:09:30, had intensified significantly by the time of the next surface PPI at 14:15 and then weakened in the following scan at 14:24. Divergent velocity features were recognizable in the ASR-based LBHP and DBV velocity fields at 14:09 but were not of sufficient size and intensity to trigger a microburst report from the algorithm. An alarm was generated from the DBV field in the next ASR scan processed (14:10) and from the LBHP and LBV/HBV methods in the following scan (14:12). Prior to 14:16, the LBV/HBV shear estimate is higher than the other ASR estimates and the available pencil beam measurement. All three ASR-based measurements are consistent thereafter, but cannot be verified given the lack of surface scan data from the MIT weather radar.

2. 14 June 1987 - 19:15 to 19:40

This long-duration outflow exhibited three successive radial velocity shear maxima (Figure VI-3), corresponding to the surface impact of distinct downdrafts within a large thunderstorm cell. The center of divergence -- initially 10 km southeast of the radars -- drifted west-north westwards over the course of the event.

ASR-based shear estimates were in good quantitative agreement with the pencil beam measurements prior to the initial intensity peak at 19:18 and again after about 19:30. Between these times, the ASR differential velocity estimates averaged approximately 15% less than were measured by the weather radar. Over the duration of this outflow, the RMS differences between the ASR and pencil beam radar shear estimates were 5.2 m/s using the LBV/HBV estimation technique and were approximately 3.1 m/s with the LBHP and DBV products.

The radial velocity fields at 19:18 (Figure VI-4) all clearly showed the strong divergent signature at 10 km. Note that a second microburst (17 km/160°) -- centered beyond the range of critical operational need for wind measurements with an ASR -- is readily recognized in the DBV velocity field. A low reflectivity "ring" gust front passed over the site several minutes before this scan and is visible in the ASR-generated images as a thin, north-south oriented line of receding velocity 3 km west of the radars. The pencil beam radar was performing sector scans at this time so that only the southern portion of this arc was measured. Note finally the receding air motions present in the ASR fields at 15-25 km range, between the azimuths of 60° and 90°. The pencil beam radar did not receive sufficient returned energy from this region to make a velocity measurement. Since the sensitivities of the two radars are nearly equal at this range, we conclude that the

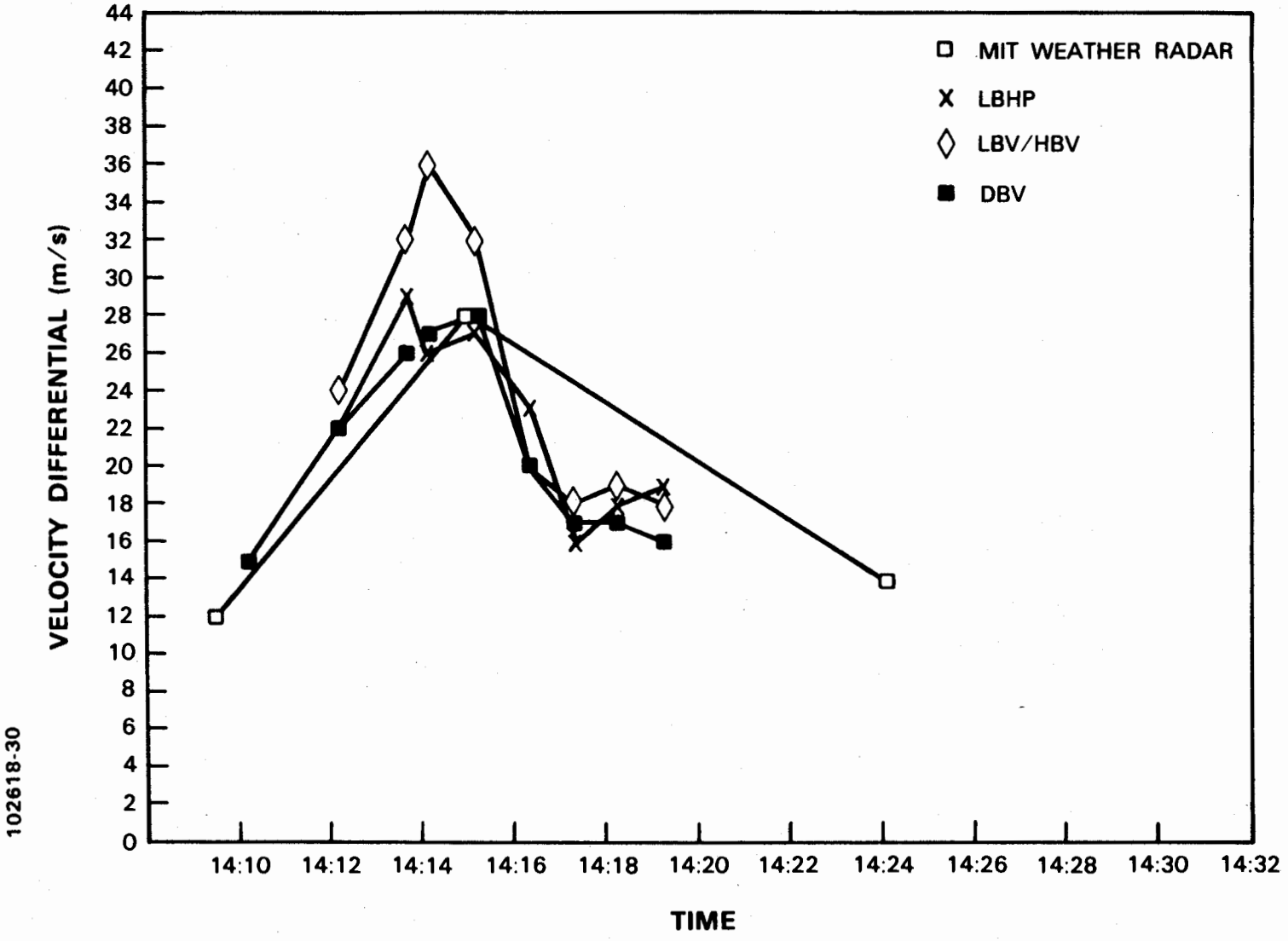


Figure VI-2 Pencil beam radar and ASR estimates of differential radial velocity versus time across microburst on 21 May 1987, 14:09 - 14:24 (UT).

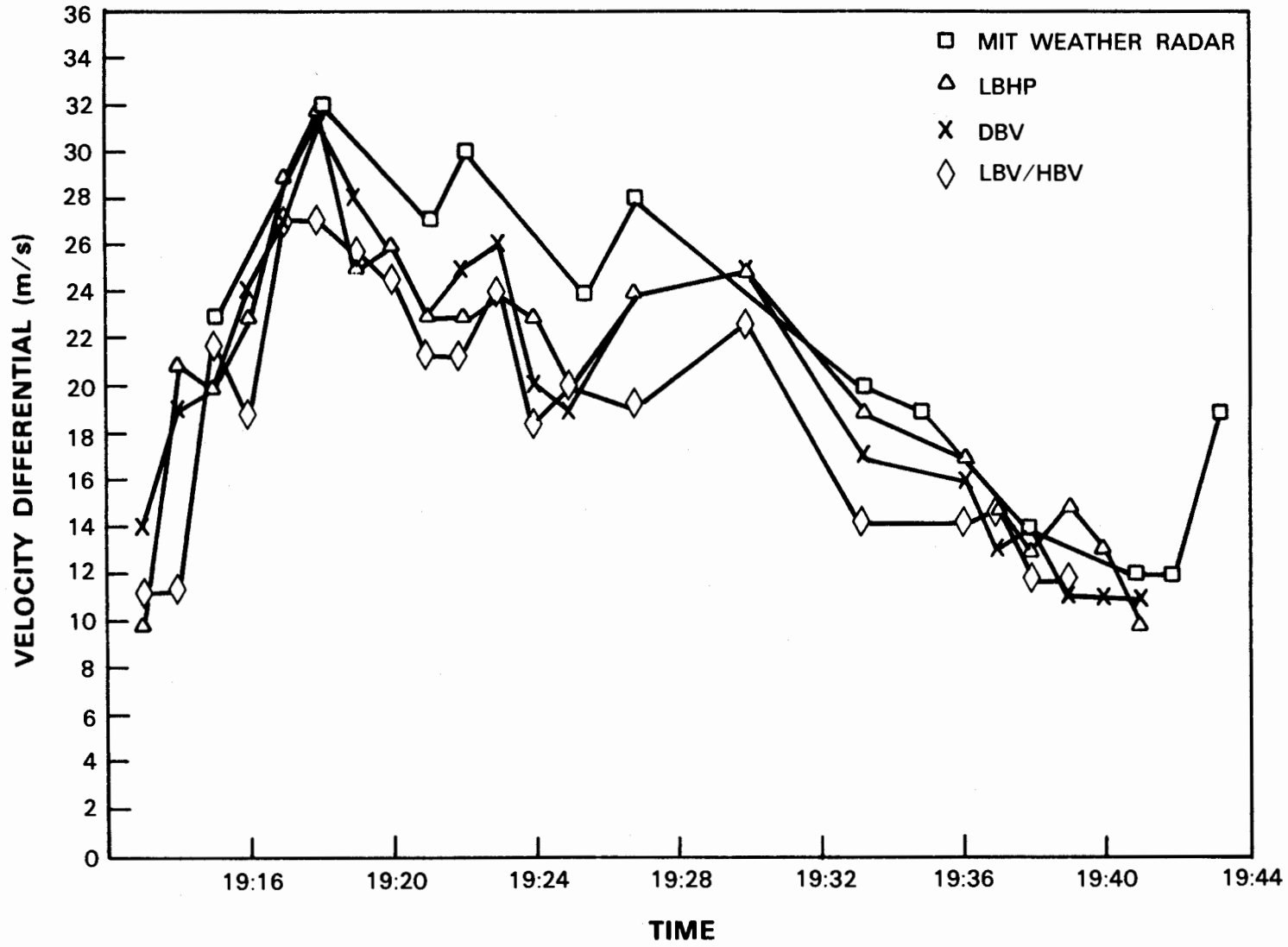


Figure VI-3 Pencil beam radar and ASR estimates of differential radial velocity versus time across microburst on 14 June 1987, 19:12 - 19:44 (UT).

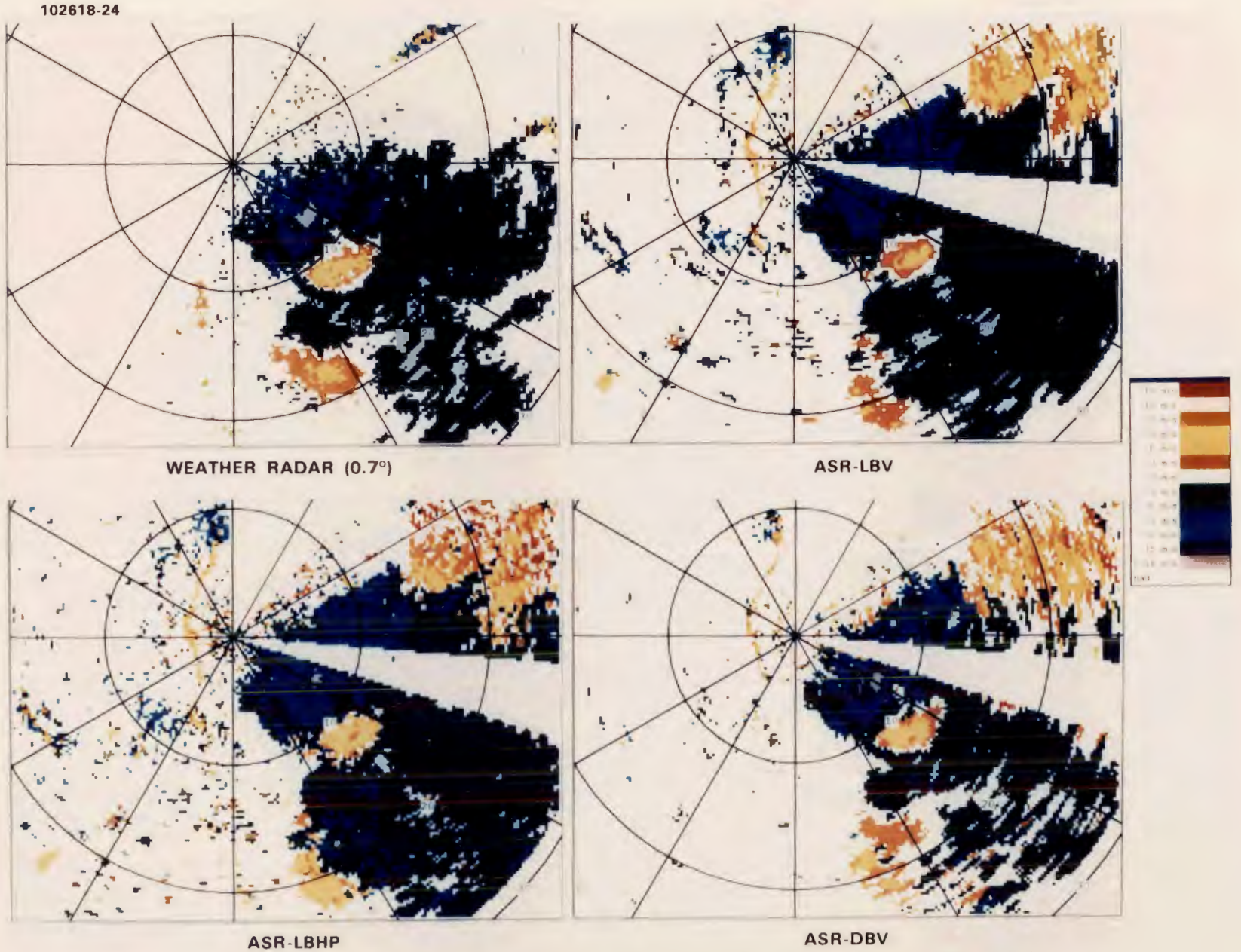


*Figure VI-4. Radial velocity fields from pencil beam weather radar and ASR during microburst at 19:18 (UT), 14 June 1987. Range rings are at 10 km intervals.*

scatterers producing the ASR signal were situated above the weather radar's beam and do not reflect surface velocity shear. Although the indicated divergence triggered microburst alarms on some of the ASR scans, these could probably have been eliminated by modifying the detection algorithm to require that reported wind shear regions overlap areas of significant radar reflectivity. The reflectivity factor measured by the ASR in the regions of receding velocity was 20 dBz or less.

3. 21 June 1987 - 20:35 to 21:00

This microburst formed as one cell of a loosely organized squall line passed over the site from southwest to northeast. The pencil beam weather radar was inoperative between 19:55 and 20:36, by which time a vigorous outflow was already in progress west-southwest of the site.

Figure VI-5 shows the radial velocity fields measured by the radars at 20:40. The ASR's LBV velocity estimate was heavily biased by overhanging precipitation. The approaching velocity core is significantly weaker than measured with the pencil beam radar and the receding portion of the outflow is evident only as a region of near-zero radial velocity at 8 to 10 km range. The high pass filtered (LBHP) velocity field showed strong receding winds only over a very small area at 10 km range. This occurred because the overhanging precipitation -- moving northeasterly at the storm translation velocity -- was outside of the filter stop bands and in most places of greater scattering cross section than the receding outflow winds. The DBV product correlates much more closely with the weather radar measurements in accurately depicting the spatial dimensions of the microburst outflow.

By 20:46, the center of divergence had migrated to 4 km/310° (Figure VI-6). At this azimuth, the mean motion of precipitation above the outflow was at right angles to radials from the radars. As a result, the associated bias over the receding velocity core was smaller when the ASR mean velocity estimator was used. The high pass filter stop bands were now matched to the overhanging precipitation spectrum so that LBHP produced a much better representation of the microburst wind field than earlier. The DBV radial velocity field again clearly showed the divergence.

Time histories of the estimated shear are plotted in Figure VI-7. The microburst algorithm declared a hazard beginning at 20:36 using the DBV and LBV/HBV techniques. This signature was not automatically detected in the high-pass filtered LBHP field until after 20:40, owing to the small area of the divergent signature (see Figure VI-5). Over the time period shown, RMS differences between the ASR and pencil beam radar shear estimates were 5.7 m/s using the LBV/HBV estimation technique, 5.4 m/s with the LBHP velocity product and 2.5 m/s with the DBV product.

4. 1 August 1987 - 20:30 to 20:50

An air-mass thunderstorm northwest of the site initiated a weak to moderate intensity microburst; pencil beam weather radar recording began at 20:32. Figure VI-8 compares the ASR and pencil-beam radar radial velocity fields at 20:34 at which time the latter radar measured a velocity differential of 17 m/s across the event. As in one of the preceding examples, the more distant, receding outflow is depicted as having near zero velocity in the LBV field owing to spectral broadening from precipitation aloft. The LBHP field shows the receding winds only over

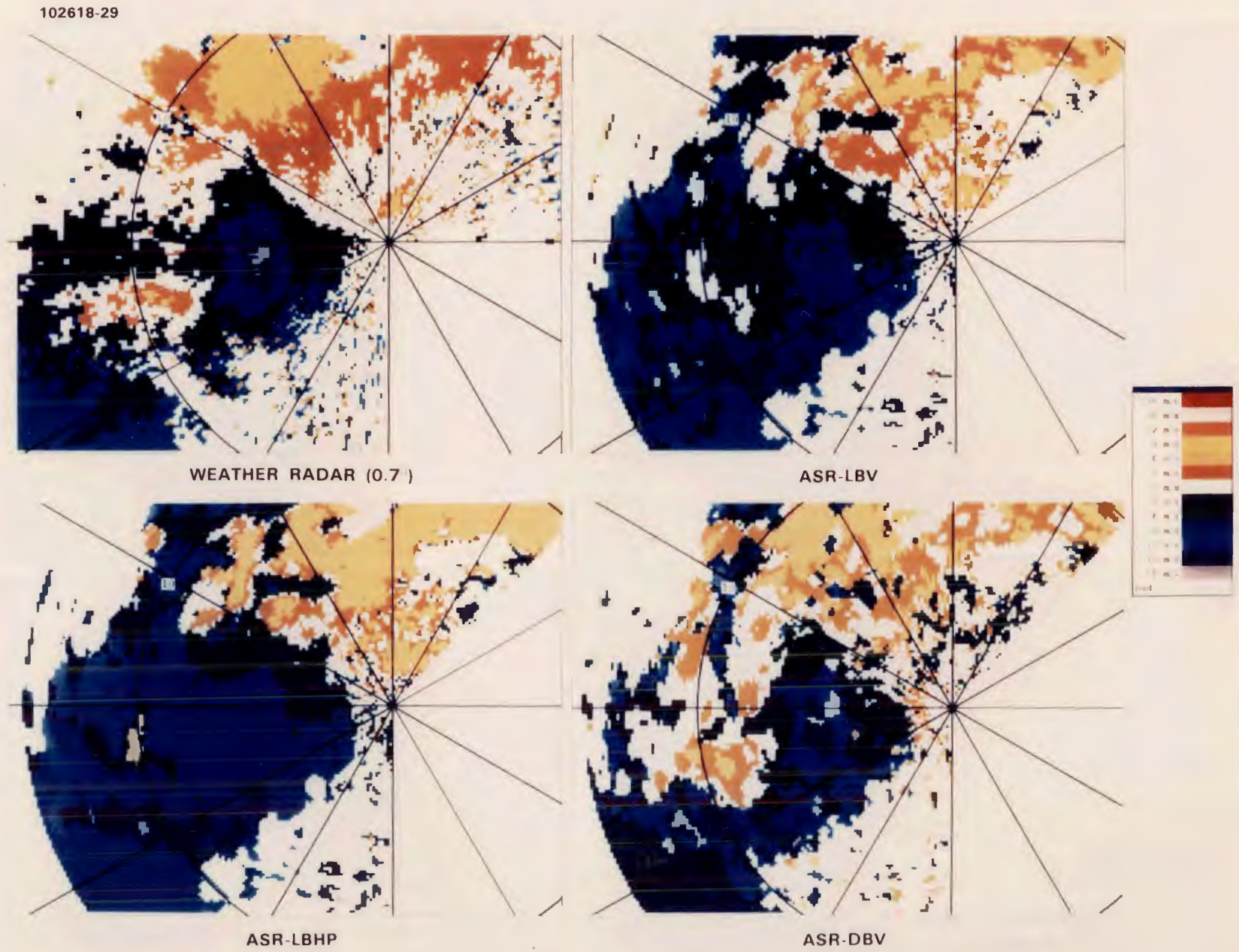


*Figure VI-5. Radial velocity fields from pencil beam weather radar and ASR during microburst at 20:40 (UT), 21 June 1987. Range ring is at 10 km.*

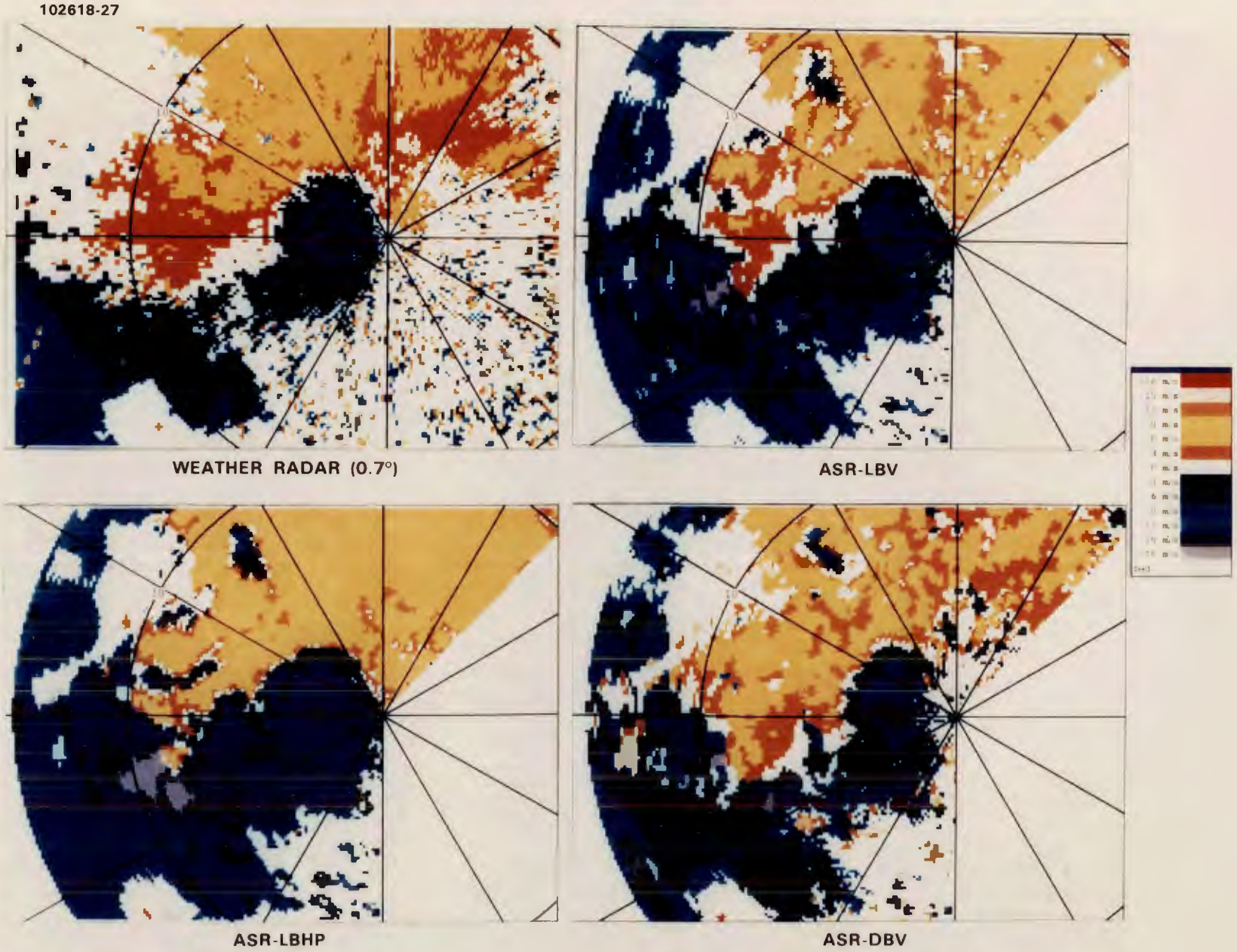


*Figure VI-6. Radial velocity fields from pencil beam weather radar and ASR during microburst at 20:46 (UT), 21 June 1987. Range ring is at 10 km.*

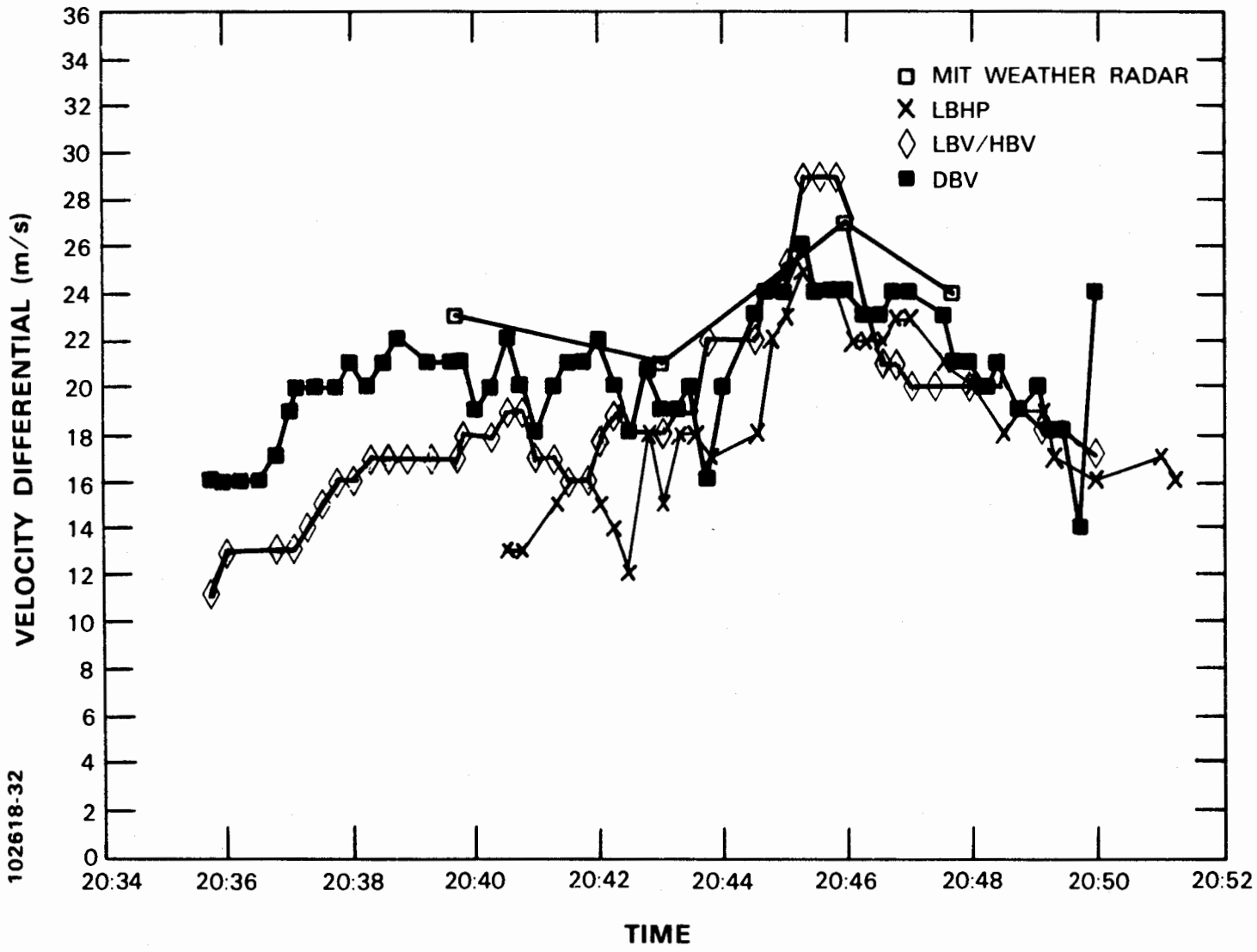


Figure VI-7 Pencil beam radar and ASR estimates of differential radial velocity versus time across microburst on 21 June 1987, 20:34 - 20:52 (UT).

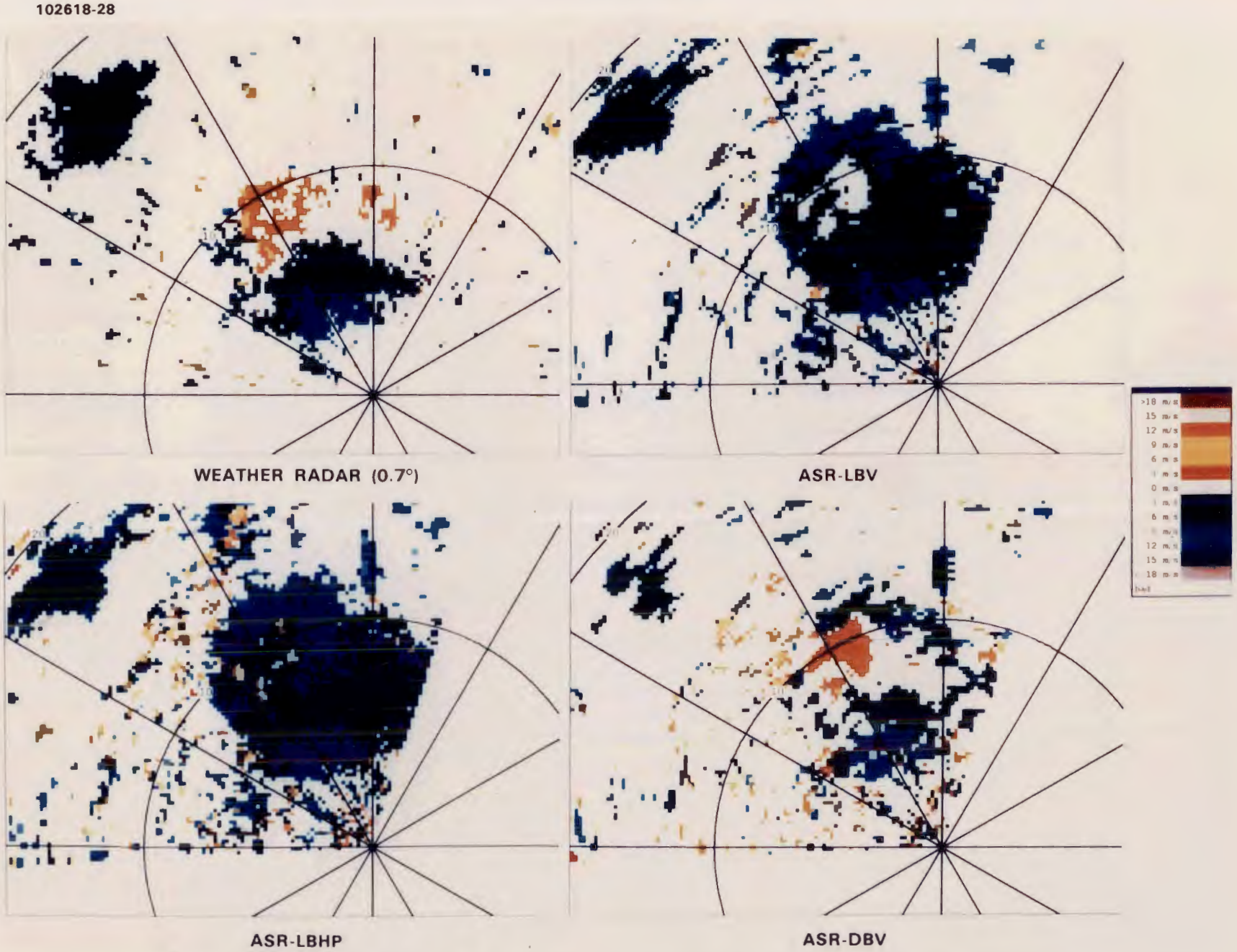


*Figure VI-8. Radial velocity fields from pencil beam weather radar and ASR during microburst at 20:34 (UT), 1 August 1987. Range rings are at 10 km intervals.*

very small areas; elsewhere the estimated radial velocity is everywhere towards the radar. The outflow was more clearly defined in the DBV field where a large area of receding outflow was measured at 8-10 km range.

5. 10 September 1987 - 22:26 to 23:05

At about 22:00 (UT) a thunderstorm cell formed 15 km southwest of the radars ahead of a cluster of large storms moving towards the site from the west. The pencil beam radar measured a weak outflow ($\Delta V_R = 4$ m/s) from this cell beginning at 22:27. By 22:36, the outflow had reached microburst intensity and had drifted northeasterly to within 10 km of the site.

Figure VI-9 compares pencil-beam measurements of the time history of the radial velocity difference in the microburst to ASR estimates based on the three methods described above. Prior to 22:39, the weak outflow was evident in the ASR-generated velocity fields only using the differential low-high beam power spectral technique (DBV): the resulting signature allowed for intermittent detection with the microburst detection algorithm. The outflow became apparent in the other ASR-based fields at about the time that the shear measured with the pencil beam radar exceeded 15 m/s. The algorithm declared a microburst at 22:39 using the LBV/HBV method and at 22:47 when operating from the LBHP field. The poor algorithm detection performance on this event resulted because the area of the radial shear region as seen by the ASR was small on many scans (particularly in the LBHP field) and did not pass the area threshold. On scans where detections were made, RMS differences from the pencil beam radar velocity shear estimates over the time period plotted were 3.0, 1.8 and 7.9 m/s respectively for the DBV, LBHP and LBV/HBV shear estimates.

Figure VI-10 compares the radial velocity fields measured at 22:47. At this time, the center of strongest divergence in the microburst was at 4 km range, 165° azimuth with velocity shear of 23 m/s over a distance of 2 km. The divergent signature is readily recognized in each of the fields estimated from the ASR data. New surface outflows centered at 4 km/65° and 7 km/70° were evident in the pencil beam data but did not yet give rise to signatures in the ASR data of sufficient clarity to be automatically detected by the microburst algorithm. These outflows had merged to form a single microburst in the following pencil beam PPI scan (22:50); by this time the divergence produced a detectable signature in the ASR-generated velocity fields. A gust front propagating ahead of a larger storm to the southwest produced the convergent radial velocity shear at 5 km range that extends in an arc from 210° to 270°.

6. 11 September 1987 - 23:40 to 00:00

A system of large, southwest to northeast oriented line storms formed in the afternoon of 11 September. By 23:00, the southeastern edge of one such storm's 30 dBz contour was directly over the radar site; the storm's echo extended 30 km in both the southwest and northeast directions. A microburst outflow began 5 km west of the site at 23:40 and intensified as its divergence center migrated north-eastwards.

Figure VI-11 plots time histories of the radial velocity differential in the microburst. The ASR-based estimates clearly show the overall rise and decay of outflow wind intensity. RMS differences from the pencil beam shear

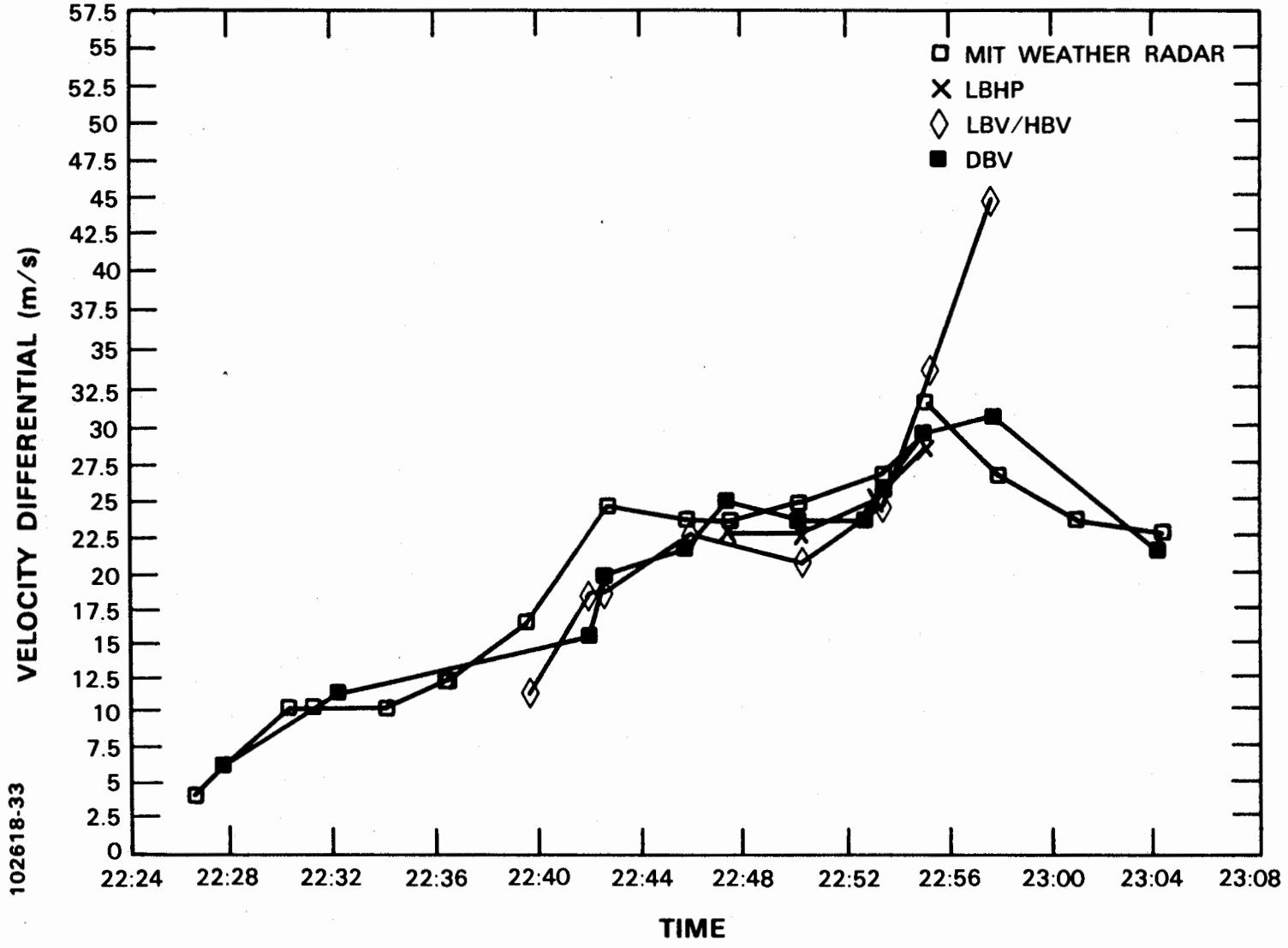


Figure VI-9 Pencil beam radar and ASR estimates of differential radial velocity versus time across microburst on 10 September 1987, 22:26 - 23:05 (UT).

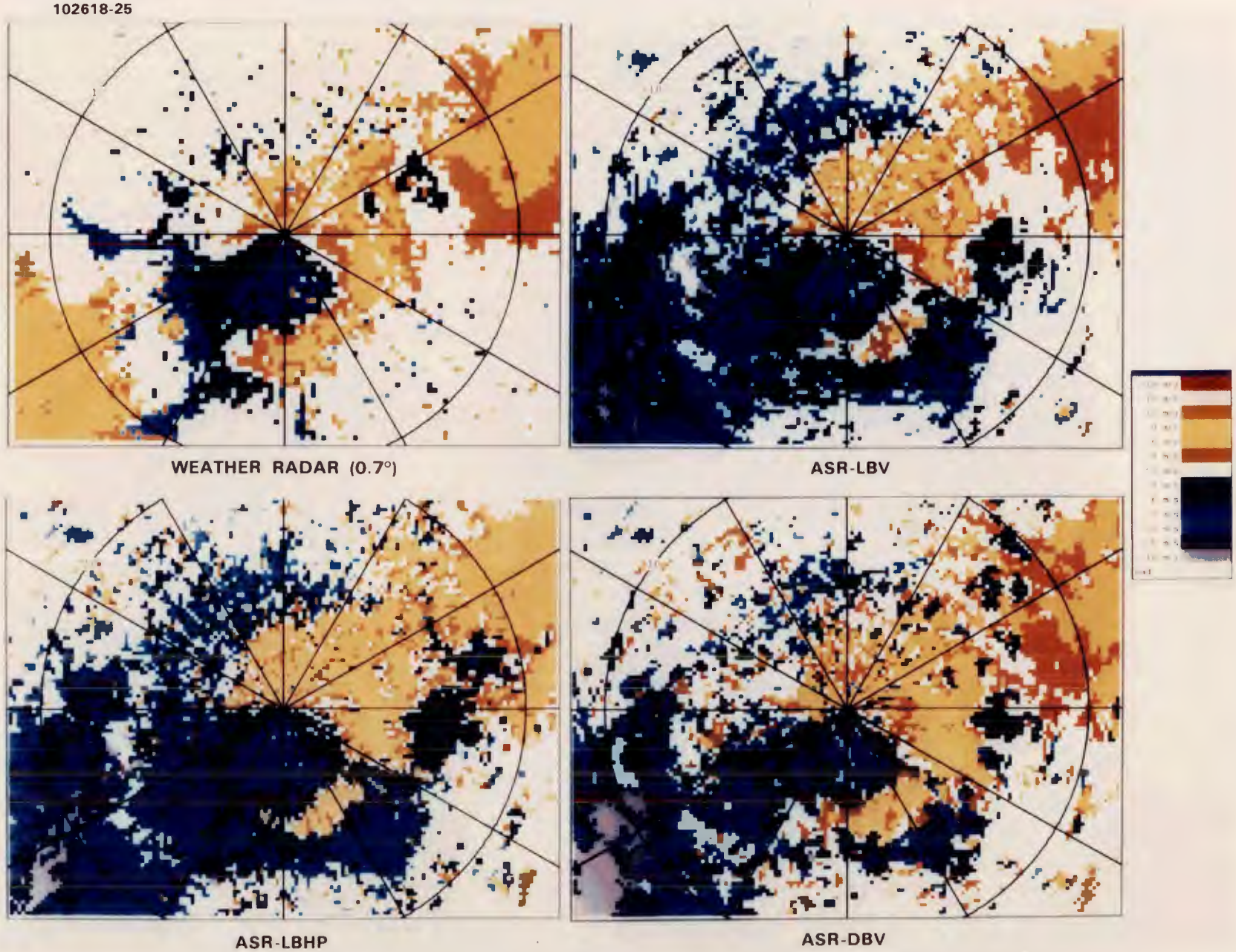


*Figure VI-10. Radial velocity fields from pencil beam weather radar and ASR during microburst at 22:47 (UT), 10 September 1987. Range ring is at 10 km.*

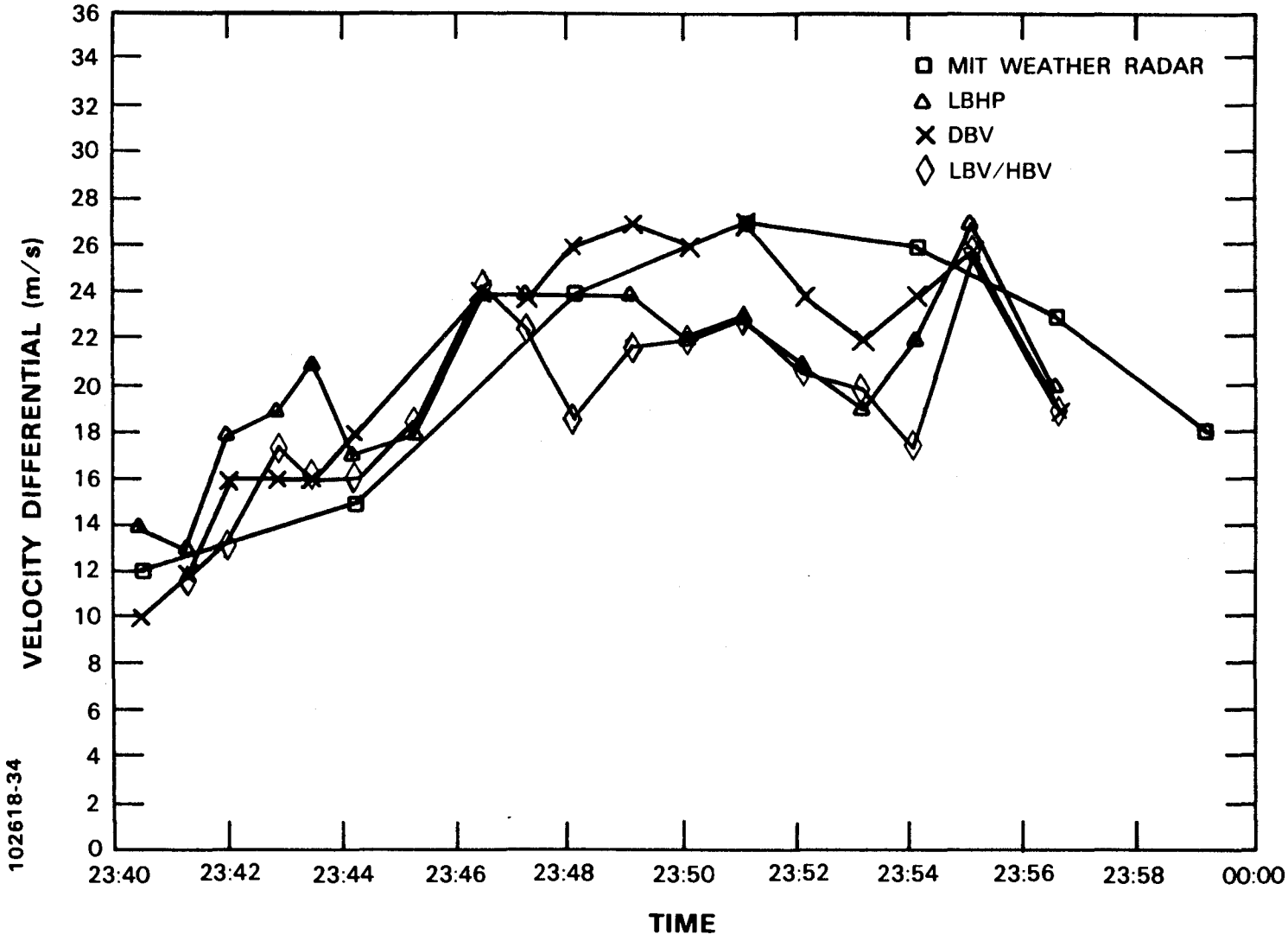


Figure VI-11 Pencil beam radar and ASR estimates of differential radial velocity versus time across microburst on 11 September 1987, 23:40 - 00:00 (UT).

measurements were 2.5, 4.0 and 4.1 m/s for the DBV, LBHP and LBV/HBV estimates respectively.

Images of the radial velocity fields at the time of maximum radial wind shear are shown in Figure VI-12. At this time the divergence center was at 4 km/315°. The shear signature is recognizable in each of the ASR-generated velocity fields; the DBV field in the lower right correlates more closely with the pencil beam measurements in showing the strongest receding outflow at 315°. The arc of strong radial velocity convergence at 10 km/300° – 345° is the leading edge of a large-scale outflow from a second line storm situated northwest of the radars.

## B. Overall Statistics on Microburst Detection Algorithm Performance

The above examples indicate that the quality of wind shear signatures in velocity fields estimated from the ASR data and the associated performance of the microburst detection algorithm varied among individual events. This section quantifies that variability by presenting a preliminary statistical measure of the performance of the evaluated processing sequence. For the days listed in Table III-1, we present merged probabilities of detection, false alarm and statistics on the accuracy of shear strength estimates for each of the three data processing strategies considered above. This evaluation included 30 separate microbursts, centered at ranges varying from 1 km to 20 km. Approximately 350 scans from the ASR testbed were processed and scored for these events, using the rules described below.

### 1. Scoring Rules

The algorithm performance was quantified using a procedure similar to that developed by the TDWR groups at Lincoln Laboratory and the National Center for Atmospheric Research (NCAR). Reflectivity and radial velocity images from the pencil beam weather radar were examined by a skilled observer on a scan-by-scan basis to determine the existence of a microburst, its range/azimuth center, the spatial extent of the outflow region (defined by a bounding "box" in range, azimuth space) and the radial velocity difference across the outflow. These "truth objects" were grouped together into "microburst events" (i.e. a sequence of pencil beam radar scans of the same microburst) and entered into a computer data base.

Since the times of processed data from the ASR testbed were often not coincident with a low elevation angle PPI scan from the weather radar, it was necessary to map these truth objects into a second data base with times matched to the processed ASR data. For times between the first and last pencil beam radar scan in a microburst event, this mapping was accomplished by linearly interpolating the microburst center, range/azimuth extent, and shear metric from the two "truth objects" closest in time to the desired point. ASR-based microburst declarations that fell slightly before or slightly after the temporal limits of a microburst event were classified as "early" or "late" as described below.

"Microburst alarms" (i.e. range/azimuth regions where the microburst detection algorithm found velocity shear satisfying the criteria described in Section V) were then scored against this data base on a scan-by-scan basis. The specific scoring rules were as follows.

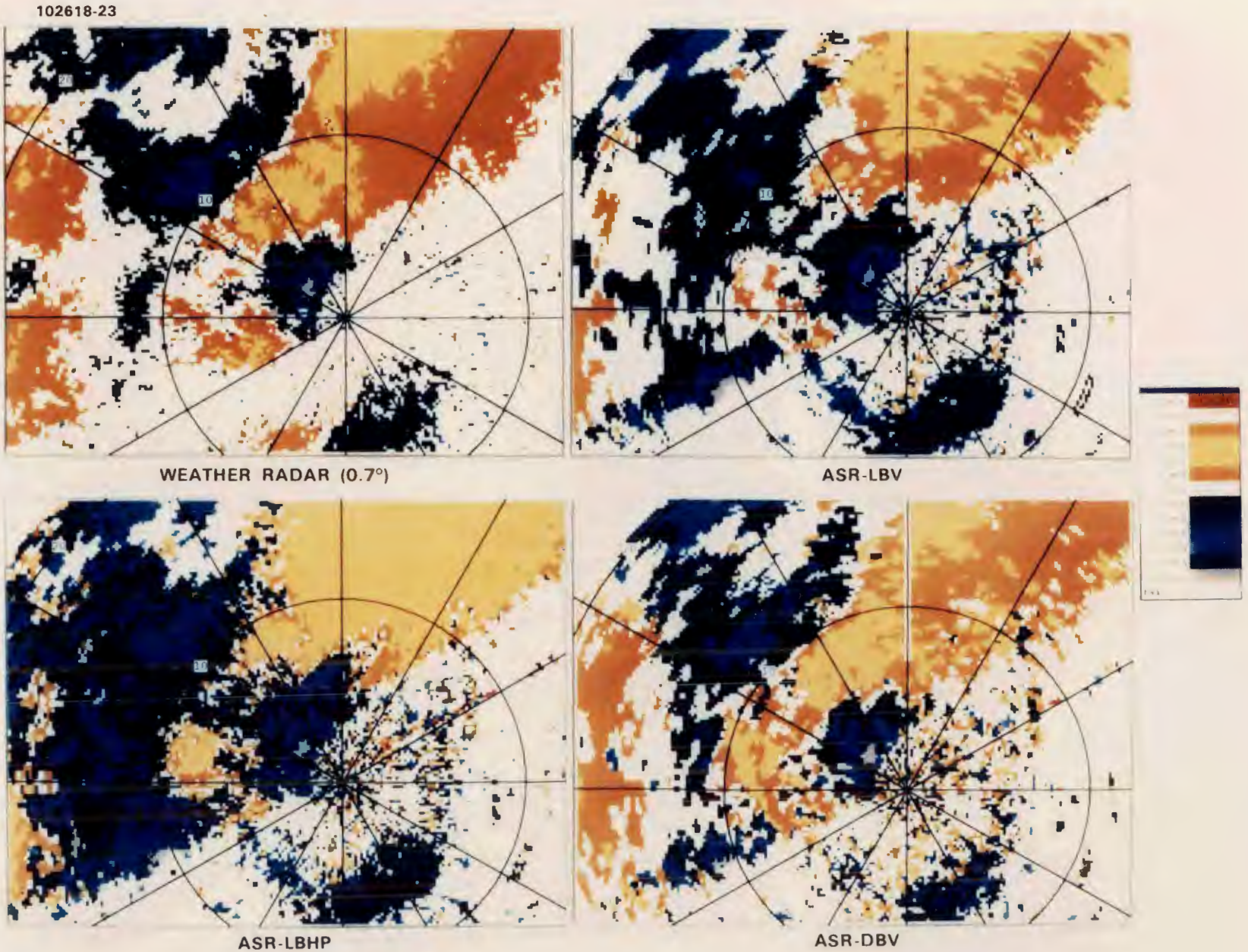


*Figure VI-12. Radial velocity fields from pencil beam weather radar and ASR during microburst at 23:51 (UT), 11 September 1987. Range rings are at 10 km intervals.*

(i) If the minimum distance between the alarm outline and truth outline is less than 2 km, mark them as a detection.

(ii) More than one alarm may coincide with a truth, but the truth is considered to be detected just once.

(iii) If within the next minute a truth occurs within 2 km of an alarm, the alarm is scored as "early".

(iv) If in the past minute a truth was present within 2 km of an alarm, the alarm is scored as "late".

The quantities calculated from the scoring procedure are:

(i) probability of detection (POD), the ratio of the number of detected microbursts to the number of microbursts in the truth set;

(ii) probability of a false alarm (PFA), the ratio of alarms not associated with a microburst to the total number of alarms;

(iii) shear ratio (SR), the mean of the ratio of detected shear to true shear. This quantity measures the bias in the ASR shear estimates relative to pencil beam radar "truth" and was averaged for all microburst detections within each range/shear strength category;

(iv) root mean squared (RMS) relative error between the ASR estimates and the pencil beam measurements, a measure of the consistency of the shear strength reports from the microburst detection algorithm.

"Early" and "late" declarations are not included in either a negative or positive sense in the statistics, but allow for an event's history to be understood more easily. Because of the scan update rate differences between the weather radar and the ASR testbed this is perhaps the most objective way to treat an event for which truth is not available over its duration.

2. Results

(a) LBV/HBV Method

Table VI-1 summarizes algorithm performance when detections were made from the mean low beam velocity field and the radial velocity shear estimates were based on comparison of measured shear in the low and high beam fields (the LBV/HBV method). The detection probability for all microbursts with velocity shear greater than 10 m/s and range centroids inside 12 km was 0.79. The corresponding false alarm probability was 0.08. When microbursts out to 16 km range were included, the detection and false alarm probabilities were 0.80 and 0.12.

As seen from the table, the calculated performance metrics generally improve for more intense microbursts (i.e. greater radial velocity shear). Figure VI-13 plots detection and false alarm probabilities, and average shear ratio as a function of the minimum velocity shear of the truth objects or algorithm alarms that were scored. Only events inside the operationally critical region within 12 km of the radar were included in this calculation. The plot indicates that for microbursts exhibiting a differential velocity of 15 m/s or greater, the detection probability was 0.90. Microburst alarms indicating a velocity shear greater than 15 m/s were false 6 percent of the time. If the minimum shear category considered were increased to 20 m/s, the corresponding POD and PFA values are 0.95 and 0.05.

The average ratio of velocity shear estimated from the LBV/HBV technique to

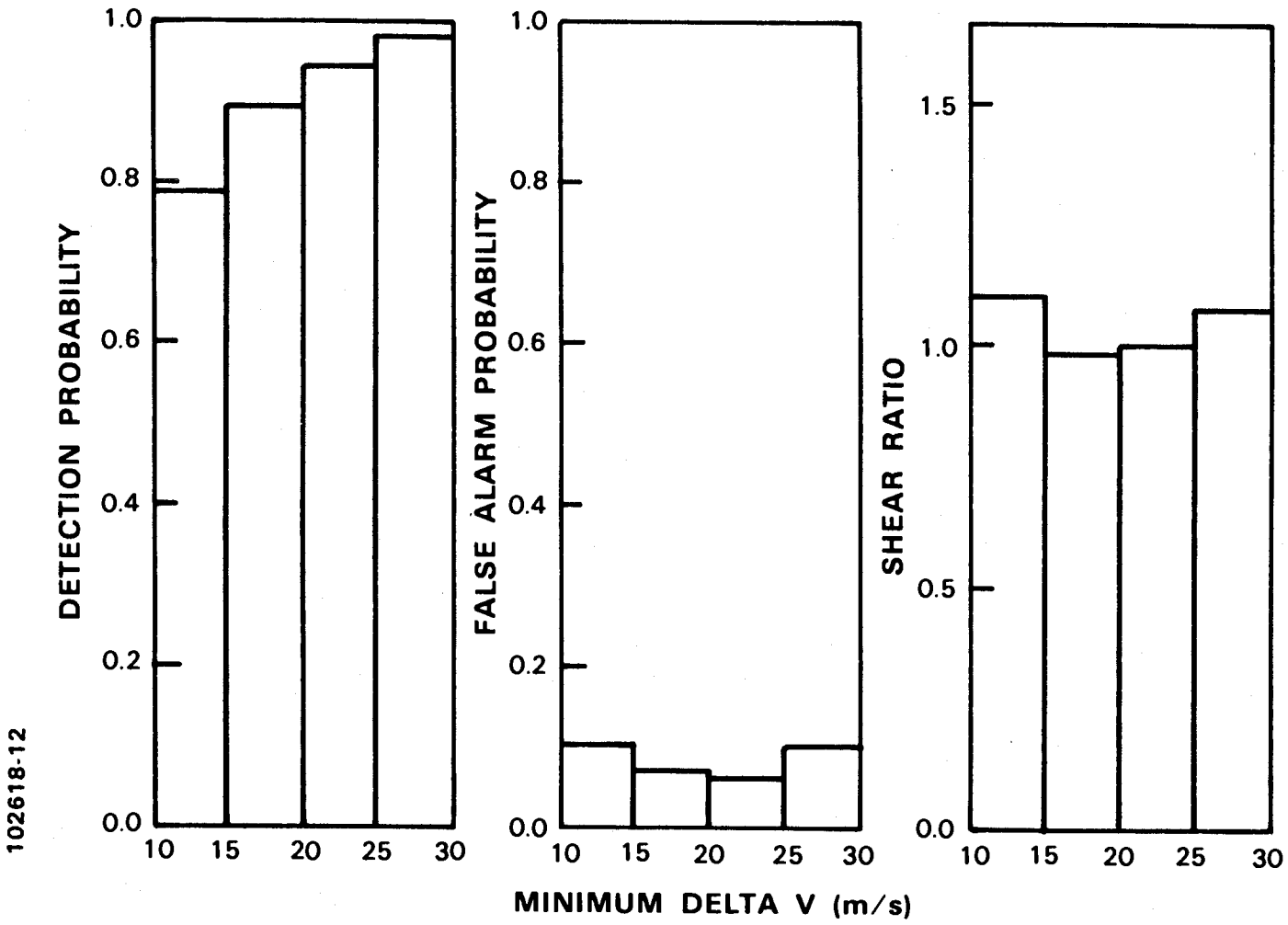


Figure VI-13 Probability of detection (POD), probability of false alarm (PFA) and shear ratio (SR) using the LBV/HBV processing strategy for the ASR signals. The histograms reflect the cumulative statistics for all microburst events (POD, SR) or alarms (PFA) exhibiting velocity shear larger than the minimum abscissa value for each shear category.

| Table VI-1: LBV/HBV Performance Statistics by $\Delta V_R$ (m/s) | | | | | |
|---|---|---|---|---|---|
| *Range Centers* < 12 km | | | | | |
| | 10-14 | 15-19 | 20-24 | >=25 | OVERALL |
| POD | 38/ 79 | 68/ 82 | 80/ 85 | 41/ 42 | 227/288 = 0.79 |
| PFA | 19/157 | 14/190 | 0/ 75 | 8/ 74 | 41/496 = 0.08 |
| SR | 1.76 | 0.94 | 0.95 | 1.15 | 1.12 |
| RMS | 0.75 | 0.26 | 0.27 | 0.36 | 0.37 |
| *Range Centers* < 16 km | | | | | |
| | 10-14 | 15-19 | 20-24 | >=25 | OVERALL |
| POD | 56/100 | 86/105 | 98/103 | 41/ 42 | 281/350 = 0.80 |
| PFA | 35/194 | 18/222 | 2/ 85 | 16/ 98 | 71/599 = 0.12 |
| SR | 1.65 | 0.95 | 0.97 | 1.15 | 1.13 |
| RMS | 0.75 | 0.30 | 0.28 | 0.36 | 0.37 |

that measured by the pencil beam radar was within fifteen percent of unity for microbursts events with differential velocities stronger than 15 m/s. The LBV/HBV shear reports for weaker microbursts exhibited a strong bias towards overestimation of the shear strength. As illustrated in some of the case studies in Section VI-A, the variance of the corrected shear estimates was sometimes large, even for events in the more intense shear categories. The overall RMS relative difference with respect to the pencil beam measurements was 0.37 for all microbursts inside 12 km, dropping to 0.30 if only events with shear greater than 15 m/s were considered. Temporal smoothing of the shear estimates would be feasible if every scan of the ASR data were processed; this might reduce the "noisiness" of the LBV/HBV shear estimates to an acceptable level.

(b) LBHP Method

In discussing the case studies of Section VI-A, we pointed out that microburst signatures as depicted in the high-pass filtered radial velocity field (LBHP) were sometimes small in area. In addition, because the filter normally drives the velocity estimate to one side or the other of its stop band, the indicated transition from approaching to receding velocities across the divergence center was often extremely sharp. The microburst detection algorithm evaluated here is unsuited to identifying large shear regions around such transitions since its segment growth process requires monotonically increasing runs of radial velocity.

We attempted to adapt the detection algorithm to the above characteristics. The threshold determining minimum microburst area was reduced and a five point Gaussian filter along the range axis was used to smooth the transitions between approaching and receding radial velocity regions in microbursts. However, there were still many cases where the algorithm failed to report a microburst in spite of a readily apparent velocity couplet in the LBHP field. As shown in Table VI-2 and Figure VI-14, the overall detection probability for microbursts inside 12 km was only 0.82 when running off the LBHP field, even when scoring was restricted to events with velocity differentials greater than 20 m/s.

To confirm that this poor performance resulted at least partially from the inability of the detection algorithm to find sufficiently large regions of monotonically increasing radial velocity, we visually examined the same LBHP fields used in scoring the algorithm. A revised probability of detection was estimated based on

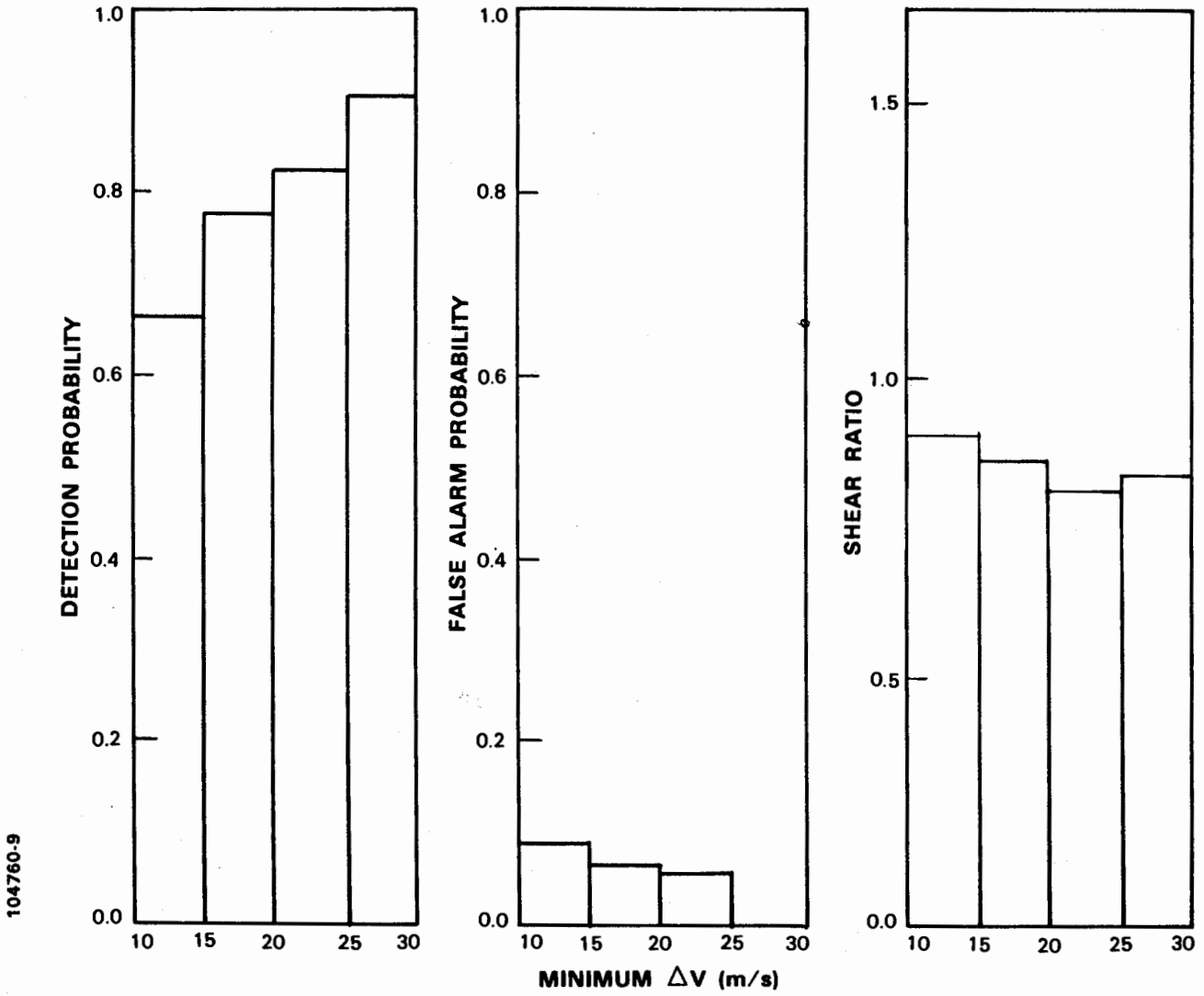


Figure VI-14 Probability of detection (POD), probability of false alarm (PFA) and shear ratio (SR) using the LBHP processing strategy for the ASR signals. The histograms reflect the cumulative statistics for all microburst events (POD, SR) or alarms (PFA) exhibiting velocity shear larger than the minimum abscissa value for each shear category.

| Table VI-2: LBHP Performance Statistics by $\Delta V_R$ (m/s) | | | | | |
|---|---|---|---|---|---|
| *Range Centers* < 12 km | | | | | |
| | 10-14 | 15-19 | 20-24 | >=25 | OVERALL |
| POD | 28/ 76 | 52/ 75 | 65/ 83 | 38/ 42 | 183/276 = 0.66 |
| FAR | 22/181 | 11/162 | 4/ 62 | 0/ 9 | 37/414 = 0.09 |
| SR | 1.16 | 0.96 | 0.80 | 0.83 | 0.91 |
| RMS | 0.20 | 0.13 | 0.27 | 0.25 | 0.23 |
| *Range Centers* < 16 km | | | | | |
| | 10-14 | 15-19 | 20-24 | >=25 | OVERALL |
| POD | 46/ 96 | 65/ 98 | 85/103 | 38/ 42 | 234/339 = 0.69 |
| FAR | 34/209 | 12/190 | 7/ 68 | 0/ 10 | 53/477 = 0.11 |
| SR | 1.14 | 0.98 | 0.84 | 0.83 | 0.94 |
| RMS | 0.18 | 0.14 | 0.27 | 0.25 | 0.23 |

the opinion of a human observer that a recognizable shear signature was present in the data. The resulting POD for microburst events inside 12 km and with $\Delta V_R$ greater than 20 m/s increased to 0.95.

We believe therefore that the low detection probability achieved with this method is a result of mismatch between the evaluated hazard detection algorithm and the characteristics of the LBHP radial velocity field. Anderson [18] is evaluating a different shear detection algorithm that appears to be less sensitive to distortions in the velocity field introduced by the high pass filter. His results will be reported separately.

3. DBV Method

Table IV-3 lists summary statistics for the microburst algorithm when the input radial velocity fields were estimated using information from the differential high and low beam power spectra. Microburst events centered within 12 km of the radar were detected with a probability of 0.92 and a corresponding false alarm probability of 0.04. If the maximum range of consideration was increased to 16 km, the POD and PFA were 0.92 and 0.09 respectively.

Figure VI-15 plots the algorithm performance metrics as a function of the minimum velocity shear of the truth objects and algorithm alarms considered. Again the statistics are limited to events centered within 12 km of the radars. For microbursts with differential velocity greater than 15 m/s, the POD was 0.96; algorithm reports indicating shear greater than 15 m/s were false only 1 percent of the time.

Reported velocity shear for all detected microburst events inside 12 km was, on average, 0.91 of the shear measured by the pencil beam weather radar. This tendency for the DBV shear estimate to be lower on average than simultaneous pencil beam measurements is probably due to the higher "effective" beam elevation angle associated with this ASR velocity estimation technique. We showed in section IV-C-4 that the DBV field corresponds to a tilt angle of $1.3^o$ (as opposed to $0.7^o$ for the pencil beam "truth") assuming linear variation in wind speed with height near the ground. The overall RMS relative difference from the pencil beam weather radar measurements was 0.24 for events inside 12 km.

| Table VI-3: DBV Performance Statistics by $\Delta V_R$ (m/s) | | | | | |
|---|---|---|---|---|---|
| *Range Centers* < 12 km | | | | | |
| | 10-14 | 15-19 | 20-24 | >=25 | OVERALL |
| POD | 60/ 76 | 77/ 85 | 86/ 86 | 42/ 42 | 265/289 = 0.92 |
| PFA | 15/164 | 2/157 | 0/101 | 2/ 27 | 19/449 = 0.04 |
| SR | 1.04 | 0.87 | 0.90 | 0.83 | 0.91 |
| RMS | 0.27 | 0.25 | 0.19 | 0.27 | 0.24 |
| *Range Centers* < 16 km | | | | | |
| | 10-14 | 15-19 | 20-24 | >=25 | OVERALL |
| POD | 77/ 96 | 100/109 | 106/106 | 42/ 42 | 325/353 = 0.92 |
| PFA | 39/240 | 7/188 | 1/105 | 3/ 28 | 50/561 = 0.09 |
| SR | 0.99 | 0.85 | 0.88 | 0.83 | 0.89 |
| RMS | 0.27 | 0.27 | 0.19 | 0.27 | 0.25 |

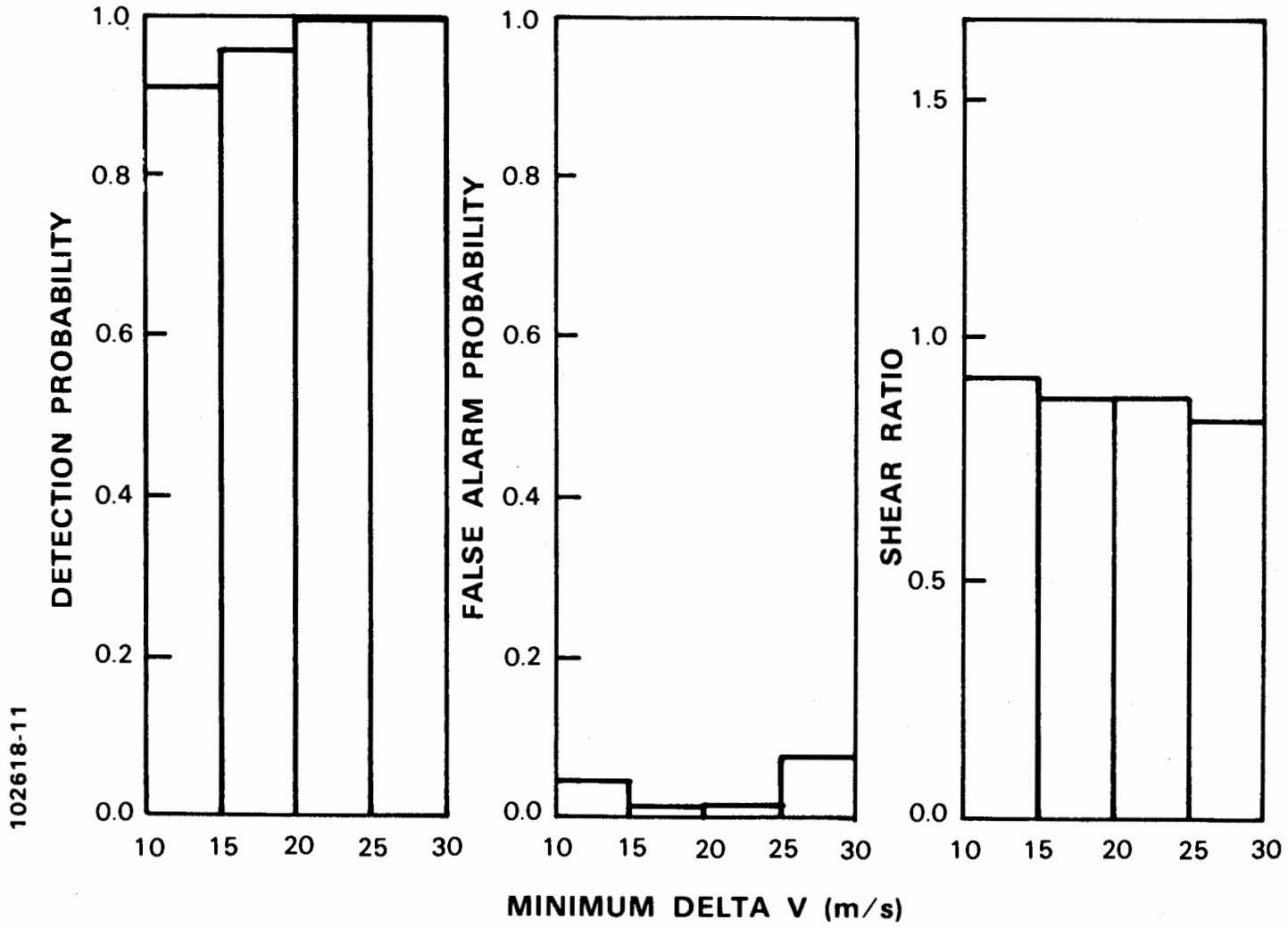


Figure VI-15 Probability of detection (POD), probability of false alarm (PFA) and shear ratio (SR) using the DBV processing strategy for the ASR signals. The histograms reflect the cumulative statistics for all microburst events (POD, SR) or alarms (PFA) exhibiting velocity shear larger than the minimum abscissa value for each shear category.

# VII. SUMMARY AND IMPLICATIONS FOR DEVELOPMENT OF AN OPERATIONAL MICROBURST DETECTION CAPABILITY

## A. Preliminary Statement of ASR Microburst Detection Capability

The above case studies and summary statistics allow for an initial statement of the capabilities and limitations of ASRs for automatically detecting microburst wind shear. Our analysis indicated that strong ($\Delta V > 15\ m/s$) microbursts within 12 km of the radars produced recognizable signatures in the ASR data; these in turn could be detected automatically by a modified version of the TDWR surface outflow detection algorithm at the level of confidence called for in the TDWR systems requirements statement. Best-case combined detection and false alarm probabilities (using the differential low-high beam power spectrum method (DBV)) were 0.96 and 0.01 for this class of events.

Our analysis of microbursts with differential velocities between 10 and 15 m/s or at ranges beyond 12 km was also favorable although POD and PFA statistics were somewhat less than the values given above. Signatures from weaker outflows -- for example, 10 September before 22:40 -- were sometimes ill-defined in the ASR-based velocity fields, resulting in missed or intermittent detections. The best-case (DBV) overall algorithm detection probability against microbursts inside 12 km but with low shear ($\Delta V_R \leq 15 m/s$) was 0.79 and the associated false alarm probability was 0.09. For microbursts centered between 12 and 16 km with $\Delta V_R \geq 15 m/s$, the corresponding statistics were 0.98 and 0.19.

Examination of the images in Figures VI-1,4,5,6,8,10 and 12 shows that in many cases, the velocity field estimate based on simultaneous use of the high and low beam power spectral estimates (DBV) correlated better with the pencil beam radar measurements than the fields that used only the low receiving beam signal. This correspondence refers to the size of the approaching or receding velocity regions (e.g. Figure VI-5) and/or the indicated position of the center of divergence (Figure VI-12). The increased fidelity of the radial velocity fields estimated using this method resulted in improved overall detection and false alarm statistics relative to the other techniques that were evaluated. As discussed in the following section, implementation of receiving paths to acquire data from both beams of an ASR-9 would not be difficult, although the required signal processing would be more computationally expensive.

Finally, we presented comparisons between pencil beam radar and ASR estimates of the accepted microburst intensity metric -- the total differential radial velocity across the outflow. Two statistics characterizing shear strength report accuracy were calculated: the "shear ratio" which measured the average bias in the ASR estimates, and the RMS relative deviation between the ASR and pencil beam measurements. The shear ratio calculation was favorable, indicating that over all events scored, the ASR microburst intensity estimates using the methods evaluated were biased by 15 percent or less with respect to the corresponding pencil beam measurements. For the significant category of microburst events (range center $\leq$ 12 km, $\Delta V_R \geq 15$ m/s) the overall RMS relative difference between the best-case DBV-based shear report and the pencil beam measurements was 0.23. Seventy-five percent of the DBV shear reports were within $\pm 25$ percent of the corresponding pencil beam radar measurement.

Discrepancies between the pencil beam radar and ASR-based velocity shear estimates may result from:

(i) statistical errors in the ASR estimates that could be removed, for example, by temporal smoothing of the data;

(ii) errors caused by linear interpolation of the weather radar measurements to the times of the ASR scans. Many of the plots of velocity shear versus time in Section VI-A show periods where the pencil beam radar's scanning schedule did not unambiguously define the evolution of outflow intensity;

(iii) inconsistency between the methods used by the human "truthers" to calculate $\Delta V_R$'s and the procedure implemented in the microburst detection algorithm. In particular, we observed that the humans sometimes computed $\Delta V_R$ between approaching and receding velocity maxima that were separated by 5 km or more in range and were not connected by a monotonically increasing velocity pattern. In this circumstance, the size of shear regions found by the microburst detection algorithm was smaller than declared by the human observer and the maximum velocity differential within the search area was less;

(iv) inadequacies in the assumptions used in deriving the ASR shear estimators. For example, compensating convergence above microbursts is sometimes strong; thus, neglect of this effect in deriving the LBV/HBV shear correction is clearly not always justified. We showed several examples where the radial velocity of precipitation above microburst outflows was greater in magnitude than the stop bands of the high pass filter used in generating the LBHP product. Thus this filter did not always effectively "unbias" the ASR velocity measurements and in some cases even resulted in a velocity estimate with sign opposite to that actually present in winds near the surface. As pointed out previously, the effective "tilt angle" using the DBV method ($1.3^{\circ}$) is higher than would be desirable for measurements of surface outflows, particular at ranges beyond 10 km.

The first three factors above are caused by shortcomings in the data collection and analysis for this preliminary evaluation and do not represent fundamental limitations for accurately measuring wind shear. Ongoing work will:

(i) refine the algorithm and scoring procedures to reduce inconsistencies in the rules used to quantify microburst intensity;

(ii) acquire additional data with more timely near-surface scanning from the weather radar to reduce the need for temporal interpolation;

(iii) analyze the vertical structure of winds and reflectivity in and above microbursts (measured with RHI scans) to determine explicitly how these affect the ASR's shear estimates.

We expect that by additional smoothing of the ASR velocity data, refinement of signal processing and hazard algorithm logic and more careful evaluation of the weather radar's "truth", one could achieve better quantitative accuracy in ASR shear reports than was obtained in this initial analysis.

B. Implementation Issues

1. Radar Modifications

Our testbed airport surveillance radar was designed to permit the collection of signals in modes that would not be supported by an operational ASR-8 or ASR-9. Capabilities such as access to low beam data at short range, the ability to utilize a sensitivity time control (STC) function that would not obscure low reflectivity wind shear events and the simultaneous availability of low and high beam signals would require the insertion of signal paths, receivers and processing equipment not currently in ASRs. As shown below, these can be added without affecting the radars' primary mission of aircraft detection and tracking.

Figure VII-1 is a schematic of the current signal paths in an ASR-9 from the antenna to the A/D converters. When the radar is transmitting linearly polarized (LP) signals, both the aircraft detection processor and the six-level weather reflectivity channel receive signals from the same-sense polarization ports on the antenna feeds. Both high and low beam signals are brought through the rotary joint in waveguide and a single set of A/D converters are switched between the beams in a range-azimuth gated (RAG) mode. When circularly polarized (CP) signals are transmitted, the target channel continues to receive same-sense polarized data while weather processing is accomplished using signals from the orthogonal antenna ports. Only one RF path through the rotary joint is available for the opposite-sense signals so that RAG switching between the high and low beams must be accomplished on the antenna.

Figure VII-2 shows modifications to these paths that would allow for acquisition of low beam signals at short range as required for wind shear detection. For LP operations, the single-pole, double-throw switch between the high and low beams would be replaced by a double-pole, double-throw switch. This would shunt low-beam signals to the combined reflectivity and wind shear processor for the range interval over which the target channel employs high beam signals. A separate STC module, receiver and A/D converter pair would be installed for this path. High beam data would be simultaneously available to the weather processor from the target channel A/D converters. While the associated STC setting might not be optimum for measurement of very low reflectivity weather signatures, it is unlikely that this would pose a problem for detection of "wet" microbursts -- the most prevalent form of wind shear. If the target channel's RAG program required a switch to low beam data within the range of operational concern for wind shear measurements, the indicated paths would reverse; the dedicated weather receiver would accept high beam data whereas low beam signals would enter the wind shear processor via the target channel A/D converters.

When the radar transmits CP signals, the weather channel receiver would be switched to the single RF path from the orthogonal-sense antenna ports. High or low beam signals could be acquired over any range interval desired, using an STC setting appropriate to the measurement of low reflectivity weather events. In this mode, it would not be possible to simultaneously access high and low beam orthogonally polarized signals, thus precluding the use of coherent, dual-beam velocity estimation techniques (Section IV-C-5). However, amplitude comparisons -- such as the differential low-high beam power spectrum technique considered in this report -- could be accomplished by switching between the high and low beams on alternate antenna scans. This would require a large memory in the wind shear processor to store signals for one scan.

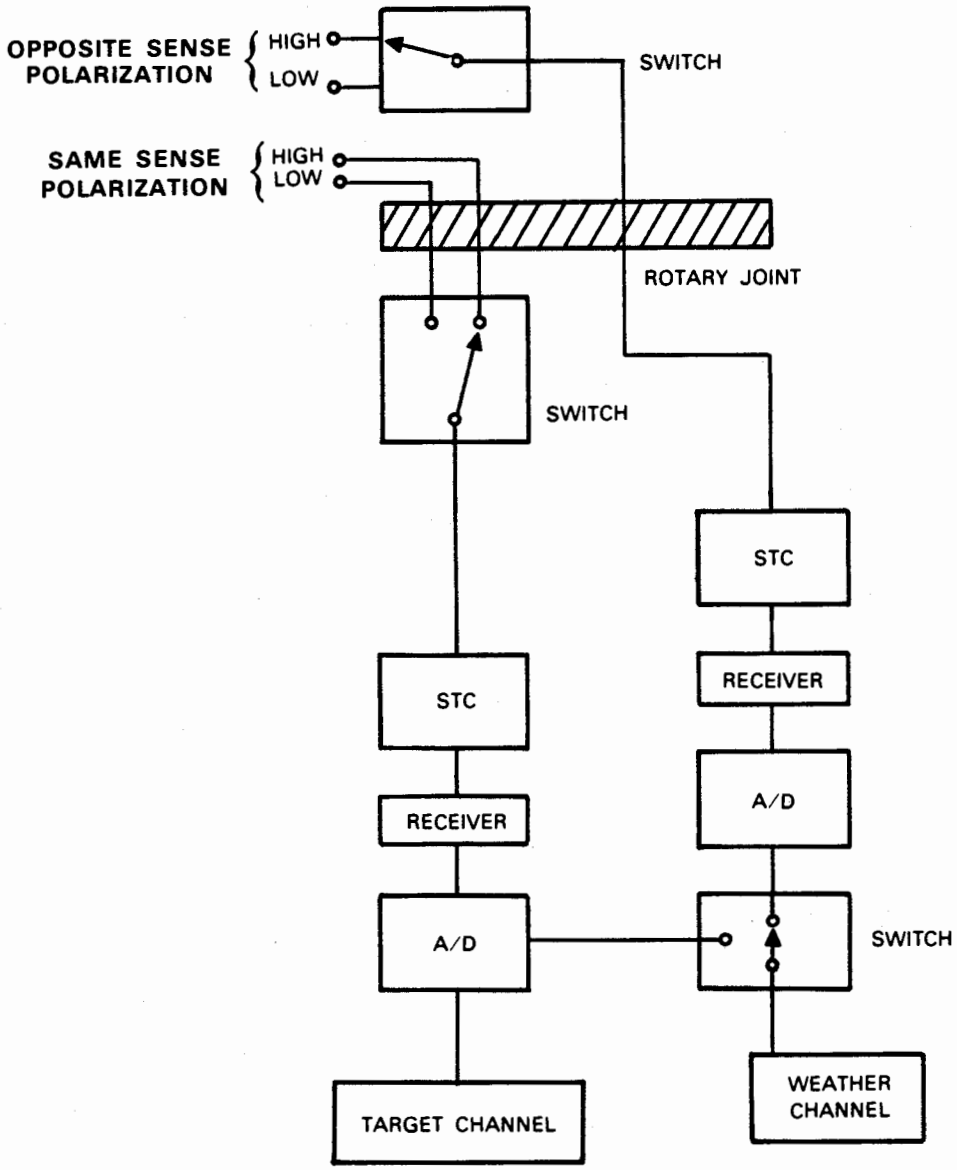


Figure VII-1 Simplified diagram of signal paths from ASR-9 antenna to airplane target processor and six level weather reflectivity processor.

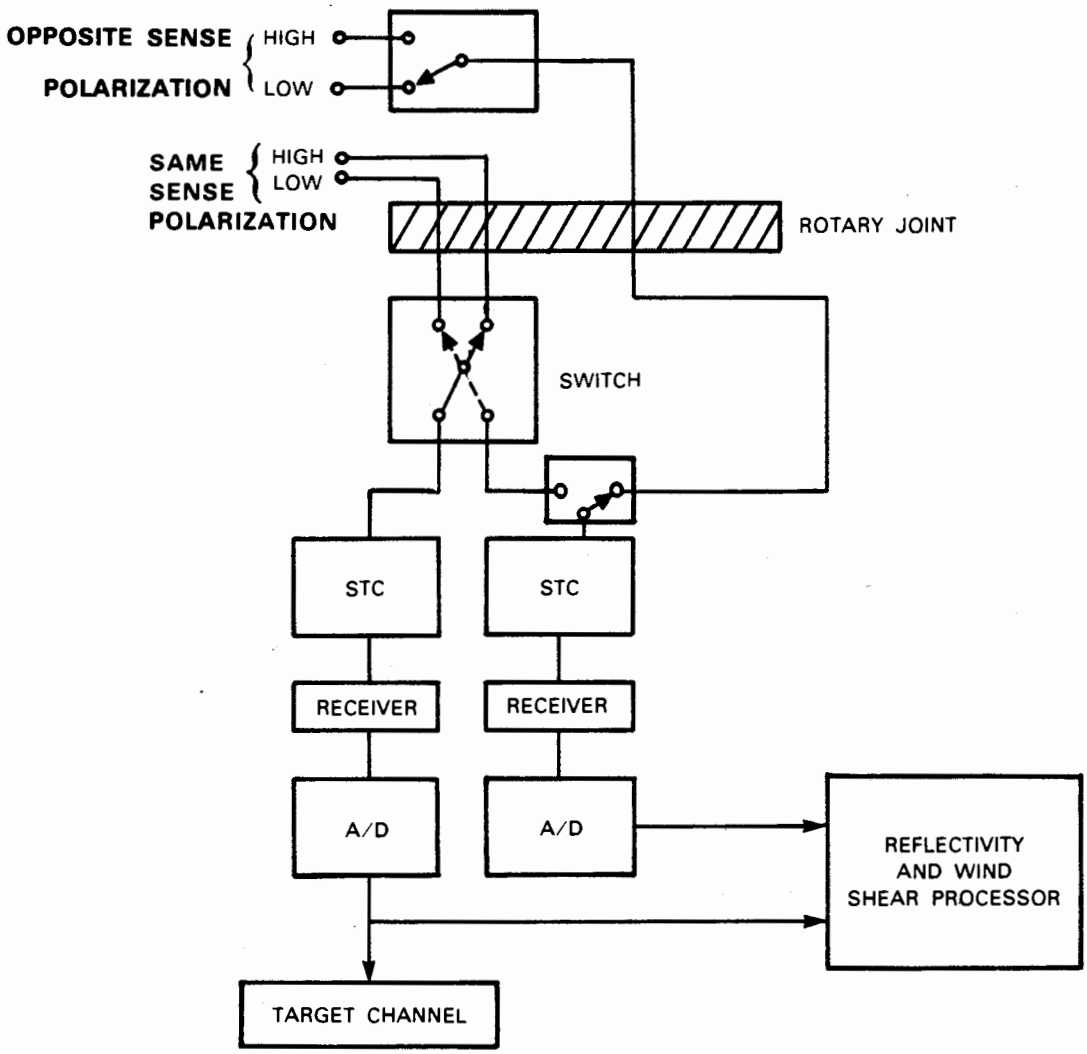


Figure VII-2 Diagram of modified ASR-9 signal path configuration to allow for low altitude wind shear processing.

The radar hardware needed to implement the necessary changes consists therefore of switches, a receiver chain and A/D converters; the latter two items could be taken from the current ASR-9 reflectivity processor (assuming that its function was subsumed by the enhanced weather channel). Local oscillator signals must be extracted from the exciter chain and suitable microwave components provided.

2. Processing Equipment

Cost-benefit analysis conducted for the TDWR procurement [22] indicated that -- if the radars result in the achievement of a five percent delay reduction -- the first forty airports equipped with TDWR would realize a benefit greater than the cost of the radars. An appealing feature of an ASR-based wind shear detection function is that the cost of the enhancement could be significantly less than that involved in acquisition of an entire radar system. This would allow for a cost-benefit based justification of a wind shear protection system for many secondary airports that will not receive a TDWR.

To minimize the cost of the add on system and to speed the development and procurement cycle, we recommend that the signal processing and hazard detection functions of an ASR wind shear channel be implemented using commercially available computers and array processors. This approach has a precedent in that the TDWR contract will allow for the use of commercially available processing equipment. As part of our field measurement program in 1988, Lincoln Laboratory is deploying a real-time signal processing system at the testbed ASR that will implement some of the processing/hazard detection sequences described in this report. The system uses an engineering workstation for control and microburst detection algorithm processing; high-speed signal processing operations are accomplished in array processor boards. The processors are modular and can be expanded to achieve computational speeds on the order of 100 million floating-point operations per second.

3. Output Product from ASR Wind Shear Processor

Investigators from Lincoln Laboratory and NCAR have developed formats for dissemination of microburst reports and reflectivity products from the TDWR. These are undergoing operational testing during the summer of 1988 in the tower and terminal radar control facility (TRACON) at Denver's Stapleton Airport. The current output products for ATC personnel are:

(1) an alphanumeric readout of wind shear location, type and intensity which will be available at individual TRACON stations. Figure VII-3, from McCarthy and Clyne [23], illustrates the information conveyed in this report;

(2) a graphical display of hazard locations, size and intensities for the TRACON and tower supervisors.

These formats could be used for reports from a stand-alone ASR wind shear detection system. A suitable update period needs to be established for ASR reports since controllers do not require wind shear reports updating at the 5 second antenna scan rate.

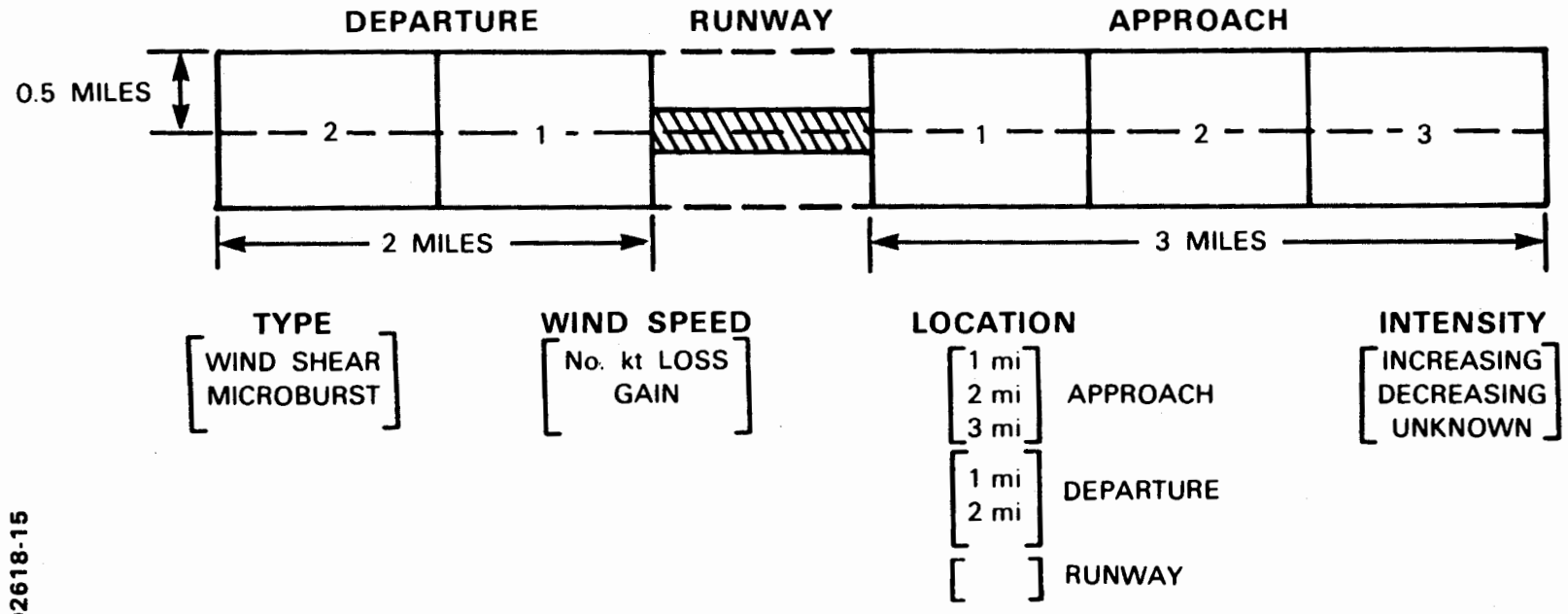


Figure VII-3 Illustration of TDWR wind shear alert format (from McCarthy and Clyne, [23]).

C. Future Investigations

Our preliminary evaluation indicates that a suitably modified airport surveillance radar would provide an operationally useful stand-alone capability for automatic detection of "wet" microbursts. A number of follow-on tasks are in progress to refine our understanding of this capability, to explore possibilities for "dry" microburst and gust front detection and to investigate possible utilization of ASR wind measurements in conjunction with other systems such as LLWAS or TDWR. We conclude this report with a brief itemization of areas where additional investigation is required.

1. Signal Processing Strategy

One long term goal is to develop a quantitative statement of performance versus complexity tradeoffs for the velocity estimation module in an ASR wind shear detection system. Issues such as the need for multiple versus a single clutter filter, or the requirement for combination of signals from high and low beams will directly affect the computational load and cost of the system.

The computational requirements of the low-high beam spectral differencing technique described in Section IV-C-4 significantly exceeds that required by the other signal processing methods treated. While our analysis indicated an improvement in microburst detection performance using this technique, comparative analysis should continue using additional data and iterations on the processing strategies. As an example. the placement and width of the filter stop band used to null overhanging precipitation echoes in the LBHP field could be varied based on information on mean mid-level wind velocity or previous estimates of outflow speeds.

As stated in Section IV-C-5, an ASR-based technique has been developed that uses the phase difference between high and low beam signals to provide three-dimensional information on the reflectivity and radial velocity of weather (or airplane) scatterers. On current ASRs, there are implementational problems in obtaining the required weather signals during CP operations. Research on this technique should continue, however, owing to its applications for aircraft intruder detection as well as enchanced hazardous weather surveillance. This effort will establish performance objectives and specify the needed modification to future generation ASRs to accommodate the hardware requirements.

2. Microburst Detection Algorithm

This work falls into two categories:

(1) refinement and continued testing of the microburst detection algorithm described herein;

(2) development and evaluation of alternative algorithms with substantially different logic.

An identified problem of the TDWR surface outflow algorithm has been intermittent detection of velocity shear signatures that are apparent to a trained human observer. This may arise form the inherent noisiness of weather radar data fields, interference from physical sources such as ground clutter, or unusual clustering in range and/or azimuth of radial shear segments. Enhancements to the detection sequence could include, for example, adaptive shear segment thresholding so that once strong radial shear was identified along an azimuth, the

surrounding shear region could be mapped out using looser criteria. Parametric studies of this algorithm's performance with varying threshold settings, using both ASR and TDWR-prototype velocity data, should continue.

The evaluated algorithm does not explicitly search for non-radial shear, nor does it make use of temporal continuity in the initial region finding operation. (Time continuity is used for post-filtering of shear regions.) Alternative microburst detection algorithms are under investigation that use multi-dimensional image processing to:

(i) relax the radial alignment requirement in the initial detection process;

(ii) "grow" shear regions over multiple scans to make explicit use of the high update rate of an ASR.

Owing to the planned off-airport siting of TDWR, the current divergent outflow algorithm is not designed for the case where a microburst outflow occurs on top of the radar; in this situation shear segments would be split across diametric radials and would not necessarily be grouped azimuthally into the same shear region. This problem needs to be addressed, either through modification of the existing TDWR algorithm or in the development of alternative techniques.

3. Gust Front Measurement and Detection

As stated in the introduction, detection and tracking of gust fronts could provide significant benefits to airport operations by warning air traffic controllers of an impending wind shift. Low reflectivity gust fronts as depicted by the Huntsville ASR measurements were often fragmented owing to receiver noise and/or ground clutter residue. In addition, winds in clear air ahead of and behind the front were not measured owing to insufficient sensitivity. Figure VI-4 shows an example of a gust front signature measured by the ASR testbed. We expect that temporal and/or additional spatial filtering of ASR signals will provide "cleaner" representations of gust fronts than depicted here.

Initial experimentation with the algorithm developed for TDWR gust front detection have not been favorable because -- as presently structured -- this algorithm searches exclusively for a convergent radial velocity line to identify the front. This feature is simply not present in the ASR-generated velocity fields in many cases.

Refinements to the current algorithm will involve:

(1) logic to search for "thin-line" features that characterize the reflectivity and radial velocity signatures of a gust front in the ASR data;

(2) removal of the orientation sensitivity of the current algorithm. Azimuthal shear detection must be included to detect gust front segments that are oriented along a radial with respect to the radar;

(3) elimination of algorithm-induced segmentation of gust fronts that may occur even when the front is clearly defined in the radar data.

Each of these investigations has direct applications to the TDWR gust front detection effort and will be conducted in cooperation with investigators in that program.

4. "Dry" Microburst Measurement and Detection

Analysis [1,3] of the limits of ASR sensitivity and ground clutter suppression indicated that noise and ground clutter residue may interfere with an ASR's measurements of winds when the reflectivity factor is below about 20 dBz. Gust front measurements from the Huntsville field experiment have borne out these analyses. To better define the capabilities and limitations for an ASR to measure dry microburst outflows, we are conducting a simulation-based analysis, using volume scan data from Lincoln Laboratory's TDWR testbed in Denver.

The procedure described in reference [1] is used to simulate time-series signals as would be seen by a fan-beamed ASR. Additive noise and ground clutter are included. The approach allows for full simulation of the signal processing sequence and for evaluation of the effects of varying radar and environmental parameters. Examples of such parameters are the mean clutter cross section, the STC function, and the tilt angle of the ASR antenna beam.

## 5. Utilization of ASR Data in Conjunction with LLWAS

As would be the case where a TDWR and LLWAS are sited at the same airport, an ASR would provide complementary information to the surface anemometer network. Joint usage of wind measurements from the ASR and LLWAS needs to be defined for airports equipped with both sensors.

In the critical runway corridors covered by LLWAS, the ASR could confirm the existence and type of wind shear as well as detecting divergence which has not yet reached the surface. The ASR could reduce the probability of LLWAS false alarms due to thermals, for example, by determining whether there is precipitation aloft Methods for usefully combining the LLWAS discrete wind vector measurements with the radial velocity fields measured by the radar need to be investigated in both the ASR and TDWR context.

The ASR could provide wind shear warnings for those areas within 5 km of the airport center that are not covered by LLWAS as well as for the area beyond 5 km. Algorithms to track the movement of wind shear detected outside the LLWAS corridors should be developed so as to provide warnings of the movement of wind shear onto the runways or approach/departure corridors. Likewise, definition of the capabilities of an ASR to detect and track gust fronts is needed to provide a quantitative measure of the airport operations planning benefit to be derived from the ASR wind measurements.

## 6. Utilization of ASR Data in Conjunction with TDWR

As pointed out in the introduction to this report, the point-wise accuracy of ASR radial velocity measurements is important in assessing the utility of a dual-Doppler system involving a TDWR and an ASR. While we did not explicitly assess this issue, our evaluation of the accuracy of differential velocity estimates across microbursts can be used for a rough estimate by assuming that the contributing errors from the $V_R$ estimates in the approaching and receding microburst cores are independent. Typical RMS errors for the differential velocities estimated from the DBV field were 4 m/s; the implied point-wise accuracy is therefore 2.8 m/s which is probably sufficient for a useful dual-Doppler measurement. The capability to achieve such accuracy from the ASR needs to be verified directly, however.

It is plausible that information from the TDWR on three-dimensional storm

structure (i.e. the location and vertical extent of microburst outflows, vertical reflectivity structure) could be fed to an ASR wind shear processor to improve the velocity estimates or at least to flag conditions under which the ASR-generated fields may be of low accuracy. Conversely, rapid update data from an ASR could be supplied to the TDWR to refine scanning procedures or to provide temporal tracking on rapidly changing events. Careful consideration as to how data from the two radars should be integrated comprises a long term research and development effort.

## ACKNOWLEDGEMENTS

We wish to acknowledge the contributions of John Anderson (University of Wisconsin, Madison). John first proposed the use of airport surveillance radars for low altitude wind shear detection in 1984 and has been a key player in subsequent investigations of their capabilities in this role. Jim Pieronek, Bill Moser and Bill Drury (Lincoln Laboratory) executed the development and integration effort necessary to transform a stock ASR-8 into the flexible ASR-9 emulation facility described herein. Weather radar support was provided through the cooperation of Earle Williams, Spiros Geotis and Oliver Newell (Massachusetts Institute of Technology) and Dean Puzzo (Lincoln Laboratory). Wes Johnston, Jay Laseman, Gene Telles (RCA) and Mark Burzinski (University of Wisconsin, Madison) staffed and operated the Huntsville field site to record and log the data which formed the basis for this report. Mark Meister (Lincoln Laboratory) assisted in the development of signal processing software for the ASR data. We wish to thank Joe Cullen (Lincoln Laboratory) whose efforts in data processing and meteorological analyses were indispensable in producing this report. Finally, we acknowledge the ASR-9 Program Supervisor, Carmine Primeggia (FAA ASA-140) and Marty Pozesky (FAA ADL-2) for their early recognition of the capabilities of ASRs for wind shear detection and long term support.

This work is being performed under Interagency Agreement No. DTFA01-80-Y-10546 and is sponsored by the Federal Aviation Agency.

**REFERENCES:**


1. M.E. Weber and W.R. Moser, *A Preliminary Assessment of Thunderstorm Outflow Wind Measurement with Airport Surveillance Radars,* Project Report ATC-140, Lincoln Laboratory, MIT, FAA-PM-86-38, 1987.

2. J.R. Anderson, *The Measurement of Doppler Wind Fields with Fast Scanning Radars: Signal Processing Techniques,* Journal of Applied Meteorology, 4, pp 627-633, 1987.

3. M.E. Weber, *Ground Clutter Processing for Wind Measurements with Airport Surveillance Radars,* Project Report ATC-143, Lincoln Laboratory, MIT, FAA-PM-87-21, 1987.

4. T.T. Fujita, *The Downburst,* SMRP Research Paper 210, University of Chicago, 1985.

5. R.C. Goff, *Observation of Thunderstorm Induced Low Level Wind Variations,* Preprints, Amer. Inst. of Aeronautics and Astronautics, 9th Fluid and Plasma Dynamics Conf., San Diego, CA (AIAA Paper No. 76-388), 1976.

6. K.L. Elmore and F.W. Wilson, *LLWAS Performance Assessment During the 1987 TDWR Field Project,* EOS, Trans. Amer. Geophys. Union, 68, pp 1229, 1987.

7. M.D. Eilts, *Use of a Single Doppler Radar to Estimate the Runway Wind Shear Component in Microburst Outflows,* Amer. Inst. of Aeronautics and Astronautics 26th Aerospace Sciences Meeting Paper, (AIAA Paper No. 88-0694), 1988.

8. General Accounting Office, *Status of FAA's New Hazardous Weather Detection and Dissemination Systems,* Report To the Chairman, Committee on Science, Space, and Technology, U.S. House of Representatives, GAO/RCED-87-208, 1987.

9. M.E. Weber, *Assessment of ASR-9 Weather Channel Performance: Analysis and Simulation,* Project Report ATC-138, Lincoln Laboratory, MIT, FAA-PM-86-16, 1986.

10. M.M. Wolfson, J.T. DiStefano and D.L. Klingle, *An Automatic Weather Station Network for Low-Altitude Wind Shear Investigations,* Project Report ATC-128, Lincoln Laboratory, MIT, 1984.

11. D.A. Clark, *Observability of Microbursts with Doppler Weather Radar During 1986 in Huntsville, AL,* Project Report ATC-160, Lincoln Laboratory, MIT, in progress.

12. M. Isaminger, Lincoln Laboratory, MIT, personal communication.

13. R.E. Rinehart, J.T. DiStefano and M.M. Wolfson, *Preliminary Memphis FAA / Lincoln Laboratory Operational Weather Studies Results,* Project Report

ATC-141, Lincoln Laboratory, MIT, FAA-PM-86-40, 1987.

14. D.S. Zrnic, *Spectral Moment Estimates from Correlated Pulse Pairs,* IEEE Transactions Aerospace and Electronics Systems, AES-13, pp 344-354, 1977.

15. M.W. Merritt, *Automatic Detection of Microburst Windshear for Terminal Doppler Weather Radar,* Digital Image Processing and Visual Communications Technologies in Meteorology, Cambridge, MA, 26-28 October, 1987.

16. S. Campbell, *Microburst Recognition: An Expert System Approach,* Preprints, 23rd Radar Meteor. Conf., Snowmass, Co., American Meteor. Soc., Boston, 1986.

17. H. Uyeda and D.S. Zrnic', *Automatic Detection of Gust Fronts,* Final Report DOT-FAA-PM-85-11, April 1985.

18. J.R. Anderson, Department of Meteorology, University of Wisconsin, Madison, personal communication.

19. D.Atlas, *Radar Detection of Hazardous Small Scale Weather Disturbances,* United States Patent Number 4,649,388, March 10, 1987.

20. NEXRAD Program Office, *Divergence Detection Algorithm Description,* NX-DR-03-042/10, Next Generation Weather Radar Algorithm Report, 1985.

21. M.W. Merritt and S.D. Campbell, *Microburst Detection Algorithm,* Project Report ATC-145, Lincoln Laboratory, MIT, FAA-PM-87-23, in progress.

22. Martin Marietta Corporation, *Terminal Doppler Weather Radar Report,* ATC-85-1004, 1985.

23. J. McCarthy and P. Clyne, *A Strategy for Avoidance of Hazardous Convective Weather in the Aiport Terminal Area,* 40th International Air Safety Seminar Flight Safety Foundation, Tokyo, Japan, October 26-29, 1987.

## APPENDIX A: CALCULATION OF THE EFFECT OF MICROBURST ASYMMETRY ON SINGLE OR DUAL RADAR WIND SHEAR ESTIMATES

As a simple model for an asymmetric microburst, we assume that the wind direction is radial from the center of the outflow and that wind speed variation with azimuth follows the equation for an ellipse:

$$V(\phi) = \frac{V_{max} V_{min}}{\sqrt{V_{max}^2 \sin^2(\phi) + V_{min}^2 \cos^2(\phi)}} \quad \text{(A-1)}$$

Here $\phi$ is the azimuthal angle relative to the direction of maximum wind speed and $V_{max}$, $V_{min}$ are the maximum and minimum wind speeds. As a function of range from the microburst center, the maximum winds are assumed to occur on a circle of radius equal to that of the downdraft. Here, we have set this radius at 250 m.

As illustrated in Figure A-1, the radial wind component $V_R$ measured by a radar viewing this wind distribution is a function of:

(i) the angle $\phi$ between the direction of maximum wind speed and the viewing point on the "downdraft" perimeter;

(ii) the angle $\theta$ between the wind direction at this viewing point and the radial from the radar. This angle is a function of $\phi$ and the location of the radar with respect to the microburst center.

The maximum velocity differential that could be measured by a single radar is determined by computing $V_R$ around the perimeter of the downdraft and subtracting the extrema. Note that the maximum approaching and receding radial velocities will not necessarily occur along a single radial if the outflow is asymmetric. Comparison of the resulting $\Delta V_R$ measurement to $2V_{max}$ determines the bias in single Doppler shear estimates relative to the maximum shear. This calculation was repeated for microburst "centers" at grid points separated by 1 km.

Figure A-2 is an illustration of the calculation for the runways at Denver's Stapleton Airport. Each plot treats one runway: the rectangle surrounding the runway is a 2 by 6 nmi corridor where wind shear information is most critical to pilots. We have assumed a worst-case asymmetric microburst scenario with three times the wind shear along the runway directions as at right angles. The shaded region is where the single-Doppler TDWR velocity differential measurement would be within 20 percent of the true runway shear. In both cases, the 20 percent accuracy criterion is not met over the entire corridor of interest. In the case of the north-south runways, the runways themselves and the approach corridor from the south would be outside of the region of accurate coverage.

To calculate the RMS dual-Doppler estimate accuracy, each radar's radial velocity measurements are taken to have a relative accuracy of 10 percent. The error in the dual-Doppler wind speed estimate at the points of strongest outflow along the microburst perimeter are:

$$\sigma_{V_{D-D}} = \sqrt{\frac{\sigma_{V_1}^2 + \sigma_{V_2}^2}{\sin^2(\theta_1 - \theta_2)}} \quad \text{(A-2)}$$

Here $\theta_1$ and $\theta_2$ are the angles between the radar radials and the direction of maximum wind speed. Errors in the single-Doppler radial velocity measurements (at

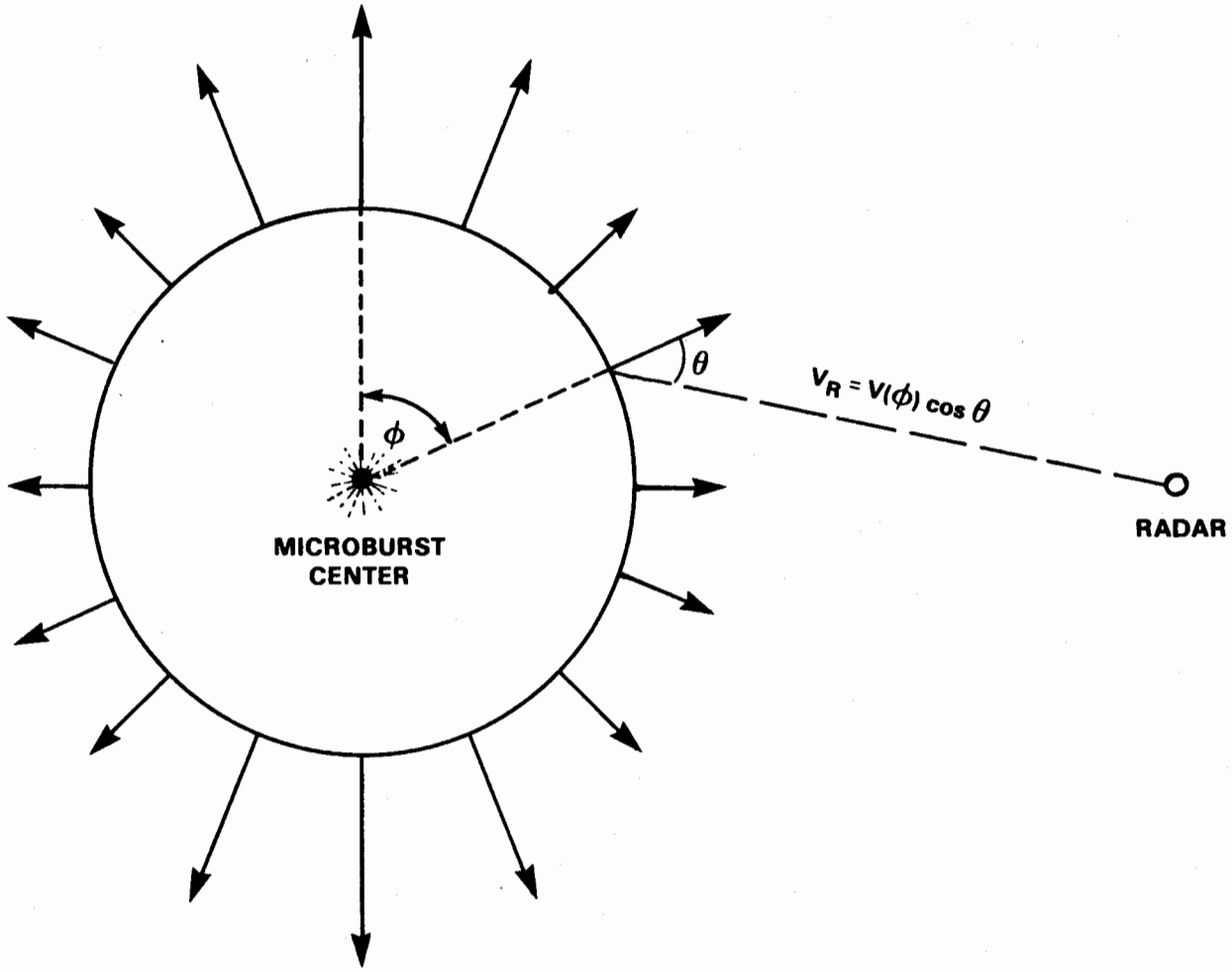


Figure A-1 Geometry of asymmetric microburst model.

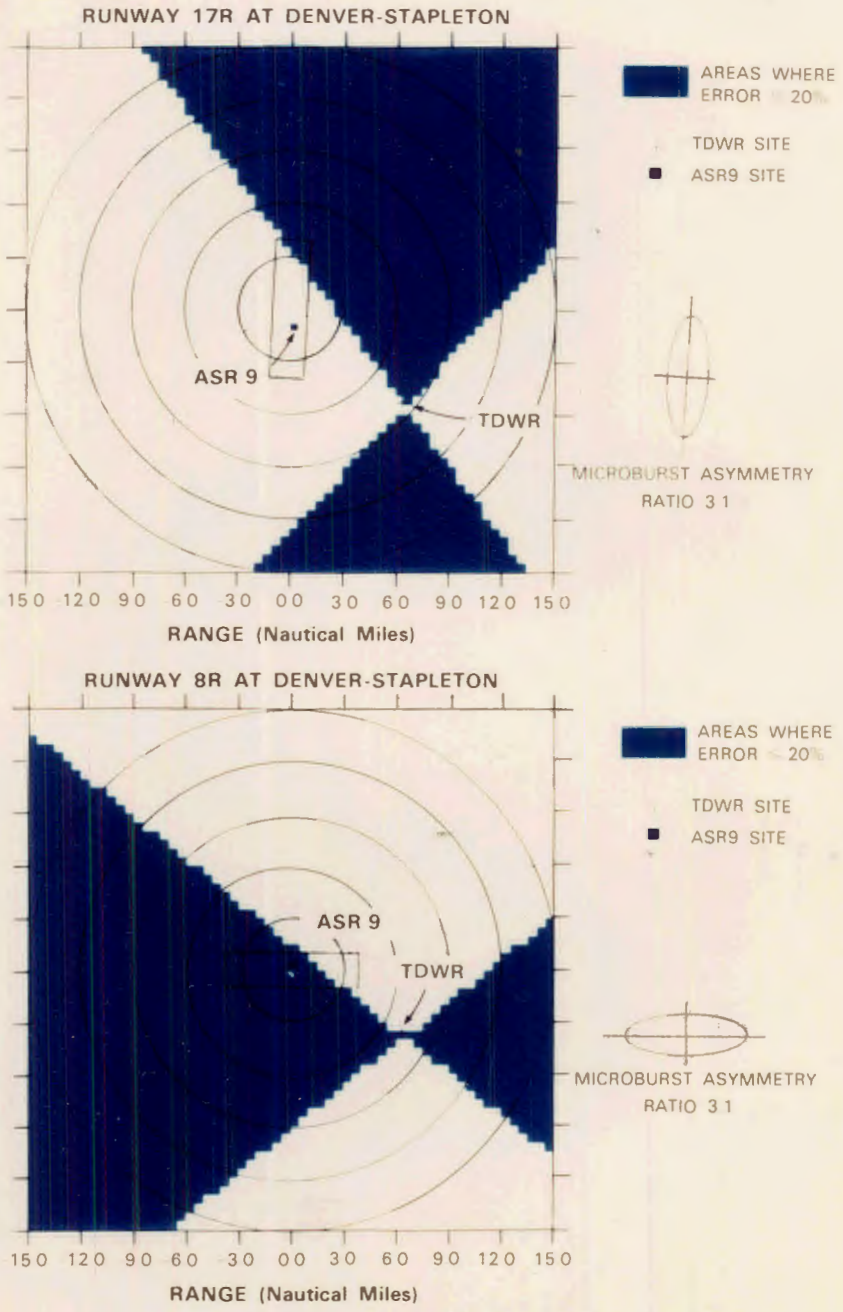


104936-1

*Figure A-2. Illustration of problem associated with estimation of headwind-tailwind shear for an asymmetric microburst. Location of TDWR site relative to Denver-Stapleton Airport is indicated. Shaded area is region where single-Doppler shear estimate would be within 20 percent of true runway oriented shear under severe microburst asymmetry conditions. Calculation assumes 3 times the velocity shear along runway direction as in perpendicular direction.*

the points of maximum outflow speed) are:

$$\sigma_{V_{1,2}} = 0.10\ V_{\max}\cos(\theta_{1,2}) \tag{A-3}$$

The relative error in the dual-Doppler microburst differential velocity estimate is therefore:

$$\frac{\sigma_{\Delta V}}{\Delta V} = \frac{\sqrt{2}\sigma_{V_{D-D}}}{2V_{\max}} \tag{A-4}$$

Figure A-3 repeats the coverage calculation for Stapleton airport assuming data from both the ASR and TDWR were used. We have assumed that the wind shear report is generated from dual-Doppler wind calculations over the region where the geometries of the two radars allows for RMS relative errors of 20 percent or less. Otherwise the reported wind shear would be the maximum of the single-Doppler TDWR or ASR measurement.

Utilization of the ASR data would result in a substantial increase in the area where accurate headwind-tailwind shear estimates would be feasible. With the exception of a small fraction of the corridor surrounding the north-south runways, the critical areas for wind shear detection would be well covered even in this worst case asymmetry scenario.

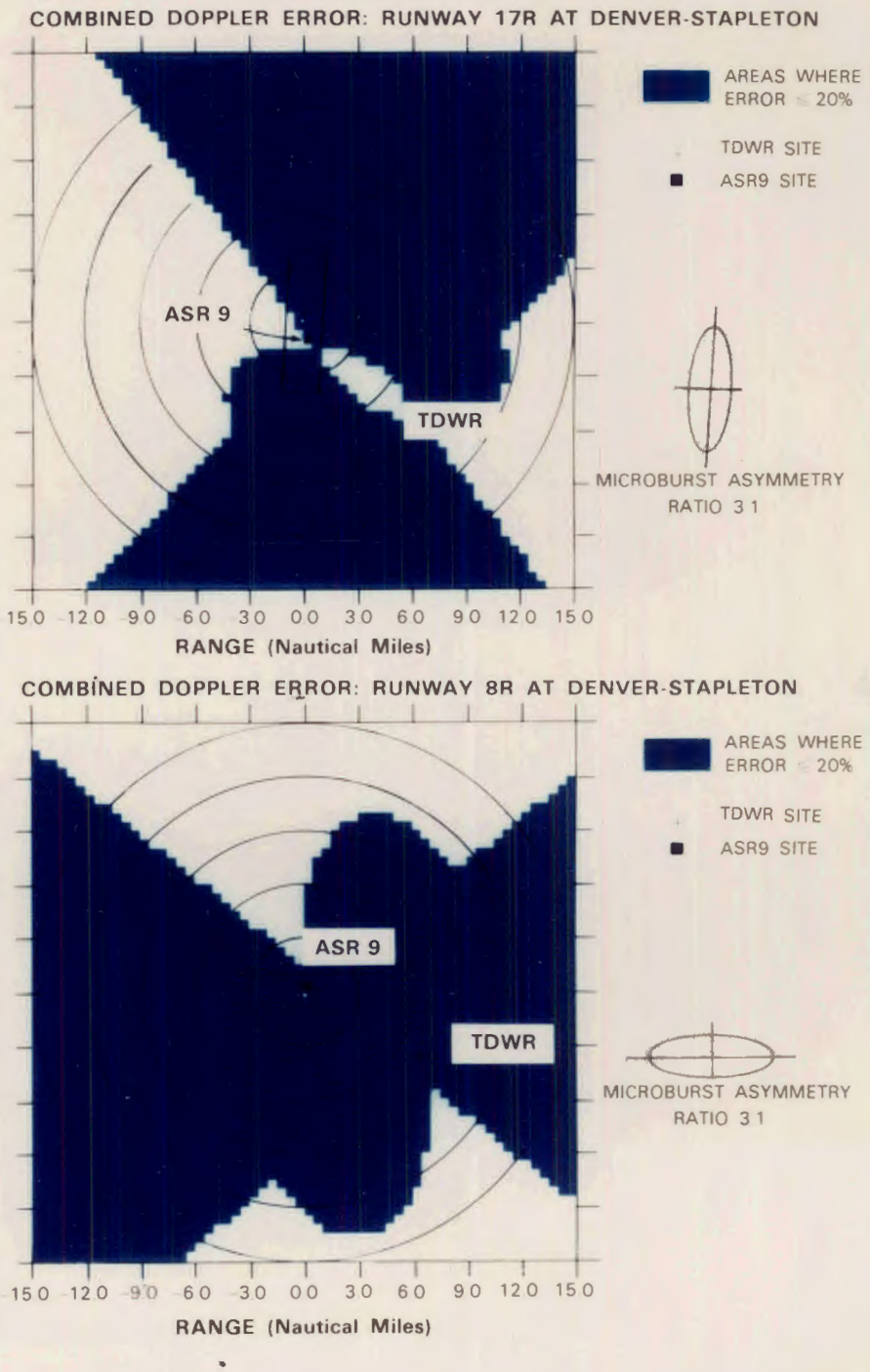


104936-3

*Figure A-3. Areas at Denver-Stapleton Airport where combined TDWR and ASR measurements of headwind-tailwind shear along runway directions would be within 20 percent of true shear under severe microburst asymmetry conditions.*

## APPENDIX B: MICROBURST DETECTION ALGORITHM PARAMETERS

This appendix defines parameters used in the implementation of the hierarchical feature extraction process of the divergent outflow detection algorithm described in Chapter V. These parameters would be site adjustable to permit adaptation to local wind shear characteristics. Parameters used in the three phases of feature extraction -- shear segment detection, shear region identification, and microburst detection -- are given below.

### A. Shear Segment Feature Detection Parameters

The first part of Table B-1 lists current values of the parameters used in the shear segment feature detection process.

**Table B-1: ASR Algorithm Site Adaptation Parameters**

| | |
|---|---|
| *Shear Segment Identification* | |
| Number_Window | 4 |
| Number_Increase | 2 |
| Threshold_Min_Pos | 15 m/s |
| Threshold_Out | 1/8th |
| Threshold_Min_DV | 3 m/s |
| Threshold_Min_Length | .8 km |
| *Shear Region Identification* | |
| Threshold_Seg_Overlap | .5 km |
| Threshold_Angular | 2 |
| Threshold_Min_Segments | 2 |
| Threshold_Total_Area | 1.0 sq km (LBV3 - .5 sq km) |
| Threshold_Max_Diff | 5 m/s |
| *Microburst Identification* | |
| Threshold_Time_Limit | 1 min |
| Threshold_Scan_Limit | 2 |
| Threshold_Region_Distance | 3 km |
| Threshold_MB_DV | 8 m/s |

The algorithm searches outward in range along radials of velocity measurements for generally increasing runs of velocities. These runs are found by sliding a pattern search window of size *Number_Window* along a radial. A shear segment is begun when a fixed number of contiguous velocities (denoted by *Number_Increase*) within the window are increasing. A segment continues to grow as the window slides until either the windowed signature is no longer increasing or the minimum velocity jump in the window is greater than *Threshold_Min_Pos*. During this segment growing process, an attempt is made to minimize the rejection of true features by allowing for spurious data values or outliers (typical of wind measurements) within these runs.

To reduce false detections, the completed segments are then pruned using additional tests, implemented using the parameters *Threshold_Out*, *Threshold_Min_Length* and *Threshold_Min_DV*. These tests impose requirements on segment smoothness, length, and the velocity difference across the segment.

Explicit definitions of the segment identification parameters are:

(1) *Number_Window:* The number of contiguous range bins along a radial which define the divergent shear segment search window.

(2) *Number_Increase:* The number of contiguous range bins for which the velocity must be increasing in order to signal the start of a shear segment feature.

(3) *Threshold_Min_Pos:* The maximum value allowed for the minimum positive velocity increase within the pattern search window to continue a shear segment feature. If the minimum change in velocity is too great the segment will be discontinued.

(4) *Threshold_Out:* The maximum percentage of bad data values and velocity values out of range allowed in the entire segment. Out of range values include velocities less than that at the segment start or greater than that at the segment end.

(5) *Threshold_Min_DV:* The minimum change in velocity required to retain a shear segment.

(6) *Threshold_Min_Length:* The required length of a shear segment.

B. Shear Region Feature Detection Parameters

The algorithm next joins segments within *Threshold_Angular* radials which overlap in range by a distance of at least *Threshold_Seg_Overlap* to form two-dimensional shear regions.

These regions are then post filtered using size (*Threshold_Min_Segments*, *Threshold_Total_Area*) and shear strength (*Threshold_Max_Diff*) criteria.

Parameters used in the shear region detection process are:

(1) *Threshold_Seg_Overlap:* Minimum overlap in range required to associate two shear segments.

(2) *Threshold_Angular:* The maximum number of azimuths over which to associate two shear segments.

(3) *Threshold_Min_Segments:* The minimum number of shear segments required for a shear region to be valid.

(4) *Threshold_Total_Area:* The minimum total area required for a shear region to be valid.

(5) *Threshold_Max_Diff:* The minimum value required for the maximum point-to-point radial velocity difference across the entire shear region.

C. Microburst Feature Detection Parameters

Each region found on the latest scan is associated with all found on recent (*Threshold_Scan_Limit* or *Threshold_Time_Limit*) scans if the Cartesian distance between region centers is less than *Threshold_Region_Distance.* If the closest previous region is not already tagged as part of a microburst, and the current region exhibits a velocity difference of at least *Threshold_MB_DV*, a new microburst is

declared. If the closest or best overlapping previous region is already part of a microburst, the current region becomes part of this event.

Parameters used in this microburst feature detection process are given below. Current values of these parameters are given in Table B-1.

(1) *Threshold_Time_Limit:* The maximum time difference allowed for associating shear regions into microburst objects.

(2) *Threshold_Scan_Limit:* The maximum number of previous surface scans to search for previous overlapping shear regions.

(3) *Threshold_Region_Distance:* The maximum distance allowed between shear region centers for time correlation.

(4) *Threshold_MB_DV:* The velocity difference across a region which has been associated with a previous region required to declare a new microburst.